Universität Zürich[UZH]

Geographisches Institut

Retrieval of biomass and fractional vegetation cover of mixed cover crops using hyperspectral UAV data

GEO 511 Master's Thesis

Author: Valerie Schneider, 19-103-662

Supervised by: Dr. Helge Aasen (helge.aasen@agroscope.admin.ch), Dr. Francesco Argento (francesco.argento@agroscope.admin.ch), Sélène Ledain (selene.ledain@agroscope.admin.ch)

Faculty representative: Prof. Dr. Alexander Damm

30.01.2026

Universität Zürich[UZH]

Schweizerische Eidgenossenschaft
Confédération suisse
Confederazione Svizzera
Confederaziun svizra

Eidgenössisches Departement für
Wirtschaft, Bildung und Forschung WBF
Agroscope
Schweizer Nationalgestüt SNG

GEO 511 Master's Thesis

Retrieval of biomass and fractional vegetation cover of mixed cover crops using hyperspectral UAV data

Author
Valerie Schneider
19-103-662

Supervised by
Dr. Helge Aasen (helge.aasen@agroscope.admin.ch)
Dr. Francesco Argento (francesco.argento@agroscope.admin.ch)
Sélène Ledain (selene.ledain@agroscope.admin.ch)

Faculty representative
Prof. Dr. Alexander Damm

January 30, 2026
Department of Geography, University of Zurich

Abstract

Cover crops are a key component of conservation agriculture, providing important ecosystem services, particularly by improving soil quality and reducing soil erosion. Above-ground biomass and fractional vegetation cover are widely used indicators to quantify their agronomic and ecological effects. Large-scale monitoring of these indicators is essential for management decisions and for evaluation of the effectiveness of cover crop practices. Traditional remote sensing methods perform well for single-species crops, but mixed-species canopies present more complex spectral signals and are rarely studied.

Therefore, the objectives of this study were to evaluate the potential of different remote sensing approaches for biomass and fractional cover retrieval in heterogenous mixed cover crop systems. A field experiment was conducted in Switzerland, and high-resolution hyperspectral drone data were acquired alongside biomass and fractional cover reference measurements. These data were processed into a consistent training and evaluation dataset.

Biomass and fractional cover were estimated using vegetation index–based (VI), radiative transfer model–based (RTM), spectral mixture analysis–based (SMA), and neural network–based approaches. Biomass retrieval generally showed moderate accuracy and strong sensitivity to mixture complexity. RTM-based approaches performed well for structurally simple mixtures but deteriorated with increasing canopy heterogeneity, while red-edge-based VIs provided the most consistent biomass estimates for individual mixtures. In across-mixture settings, the GnyLi index achieved the best performance. For green fractional vegetation cover, VI- and RTM-based approaches achieved robust results in both mixture-specific and across-mixture evaluations, with MTVI2 performing best. These findings indicate that full hyperspectral information is not necessarily required for accurate fractional cover estimation in green mixed canopies. In contrast, the widely applied SMA showed limited applicability in heterogeneous mixtures, indicating the need for further research to identify underlying causes and potential improvements.

Overall, this thesis contributes to a better understanding of the potential and limitations of different biomass and fractional cover retrieval approaches for mixed cover crops. It further highlights the use of hyperspectral UAV data as a test framework to evaluate these methods, supporting the development of future operational large-scale monitoring systems for cover crop quality and associated ecosystem services.

Acknowledgements

I would like to express my sincere gratitude to everyone who supported me in various ways throughout the entire process of creating this work.

I would like to thank Prof. Dr. Alexander Damm, my faculty representative, for providing valuable guidance and insightful feedback throughout the work. A big thank you goes to my supervisors, Dr. Helge Aasen, Dr. Francesco Argento and Sélène Ledain. Dr. Helge Aasen made this entire work at Agroscope possible. His constant support, constructive guidance, clear advice, and innovative ideas were invaluable throughout the project. Dr. Francesco Argento was a reliable cotact for all my questions regarding fieldwork and drones, and Sélène Ledain supported me with all my methodological and programming issues.

The intensive filedwork would not have been possible without a lot of help from many people at Agroscope. I would like to express my special gratitude to Alessandro Pierro and Filip Mrcarica who assisted with the biomass sampling, enduring strong heat and itchy plants. I am also grateful to the team operating the hyperspectral drone and all colleagues who assisted me with technical work, including Hans-Ulrich Zbinden, Jonas Winizki, Pascal Ackermann and others. Many thanks also to the EOA Team for the supportive and very friendly atmosphere at work. Also, I would like to thank my predecessor Timon Boos, who introduced me to his work, which formed the basis for parts of this thesis.

I would also like to thank ReSe Applications and Dr. Daniel Schläpfer together with HySpex Neo for their support with hyperspectral data processing, offering guidance, advice and troubleshooting.

Finaly, I would like to thank my family and friends for their support, encouragement, and patience throughout this project and especially Jérôme Messmer and Flurina Schneider for proof reading.

Contents

List of Figures

List of Tables

Acronyms

DEM Digital Elevation Model

DN Digital Number

GBVI Green Brown Vegetation Index

GCP Ground Control Point

GNSS Global Navigation Satellite System

GnyLi Vegetation Index named by the developers Gnyp and Li

IMU Inertial Measurement Unit

LAI Leaf Area Index

MTVI2 Modified Triangular Vegetation Index 2

NDVI Normalized Difference Vegetation Index

NN Neural Network

RGB Red Green Blue

ROI Region of Interest

RTM Radiative Transfer Model

SMA Spectral Mixture Analysis

SWIR Short Wave Infrared proportion of the electromagnetic spectrum ($\sim$ 900 - 2500 nm)

TVI Triangular Vegetation Index

UAV Unmanned Aerial Vehicle

VIs Vegetation Indices

VNIR Visible and Near-Infrared proportion of the electromagnetic spectrum ($\sim$ 400 - 1100 nm)

1 Introduction

1.1 Importance of cover crops in agriculture

Soils are one of the most essential natural resources for global food production. However, they are increasingly threatened by intensive, conventional agricultural practices, which amplify erosion, degrade soil structure, and reduce biodiversity (Büchi et al., 2016; Vincent-Caboud et al., 2017; Adetunji et al., 2020). Soil erosion is a particularly problematic issue because it results in the loss of nutrient-rich topsoil (Bashagaluke et al., 2018). It also contributes to the contamination of groundwater and surface water because eroded sediments often carry fertilizers, pesticides, and other agrochemicals into the hydrological system (Papadopoulos et al., 2006, as cited by Muñoz et al., 2010; Prabhakara et al., 2015). Conservation agriculture practices have become increasingly important in recent years to reduce these negative environmental impacts and to maintain long-term soil productivity (Adetunji et al., 2020).

One important conservation agriculture practice is the use of cover crops, which are grown during fallow periods between the main crops. They are grown for ecosystem services rather than harvest and provide a range of functions, such as reducing soil erosion, improving soil structure, decreasing nitrogen leaching and increasing soil organic matter (Büchi et al., 2016; Daryanto et al., 2018). Cover crops are usually cultivated as mixtures of species, to benefit from their diverse functions (Holzhauser et al., 2022). In Switzerland, the planting of cover crops after a summer harvest is a requirement in the Ecological Performance Record (ÖLN) for farmers to receive direct payments (Schweizerischer Bundesrat, 2013).

The ability of cover crops to reduce soil erosion depends on the species used, their biomass production, and the extent of soil cover. Accurate data and knowledge about cover crop growth and characteristics are therefore crucial for farmers to make informed management decisions (Holzhauser et al., 2022). Biomass production and fractional vegetation cover are widely used as key indicators for assessing the quality of cover crops. In this context, quality refers to the cover crops' capacity to provide ecosystem services. These key indicators are directly linked to cover crop services. Higher biomass contributes to erosion control, nitrogen retention, soil fertility and weed suppression (Büchi et al., 2016; Finney et al., 2016; Poudel et al., 2025; Salehin et al., 2025). While higher fractional cover reduces soil exposure to wind and rain, thereby reducing erosion (Büchi et al., 2016; Adetunji et al., 2020). Monitoring these indicators on a large scale is not only important to inform farmers on the success of their management decisions but also essential to quantify the adoption of cover crops and assess the effectiveness of their diverse benefits for ecosystems and agriculture (Adetunji et al., 2020).

1.2 Remote sensing of cover crops

Traditional methods for monitoring cover crops like in-situ sampling are labour-intensive, spatially limited and time consuming (Salehin et al., 2025). In contrast, remote sensing technologies, in particular satellite-based observations, can be used to continuously monitor cover crops both over time and across large areas (Kumar and Mutanga, 2017; Poudel et al., 2025). Approaches used for cover crop monitoring build on established optical remote sensing techniques developed for vegetation assessment and have been applied across a range of platforms, including satellite, airborne and Unmanned Aerial Vehicle (UAV) systems.

1.2.1 Biomass estimation of cover crops

Above-ground biomass is a commonly used measure of cover crop growth and canopy development. In the following, the shorter term *biomass* is used to refer to above-ground biomass. Numerous studies have reported good biomass estimation accuracies for single cover crop species. For example Hively et al. (2009), Prabhakara et al. (2015) and Goffart et al. (2021) found good relationships between Vegetation Indices (VIs) and biomass of single winter cover crop species. These approaches are particularly effective during mid-growth stages but often suffer from saturation effects at higher biomass levels and show limited transferability across sites and conditions (Myneni and Williams, 1994; Wang et al., 2023; Salehin et al., 2025). For cover crop mixtures, reported model performance is generally lower than for single species (Goffart et al., 2021; Salehin et al., 2025). This decline can be attributed to increased canopy complexity and spectral signatures from multiple species (Holzhauser et al., 2022; Salehin et al., 2025). Holzhauser et al. (2022) demonstrated that UAV-based multispectral VIs yielded only moderate biomass estimation accuracies for mixed cover crops and found that mixture-specific models did not significantly outperform universal models. More recent studies have explored the potential of combining VIs with additional structural information. Salehin et al. (2025), for example, reported improved biomass estimates by combining VIs with UAV-derived canopy height models in multiple regression frameworks. At satellite scale, Bendini et al. (2024) used Sentinel-2 time series and machine learning approaches and achieved promising results for both individual and mixed cover crops, while emphasizing that significant gaps for accurately estimating biomass of mixed cover crops still persist. The use of hyperspectral data to improve biomass estimation due to its higher spectral information content has been identified as promising (Kumar and Mutanga, 2017). Wang et al. (2023) accurately quantified cover crop traits of cereal rye using radiative transfer process-guided machine learning and highlighted the value of hyperspectral observations as reference data for calibrating satellite-based models.

However, studies applying hyperspectral data to biomass estimation in diverse cover crop mixtures remain scarce. Consequently, it remains unclear how well different biomass retrieval approaches perform across cover crop mixtures and to what extent hyperspectral UAV data can support robust biomass estimation under these heterogeneous conditions.

1.2.2 Fractional vegetation cover estimation of cover crops

Fractional vegetation cover describes the proportion of ground surface covered by vegetation with values ranging between 0 and 1. Henceforth, the short form *fractional cover* will predominantly be used. For effective erosion protection through cover crops, yellowed and dead plant material play a critical role in addition to green vegetation and need to be accounted for in remote sensing assessments of fractional cover (Prabhakara et al., 2015).

Remote sensing of green fractional cover is well established for agricultural systems and commonly used approaches include broad-band VIs such as the Normalized Difference Vegetation Index (NDVI) derived from multispectral data (Pereira et al., 2020). For instance, Prabhakara et al. (2015) reported strong relationships between NDVI and percent ground-cover for six winter cover crop species. However, traditional VIs are primarily sensitive to green vegetation and often underestimate total cover in the presence of senescent material or crop residues (Prabhakara et al., 2015). Recent studies have explored the potential of hyperspectral data to differentiate plant residue from bare soil by making use of absorption features related to lignin and cellulose in the shortwave-infrared (SWIR) region. Techniques such as narrow-band spectral indices, Spectral Mixture Analysis (SMA) and machine learning algorithms have been applied successfully to differentiate plant residues from bare soil (Pacheco et al., 2008; Meyer et al., 2017; Yue and

Tian, 2020; Lamb et al., 2025). Nevertheless, most of this research has focused either on green vegetation only or plant residue detection in monocultures. This represents a key research gap for the quantitative assessment of total fractional cover (including non-photosynthetic vegetation) in mixed-species cover crop systems.

1.2.3 Remote sensing methods for cover crop characterization

A range of remote sensing methods has been applied to estimate cover crop biomass and fractional cover, including VIs, SMA, Radiative Transfer Models (RTMs), and purely data-driven machine learning approaches. VIs are the most commonly applied approach due to their simplicity and computational efficiency but reduce the spectral information to a small number of bands, resulting in a loss of physiological information contained in the full spectrum (Adetunji et al., 2020). Their empirical nature further limits robustness and transferability across heterogeneous conditions as encountered for mixed cover crop species (Salehin et al., 2025).

SMA decomposes the mixed reflectance signal of a pixel into fractions of surface types within this pixel, making it particularly relevant for estimation of fractional vegetation cover (Im and Jensen, 2008). However, SMA assumes linear spectral mixing. This assumption can be violated in complex canopies due to multiple scattering, within-canopy shading and structural heterogeneity (Schweiger et al., 2015).

Physically based models are generally said to be more robust and transferable across sites in comparison with empirically based VIs (Li et al., 2023). However, their performance depends on accurate parametrization and can be improved by including in-situ data (Kooistra et al., 2024). RTMs present a class of physically based models that provide a mechanistic link between canopy reflectance and vegetation properties as they describe the interaction between radiation, leaves and canopy structure. PROSAIL is a popular RTM used for retrieving vegetation biophysical and biochemical properties (Jacquemoud et al., 2009). It combines the leaf optical properties model PROSPECT with the canopy reflectance model SAIL. In combination with machine learning based inversion, PROSAIL is used to retrieve Leaf Area Index (LAI) that is directly linked to biomass (Punalekar et al., 2018). LAI is a measure of vegetation density and defined as the ratio of the total area of one-sided green leaves to the underlying soil surface (Im and Jensen, 2008). A key limitation of PROSAIL is the underlying turbid medium assumption, which implies random leaf distribution, no explicit representation of plant structure and canopy homogeneity at pixel scale (Jacquemoud et al., 2009). Recent studies have shown that RTM-inversion-based plant trait retrieval can be critically affected when the canopy deviates from these assumptions, for example due to phenological effects (Schiefer et al., 2021), incomplete vegetation cover or leaf clumping in row crops (Richter et al., 2011, as cited by Berger et al., 2018). Despite these limitations, RMTs remain attractive due to their physical interpretability and potential transferability (Berger et al., 2018). Their applicability to heterogeneous mixed cover crop systems has not yet been systematically evaluated.

Machine learning approaches such as Random Forests or Neural Networks (NNs) can model non-linear relationships between spectral data and vegetation properties and have therefore gained popularity in vegetation monitoring (Im and Jensen, 2008). However, their performance strongly depends on representative training data, which can limit transferability across locations and cover crop mixtures.

All of these methods have specific advantages and limitations, as discussed above. However, several key research gaps remain. The applicability of these methods has rarely been systematically assessed for biomass and fractional cover retrieval in heterogeneous cover crop mixtures, where complex spectral signatures and canopy structure challenge established methods (Kharel et al., 2023; Bendini et al., 2024, as cited in Sale-

hin et al., 2025). Furthermore, as elaborated above, most studies focus either on single-species or evaluate methods in isolation. This makes it difficult to compare their performance under similar conditions. As a result, this limits the understanding of which approaches are most suitable for future operational applications in heterogeneous cover crop systems. Consequently, this study combines hyperspectral UAV data with detailed field reference measurements to evaluate the performance and robustness of different biomass and fractional cover retrieval approaches across varying mixture compositions.

1.3 Research aims, objectives and questions

The overall aim of this thesis is to provide a systematic and comparable assessment of different remote sensing approaches for retrieving above-ground biomass and fractional vegetation cover of mixed cover crop systems under controlled field conditions using hyperspectral UAV data. This study is based on a field experiment designed to include multiple cover crop species mixtures, representing a wide range of species compositions, canopy structures, and phenological conditions. Within this framework, the following **objectives** are defined:

- To acquire high-resolution hyperspectral UAV data and process them into a consistent and reliable dataset.
- To collect high-resolution RGB (Red Green Blue) UAV data and conduct in-situ biomass sampling to obtain reference datasets from an intensive field campaign.
- To estimate above-ground biomass and fractional vegetation cover from hyperspectral UAV data using both band-limited VI approaches and approaches making use of the full-spectral information, including RTMs, SMA and NNs.
- To evaluate and compare the performance of these approaches in mixed cover crop systems.
- To investigate the impact of mixed-species spectral and structural heterogeneity on prediction performance for biomass and fractional cover.
- To assess the robustness and transferability of retrieval approaches using mixture-specific models (trained and applied within individual species mixtures) and across-mixture models (trained on pooled data from multiple mixtures).

Research questions:

RQ1: How accurately can RTM-based approaches predict above-ground biomass of mixed cover crops for individual species mixtures and across mixtures, in comparison to VI-based approaches?

RQ2: How accurately can SMA-based approaches estimate fractional vegetation cover of mixed cover crops for individual species mixtures and across different mixtures, in comparison to VI-based and RTM-based approaches?

RQ3: How precisely can across-mixture NNs predict fractional vegetation cover compared to mixture-specific models, and how does this compare for SMA-, VI-, and RTM-based approaches, all evaluated both in across-mixture and mixture specific settings?

2 Methods

To address the Research Questions (RQs), a field experiment was conducted in Zürich Affoltern. Commonly used cover crop mixtures in Switzerland were sown at different dates throught the summer. During the field experiment, hyperspectral UAV data were collected on seven days covering the full growth period of the cover crops. The experimental setup with two identical mixture strips of different treatments placed next to each other and the flight days selected across various growth stages allowed to capture large heterogeinity within the mixtures in the dataset. The diversity in phenological conditions was intended to improve the robustness of the subsequent modelling to represent real world scenarios. In addition to the hyperspectral acquisitions, RGB UAV imagery and biomass data were collected to provide validation and reference datasets for modelling fractional cover and biomass.

After the data collection, the datasets were processed to derive final predictions of biomass and fractional cover. An overview of the full processing workflow is shown in Figure 2.1. Hyperspectral data were processed into georeferenced and orthorectified reflectance mosaics, while RGB drone imagery was processed into fractional cover reference data. Based on the processed hyperspectral data, features were extracted for each of the four retrieval approaches (VIs, RTMs, SMA, and NNs). To ensure spatial correspondence between the extracted features and the reference data, Region of Interests (ROIs) were selected for subsequent modelling and evaluation. To evaluate RQs 1 and 2, a baseline modelling approach was performed to predict and evaluate biomass and fractional cover. Biomass was estimated using VI- and RTM-based approaches, whereas fractional cover was estimated using VI-, RTM- and SMA-based approaches. To evaluate RQ3, a cross-validated modelling and evaluation scheme was applied to all retrieval approaches.

2.1 Study site and experimental design

2.1.1 Study site

The field experiment was conducted on a test field at Agroscope (Swiss centre of excellence for agricultural research) at the location Reckenholz in Zurich Affoltern (47.43°N, 8.52°E, 444 m a.s.l.). Reckenholz lies in the temperate climate zone of the eastern Swiss Mittelland, with moderate temperatures and precipitation throughout the year. The field site lies in a semi-rural agricultural zone close to the highway and within 5 km of Zurich Airport. The topography is flat and soil types within the field include mainly cambisol and calcaric cambisol and a smaller area with chromic gleysol.

2.1.2 Experimental design

Four common mixtures of cover crops were sown in strips of 50 x 3 m with a sowing row distance of 12.5 cm. Table 2.1 shows the species composition of the mixtures and seeding amount. The mixtures were sown at four different dates between April and August 2025. In the following, the different sowing dates are referred to as treatments. Figure 2.2 shows the study location and the field setup. For each of the four cover crop mixtures, two strips of different treatments were sown next to each other. Within these cover crop strips, plots of 1.5 x 5 m were treated with glyphosate prior to data acquisition on two dates to create controlled brown-vegetation patches. These patches were intended to provided additional information for interpreting model performance. Biomass samples were collected from four sampling plots along each cover crop strip. A detailed map of the soil types within the cover crop strips is shown in Appendix Figure A.1.

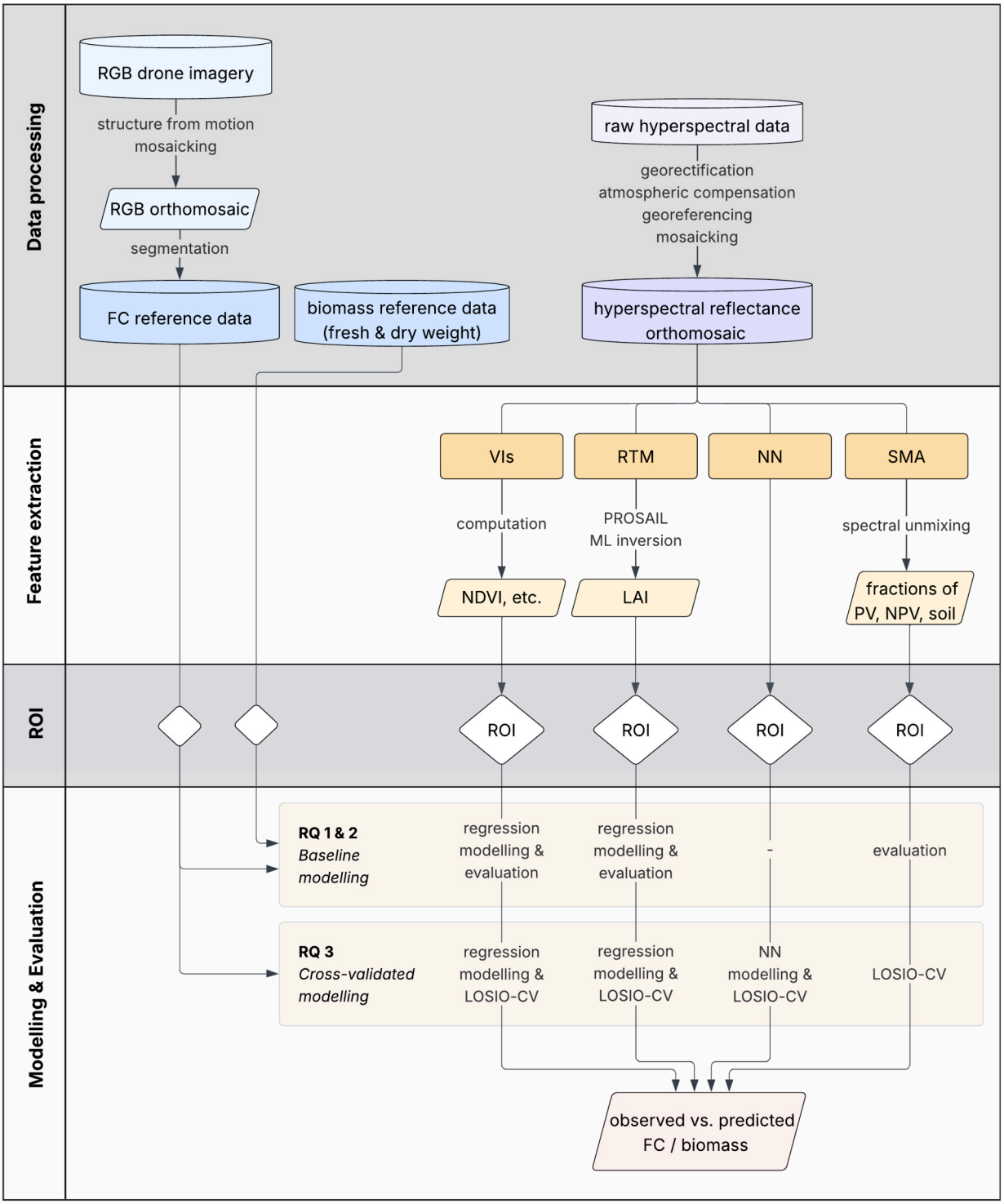

Figure 2.1: Processing workflow for collected datasets, fractional vegetation cover and biomass retrieval approaches, including data processing, feature extraction, ROI aggregation, modelling and evaluation. FC: fractional cover, VIs: vegetation indices, RTM: radiative transfer model, NN: neural network, SMA: spectral mixture analysis, NDVI: Normalized Difference Vegetation Index, ML: machine learning, LAI: Leaf Area Index, PV: photosynthetic vegetation, NPV: non-photosynthetic vegetation, ROI: region of interest, LOSIO-CV: leave-one-strip-instance-out cross-validation.

Table 2.1: Species composition for each cover crop mixture including total seeding amount, seed amount for each species and the short name, used within the thesis.

Mixture	Short name	Species	Seed amount [g/a]
UFA Express (15 kg/ha)	Ex	Buckwheat	50
		Ramtill (Guizotia)	25
		Sorghum	75
UFA Trias (80 kg/ha)	Tr	Berseem clover	100
		Common vetch	200
		Sand oat	500
UFA Humus (30 kg/ha)	Hu	Berseem clover	40
		Common vetch	50
		Forage peas	50
		Summer oat	50
		Sorghum	20
		Phacelia	20
		Bitter lupins	25
		Small-seeded field beans	25
		Summer flax	5
		Sunflowers	10
		Oil radish (multi-resistant)	5
UFA Lepha (30 kg/ha)	Le	Berseem clover	60
		Common vetch	190
		Phacelia	40
		Ramtill (Guizotia)	10

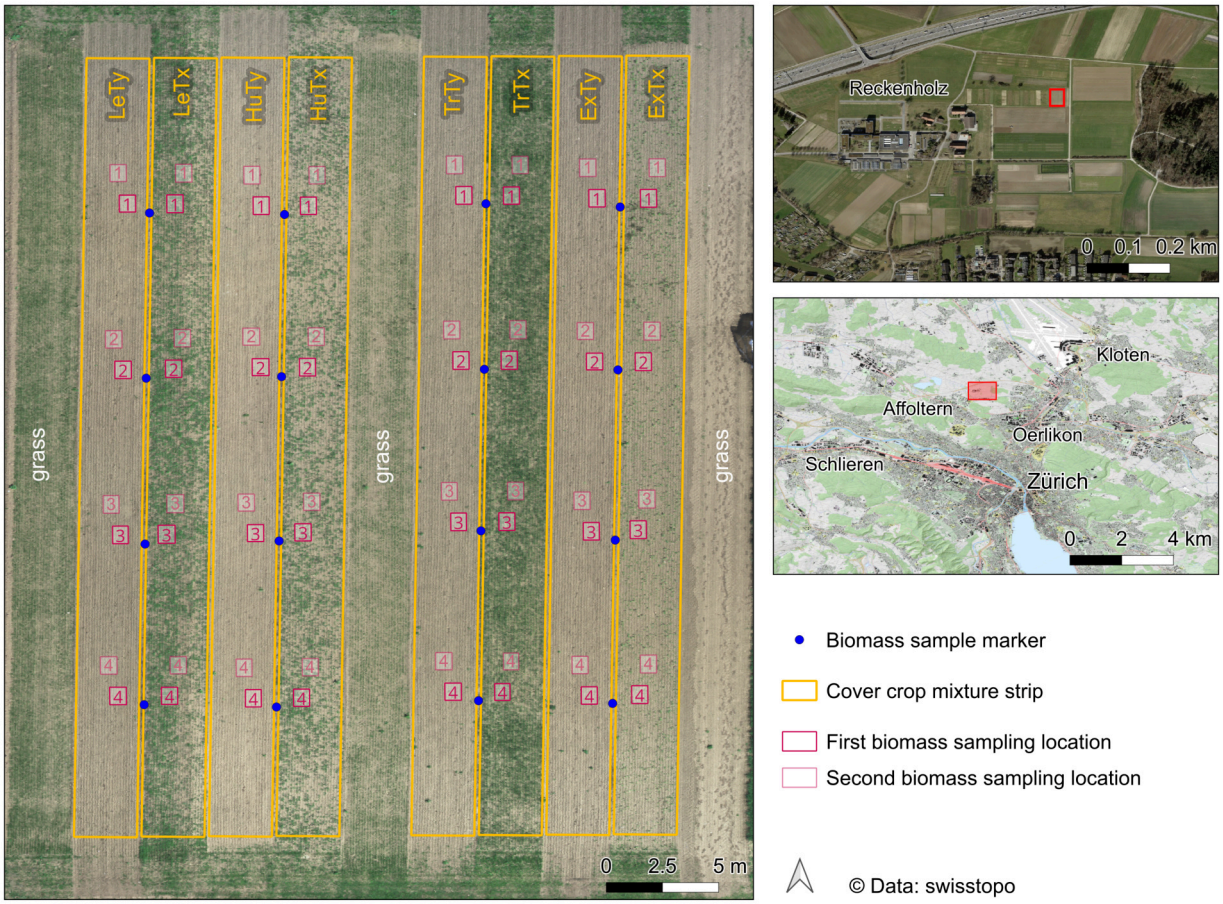

Figure 2.2: Map showing the study location and experimental design. **Left:** Layout of the eight cover crop mixture strips in the field experiment. Mixtures are labelled according to the mixture and sowing date treatments (first letters refer to mixture types, Le: Lepha, Hu: Humus, Tr: Trias, Ex: Express; second letters refer to treatments, e.g., Tx = sowing timing x). Red rectangles indicate biomass sampling locations. **Top right:** Aerial image of the field experiment location Reckenholz. **Bottom:** Wider surroundings including the city of Zurich.

2.2 Data characteristics and acquisition

All datasets were collected between June and September 2025. A list of all datasets and their collection dates is given in Table 2.2. Detailed descriptions for each dataset are provided in the following sections.

Table 2.2: Overview of data collection dates for each hyperspectral UAV (unmanned aerial vehicle) flight, including vegetation composition indicated as treatments T1 - T4, biomass sampling, and RGB UAV acquisitions dates. Biomass sampling was always conducted on the same day as the hyperspectral UAV flight. Below, sowing dates of the four treatments are listed.

HS UAV flight	Treatment	Biomass sampling	RGB UAV flight
2025-06-10	T1, T2	✓: T1, T2	2025-06-11
2025-06-19	T1, T2	✓: T1, T2	2025-06-20
2025-07-17	T2,	✓: T2	-
2025-08-07	T3	✓: T3	2025-08-07
2025-08-13	T3,	-	2025-08-14
2025-09-03	T3, T4	✓: T3	2025-09-03
2025-09-18	T3, T4	✓: T3, T4	2025-09-18
Sowing dates of the different treatments: T1: 2025-04-11, T2: 2025-05-01, T3: 2025-07-10, T4: 2025-08-13			

2.2.1 Hyperspectral UAV data

The hyperspectral UAV data was collected with the HySpex Mjolnir VS-620 line-scanning system (HySpex, Norsk Elektro Optikk, Oslo, Norway). The system consists of co-registered VNIR and SWIR sensors with a 20° field of view. VNIR refers to the visible and near-infrared proportion of the electromagnetic spectrum (∼400 - 1100 nm), whereas SWIR refers to the short-wave infrared region (∼900 - 2500 nm). Together, the sensors cover a spectral range between 400 - 2500 nm with 490 bands. The spectral sampling is 3 nm for the VNIR sensor and 5.1 nm for the SWIR sensor (Norsk Elektro Optikk, 2025). The hyperspectral system was mounted on a NOA 6 hexacopter (Acecore Technologies, Uden, Netherlands). The UAV was equipped with a gimbal for stabilization, an Inertial Navigation System (INS), an Inertial Measurement Unit (IMU) and a Data Acquisition Unit (DAU). Additionally a Velodyne VLP-32 LiDAR sensor was mounted on the system for 3D terrain modelling and point cloud generation.

All flight campaigns followed the same predefined flight plan consisting of three parallel north-south oriented flight lines covering the entire experimental area. Flights were conducted at an altitude of 80 m above ground level, resulting in a ground sampling distance of approximately 4 cm. Data was acquired on eight cloud-free days between 10:00 and 14:00 local time under clear-sky conditions to minimize illumination variability and to ensure consistent conditions across all sampling campaigns. Additionally, four reference panels with different reflectance levels were placed in the field to assess radiometric consistency across acquisitions.

2.2.2 High-resolution RGB UAV data

High resolution RGB imagery was acquired using a DJI Mavic 3E drone, equipped with a wide-angle camera and a tele camera (DJI, Shenzehn, China). The tele camera has a 1/2” CMOS (complementary metal-oxide-semiconductor) sensor with 12 effective megapixels and a 15° field of view (DJI, 2022). Flights were conducted at an altitude of 40 m above ground level using the tele camera with an optical zoom factor of 7, resulting in a ground sampling distance of 0.2 cm. The tele camera was chosen instead of the wide angle camera because of its narrower field of view. This results in less distortion at the edges of the image. All flights followed a predefined flight plan specifying each image capture location to get a forward overlap of 70 % and a side overlap of 60 %, resulting in sufficient redundancy for orthomosaic generation. Images

were captured in nadir view with a continuous autofocus and automatic white balance. RGB flights were carried out on the same day or within one day after the hyperspectral UAV campaigns.

2.2.3 Biomass data

Biomass was collected after the hyperspectral drone flight on the same day. Biomass samples were collected destructively from four rectangular subplots along each cover crop strip (Figure 2.2). The sampled area size was either 1 x 0.5 m or 0.5 x 0.5 m depending on the amount of biomass on the specific sampling campaign. The width of the sampled area was always corresponding to exactly four rows of cover crops. Sampling plots were marked in the field using blue styrofoam balls with a diameter of 7 cm. Those markers were also visible in the hyperspectral UAV imagery, allowing accurate georeferencing of the sampling plots. From each marker, a wooden stick was placed perpendicular to the orientation of the cover crop strip to define the sampling transect (Figure 2.3). To cover different positions along and across the cover crops strips across campaigns and avoid resampling the same area, the sampling position was shifted both along the wooden stick transect and across the cover crop strip by moving the blue markers north-south. The position of each sampling plot in reference to the blue marker was measured in the field using a ruler. All above-ground plant material originating within the sampling frame was cut at ground level and stored in plastic bags. In the laboratory, fresh weight was measured immediately after sampling. Samples were then dried in the oven at 60 °C for 48 h to constant weight and dry biomass was determined. Fresh and dry biomass were both weighted with a digital balance, recording mass to one decimal place (0.1 g). For sampling locations with a fresh weight biomass amount larger than 600 g, subsamples not exceeding 600 g were dried due to space limitations in the oven. Total amount of dry weight for the corresponding locations was derived from the total amount of fresh weight. Both fresh and dry biomass values were normalized by the sampled area and expressed in kg/m². The resulting values served as reference data.

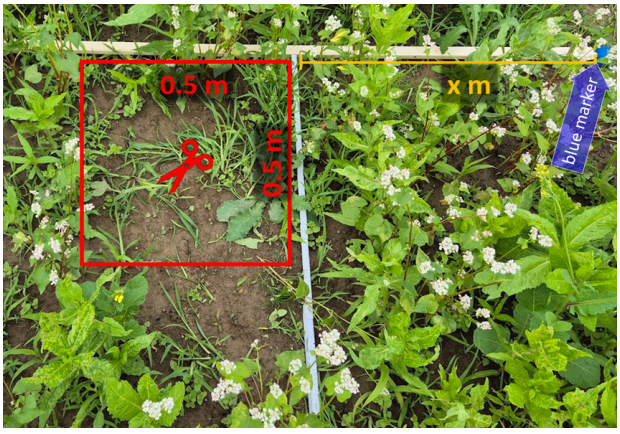

Figure 2.3: Setup for biomass sampling in the field. Blue styrofoam markers visible in the hyperspectral UAV (unmanned aerial vehicle) imagery served as reference points for georeferencing the sampling plots. From each marker, a wooden stick was placed perpendicular to the orientation of the cover crop strips to define the sampling transect. Sampling plots (0.5 × 0.5 m or 1 x 0.5 m) were positioned along these transects using rulers. Between campaings, sampling plots were shifted both along the cover crop strips by moving the blue marker north-south and across the strip by changing the distance x (annotated in yellow) along the wooden stick.

2.3 Data processing

2.3.1 Hyperspectral data processing

Processing the hyperspectral data involved several steps to convert the raw sensor data into georeferenced surface reflectance orthomosaics. The workflow included navigation data post-processing, radiometric calibration, geometric correction, atmospheric compensation, georeferencing and spectral band selection. These steps were essential to ensure accurate spatial, spectral and radiometric quality of the data used for modelling. The orthorectification and reflectance retrieval workflow was initially tested and adapted using the software packages PARGE and DROACOR. Based on this validated workflow, final processing of all datasets was performed using the ReSe Processor (Version 1.4, Build 13, ReSe Applications, Switzerland), which provides an automated and integrated implementation of the same processing steps.

Navigation data processing

The raw GNSS (global navigation satellite system) and IMU data recorded during the flights were post-processed using POSPac UAV (Version 9.3, Applanix, Canada). POSPac compares the UAV GNSS records with the base station data to compute corrections for satellite errors, clock errors and atmospheric delays. These corrections are applied to the UAV navigation data. For our system, ETH2 base station data from AGNES network (Swisstopo, 2025) were used to provide reference positions at known coordinates. POSPac then combines the corrected GNSS data with the IMU measurements to compute precise flight trajectories with accurate positions and orientations of the hyperspectral sensors for each single flight line. Normally, this step reduces positioning errors caused by UAV motion or GNSS drift from about 1 m to a few centimetres (Applanix, 2021).

Digital elevation model generation

The Digital Elevation Model (DEM) is used in the subsequent processing to normalize hyperspectral reflectance data to surface height and for accurate georeferencing of the hyperspectral images. The raw LiDAR data recorded during hyperspectral UAV flights were post-processed using POSPacs LiDAR tools to create georeferenced point clouds. LiDAR point clouds were then rasterized in QGIS (Version 3.40.4, Tool: *Point Cloud Conversion, Export to raster using triangulation*) to the same pixel size as the hyperspectral images for further processing.

Radiometric calibration and navigation synchronization

To receive sensor outputs in physically interpretable radiance values [μW cm^{-2} nm^{-1} sr^{-1}], the raw brightness values (Digital Numbers, DNs) recorded from the HySpex Mjolnir sensors were converted to at-sensor radiance using HySpex RAD (Version 3.5, Norsk Elektro Optikk, Norway). The integration of the corrected navigation data with the hyperspectral image data was performed using HySpex NAV (Version 2.6, Norsk Elektro Optikk, Norway).

Orthorectification

Orthorectification of the hyperspectral images was performed in PARGE (Version 4.1, ReSe Applications, Switzerland) using the corrected and synchronized navigation data and the LiDAR-derived DEM. In this step, image coordinates were transformed to map coordinates (UTM zone 32N, EPSG 32632) and geometric distortions caused by sensor movement, terrain and viewing geometry were removed. Further, this step included merging of the VNIR and SWIR data, to get the full spectral range from 400 to 2500 nm for every pixel. The split band between VNIR and SWIR was chosen at 952 nm as recommended by HySpex.

Reflectance retrieval

Surface reflectance is required for the analysis because it represents the true reflectivity of the surface independent of the state of the atmosphere at the acquisition date and illumination and sensor geometry. The DROACOR reflectance processor tool (Version 2.1 Build 57, ReSe Applications, Switzerland) was used to convert at-sensor radiance to surface reflectance. The software is fully automated and applies a physical reflectance retrieval method using radiation parameters from atmospheric look-up-tables (LibRadtran) to perform the atmospheric compensation (Schläpfer and Popp, 2025). Within DROACOR, the following settings were applied during reflectance processing: a weak spectral polishing (Savitsky Golay Filter, 7-band size) and a detector gap correction, which performs an empirical brightness correction for the jump at the split band in the measured spectra between the VNIR and SWIR sensors (Schläpfer and Popp, 2025).

Georeferencing

Additionaly, a manual georeferencing using Ground Control Points (GCPs) was performed before merging the single flight lines to the final mosaic. This step was needed, because the onboard IMU of the drone performed outside its specified performance range, resulting in reduced navigation accuracy and in a spatial offset of the single flight lines in flight direction. 6 - 15 GCPs were well distributed within the field experiment site and measured with a high-precision RTK-GNSS (real-time kinematic) rover. Each flight line was then georeferenced using the GCPs measured position. After single flightlines were georeferenced, they were merged to the final orthomosaic. GCP accuracy was measured to be within one hyperspectral pixel.

Spectral band selection and removal

Spectral bands affected by low sensor sensitivity at the beginning and end of the spectral range, as well as bands strongly influenced by atmospheric water vapour absorption, were removed prior to analysis following the recommendations provided in the DROACOR processing manual (Schläpfer and Popp, 2025). In addition, minor spectral artifacts were observed around 940 and 2000 nm, which were not related to surface reflectance properties. There artifacts were therefore removed. A dedicated feature optimization addressing these artifacts was later implemented in the ReSe Processor (Daniel Schläpfer, pers. comm.). However, this improvement was not available at the time of this study and was therefore not applied. Specifically, wavelength regions of 400–425 nm, 925–970 nm, 1326–1481 nm, 1785–2015 nm, and 2429–2500 nm were excluded.

2.3.2 RGB data processing

Orthomosaic generation

RGB imagery was processed to orthomosaics for each flight campaign using WebODM (Version 2.8.0, OpenDroneMap ODM, 2020). Before processing, GCPs (as described in Section 2.3.1) were identified in the images to improve georeferencing. WebODM uses a Structure-from-Motion algorithm to detect key features across overlapping images. These features are then used to calculate the camera positions and orientations. A dense point cloud is generated from which the final orthomosaic is generated. Accurate orthomosaics were only retrieved by setting the ground sampling distance manually instead of using WebODMs internal retrieval method. The ground sampling distance was calculated from camera specific parameters (DJI, 2022) and the flight height. With a flight height above ground of 40 m, a sensor width of 6.4 mm, a focal length of 29.85 mm and an image width of 4000 px, a ground sampling distance of 0.21 cm was obtained.

Segmentation of vegetation and soil

To obtain fractional cover reference data between 0 and 1, where 1 indicates 100 % coverage by green vegetation, the RGB orthomosaics were segmented into green vegetation and background pixels. The segmentation was performed using the Field-Level Canopy Cover Model developed and implemented by Boos (2025), which has been shown by Boos (2025) to have an accuracy of 96.5 %. Fractional cover was calculated for each ROI (as defined in Section 2.5) as the ratio between the number of vegetation pixels and the total number of pixels from the binary mask within the corresponding ROI. Figure 2.4 shows for each mixture an excerpt of the high-resolution RGB image together with the created binary mask for green vegetation and the overlay of both.

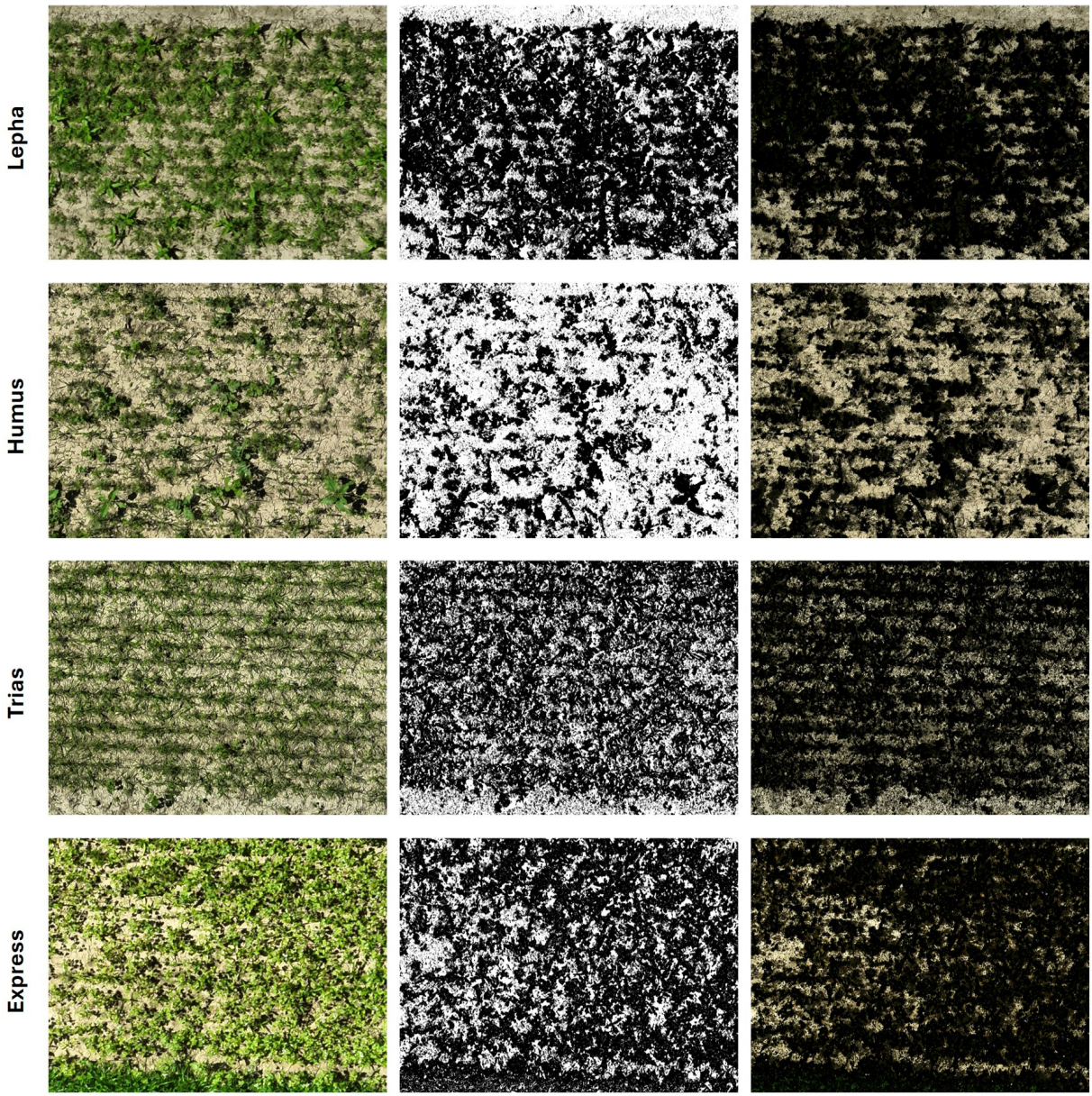

Figure 2.4: Excerpts for each mixture from left to right of the original high-resolution RGB image, the created binary mask for green vegetation (vegetation in black) using the Field-Level Canopy Cover Model and the overlay of the binary mask on top of the original RGB image.

To retrieve reference data for the brown vegetation patches within the cover crop strips, several segmentation approaches were tested to separate brown vegetation from soil. Approaches included HSV-based thresholding, gradient-based segmentation and a local graph-cut method, which is implemented in the MATLAB Image Segmenter App (Version R2025b, MathWorks, USA). The HSV-based approach (Figure 2.5) yielded the most promising results by transforming the RGB images into the Hue, Saturation and Value color space and using manually tuned lower and upper thresholds for brown vegetation. However, segmentation remained insufficient for generating reliable reference data due to image quality constraints and the general difficulty of distinguishing brown vegetation from soil in RGB imagery. Consequently, the brown vegetation patches were not included in the analysis and the subsequently used term fractional cover refers only to the fraction of green vegetation coverage of the soil between 0 and 1.

Figure 2.5: Segmentation of brown vegetation and soil. **Left:** Original image with brown vegetation masked in black. **Middle:** Original image with soil masked in black. **Right:** Original image, extent of RGB image retrieved from Mavic 3E on 2025-08-13.

2.4 Feature extraction

Based on the processed hyperspectral reflectance orthomosaics, spectral features were extracted for the four retrieval approaches (VIs, RTMs, SMA, and NNs) used for biomass and fractional cover estimation.

2.4.1 Vegetation indices

Empirical models, such as VIs and simple band ratios were tested to predict biomass and fractional cover due to their simplicity and widespread use. Different indices were selected based on their specific use cases and their applicability to not only hyperspectral data but also multispectral data. Since the indices were derived from the hyperspectral data using narrow-band wavelengths, this approach is band-limited. This is in contrast to RTM-, SMA-, and NN-based approaches, which use all available bands. These approaches will be referred to as full-spectral approaches in the following.

The NDVI was included as a standard reference index for canopy greenness (Rouse et al., 1973; Tucker, 1979; Huang et al., 2021). Triangular Vegetation Index (TVI) and the modified form Modified Triangular Vegetation Index 2 (MTVI2) together with the Modified Chlorophyll Absoprtion Ratio Index 2 (MCARI2) were tested because they are sensitive to chlorophyll absorption related photosynthetically active radiation (Broge and Leblanc, 2001; Haboudane et al., 2004). MCARI2 and MTVI2 were especially developed for hyperspectral data and they have been shown to perform well as estimators for LAI (Haboudane et al., 2004). As they are mathematically identical, only MTVI2 was used in the further analysis (Nguy-Robertson, 2013). GnyLi was developed for hyperspectral data exploiting reflectance and absoption features caused by the cellular plant structure as well as plant moisture. It has specifically shown good results for biomass estimation (Gnyp et al., 2014; Bendig et al., 2015). Additionally, simple band

ratios and normalized difference indices were included because they are highly correlated with biomass (Im and Jensen, 2008) and have already shown good results for cover crop assessments (Holzhauser et al., 2022).

Vegetation indices were derived from the hyperspectral UAV data on a per-pixel basis, using the bands with the nearest available central wavelength to the theoretical wavelength in the index formula (Table 2.3). Figure 2.6 shows the used wavelengths for corresponding VIs in reference to a reflectance spectrum of a vegetated pixel.

Table 2.3: Overview of the tested vegetation indices with their short names, formulas, used wavelengths, and references.

Name	Abbreviation	Formula	Reference
Normalized Difference Vegetation Index	NDVI	$\frac{R_{800} - R_{670}}{R_{800} + R_{670}}$	Rouse et al. (1973); wavelengths from Haboudane et al. (2004)
Triangular Vegetation Index	TVI	$0.5\,[120\,(R_{750} - R_{550}) - 200\,(R_{670} - R_{550})]$	Broge and Leblanc (2001); wavelengths from Haboudane et al. (2004)
Modified Triangular Vegetation Index 2	MTVI2	$\frac{1.5\,[1.2(R_{800} - R_{550}) - 2.5(R_{670} - R_{550})]}{\sqrt{(2R_{800} + 1)^2 - (6R_{800} - 5\sqrt{R_{670}}) - 0.5}}$	Haboudane et al. (2004)
GnyLi	GnyLi	$\frac{R_{900}R_{1050} - R_{955}R_{1220}}{R_{900}R_{1050} + R_{955}R_{1220}}$	Gnyp et al. (2014)
Simple ratio red	SR_{red}	$\frac{R_{790}}{R_{660}}$	Jordan (1969); wavelengths from Holzhauser et al. (2022)
Simple ratio red edge	$SR_{red\ edge}$	$\frac{R_{790}}{R_{735}}$	Sims and Gamon (2002); wavelengths from Holzhauser et al. (2022)
Red edge Normalized Difference Vegetation Index	$ND_{red\ edge}$	$\frac{R_{790} - R_{735}}{R_{790} + R_{735}}$	Gitelson and Merzlyak (1996); wavelengths from Holzhauser et al. (2022)

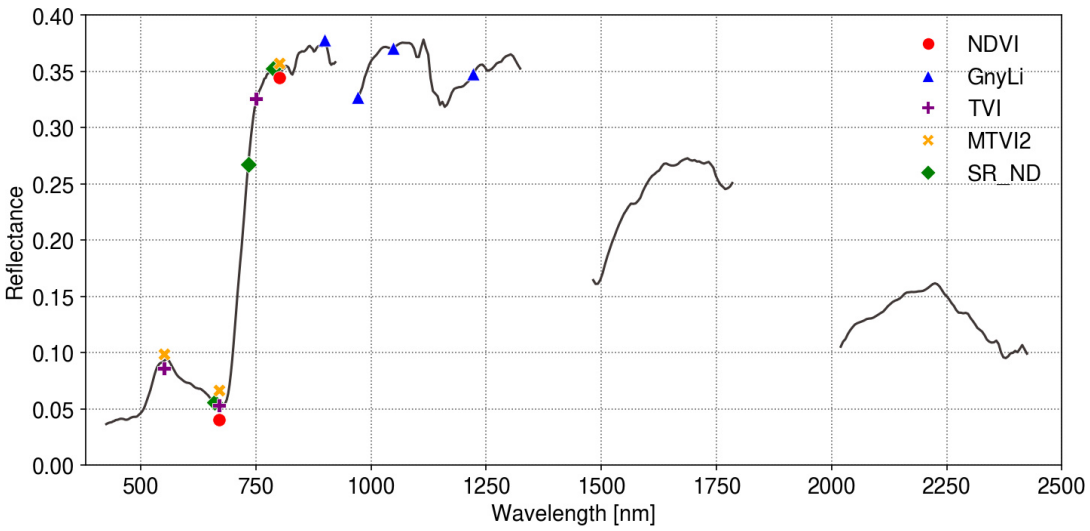

Figure 2.6: Wavelength regions for the vegetation indices marked on the reflectance spectrum of a vegetated pixel derived from UAV (unmanned aerial vehicle) imagery collected on 2025-09-03. NDVI: Normalized Difference Vegetation Index, GnyLi, SR_ND: Simple ratio and normalized difference, TVI: Triangular Vegetation Index, MTVI2: Modified Triangular Vegetation Index 2.

2.4.2 Radiative transfer modelling

The RTM PROSAIL was used to simulate canopy reflectance for defined leaf and canopy parameter ranges (Table 2.4). Cover crop species were supposed to exhibit mostly similar characteristics as grassland species. Thus, vegetation-related parameters, such as leaf biochemical content and structural traits, were set based on commonly reported ranges for grasslands (Asam et al., 2015; He et al., 2019; Wang et al., 2023) and slightly adjusted for the cover crop species characteristics. Canopy and observation-related parameters were adjusted according to the HySpex sensor configuration and the data acquisition conditions (Section 2.2.1). To account for local soil conditions, pure soil reflectances (retrieved as described in Section 2.4.3) were provided to PROSAIL to more representatively simulate background conditions at the study sites.

Model simulations were generated following an approach similar to that described by Ledain, Sélène (2025), using a Python-based package for the radiative transfer modelling by Gomez-Dans (2019). To obtain sensor-specific reflectance comparable to the HySpex Mjolnir observations, the modelled canopy reflectance values were spectrally convolved using spectral response functions. The spectral response functions were represented by Gaussian response functions defined by the center wavelength and full width at half maximum (FWHM) of each HySpex Mjolnir band, as provided by the sensor manufacturer.

Based on the simulated PROSAIL spectra, look-up tables were created containing plant traits and per-band reflectance values for the defined parameter ranges. The pure soil reflectances were added to the look-up tables to provide examples of bare soil (LAI = 0), as they are not simulated by PROSAIL. Simulated reflectances for varying LAI are shown in Appendix Figure A.3. For the inversion step, LAI was predicted from reflectance using a NN, trained on the generated look-up tables. The trained NN was then applied to predict LAI for every hyperspectral pixel.

Table 2.4: Implemented parameter ranges, descriptions, and distributions for PROSAIL (PROSPECT and SAIL).

Parameter	Description	Range	Distribution
PROSPECT			
n	Leaf structure index	1.0–2.1 [unitless]	Gaussian
C_{ab}	Chlorophyll a+b content	15–60 [μg/cm^2]	Gaussian
C_{ar}	Carotenoid content	1.5–15 [μg/cm^2]	Gaussian
C_{ant}	Anthocyanin content	0–5 [μg/cm^2]	Gaussian
C_{brown}	Brown pigment	0–1 [unitless]	Uniform
C_w	Equivalent water thickness	0.001–0.05 [cm]	Gaussian
C_m	Leaf dry matter content	0.002–0.04 [g/cm^2]	Uniform
SAIL			
LAI	Leaf area index	0–8 [m^2/m^2]	Uniform
$LIDF_a$	Leaf angle distribution (a)	20–80 °	Uniform
$LIDF_b$	Leaf angle distribution (b)	0–0 °	Constant
h_{spot}	Hotspot parameter	0.01–0.5 [m/m]	Uniform
r_{soil}	Soil brightness factor	0–1.5 [unitless]	Uniform
p_{soil}	Soil moisture factor	0.5–1.5 [unitless]	Constant
tts	Solar zenith angle	25–60 °	Uniform
tto	Viewing zenith angle	0–10 °	Uniform
ψ	Relative azimuth angle	0–160 °	Uniform

2.4.3 Spectral mixture analysis

The performance of SMA strongly depends on appropriate endmember selection (Pacheco et al., 2008). Endmembers were selected directly from the collected hyperspectral data for green vegetation, brown vegetation and soil. First, a rough endmember selection was done manually by comparing the hyperspectral

data with the high-resolution RGB images and selecting the pixels representing the purest surface. To ensure that the full variability of spectral signatures across the cover crop mixtures were represented in the SMA, endmembers were selected from all cover crop mixtures and across different flight campaigns. Regarding soil endmembers, soil pixels were extracted from all present soil types using the soil map shown in Appendix Figure A.1. The endmember selection was then refined by using indices and thresholds. Green vegetation spectra were chosen based on high NDVI and NIR reflectance values. Selected endmember spectra for each cover crop mixture are shown in Appendix Figure A.4. Soil spectra were chosen based on low NDVI and high red reflectance values. Selected endmember spectra for each soil type are shown in Appendix Figure A.5. Brown vegetation spectra were selected based on the Green Brown Vegetation Index (GBVI). This index captures the absorption regions of dry matter in the SWIR and is positive for brown vegetation and negative for green vegetation (Delegido et al., 2015). All selected endmember spectra are shown in Appendix Figure A.6.

For spectral mixing and unmixing, code implemented by Sélène Ledain following the method of Lobert et al. (2025) was adjusted for the HySpex Mjolnir sensor characteristics. Based on the endmembers and a shade component (reflectance of 0.01 across all bands), 10,000 synthetic mixtures for each cover fraction were created by linear combination (Appendix Figure A.7). Spectral unmixing was performed by training five NNs for each endmember class to improve prediction stability. Prediction results were then averaged over the five iterations. For each hyperspectral pixel, fractions of green vegetation and soil were predicted and normalized such that the sum of their fractions was 1. The brown vegetation fraction was not included, as the analysis focused on green vegetation only and no brown vegetation was considered in the final data.

2.4.4 Neural network input preparation

For the NN-based approach, no explicit spectral feature extraction was applied prior to modelling, in contrast to the approaches described above. Instead, hyperspectral reflectance values were directly aggregated at the ROI level by computing mean spectra for each grid cell corresponding to the fractional cover reference data. The definition of the ROIs and grid cells is described in detail in the following section. Hyperspectral pixels were only included in the aggregation if their centres were within the grid cell boundaries.

2.5 ROI aggregation

To link the reference data with the hyperspectral data, ROIs were defined. For the biomass data, the ROI size corresponded to the size of the biomass sampling plots (0.5 and 0.25 m^2, Section 2.2.3). The biomass sampling location polygons were determined using the blue markers placed in the field and that were clearly visible in the hyperspectral images. The markers were identified by selecting pixels with high reflectance in the blue bands (450–465 nm) and low reflectance in the orange bands (550–610 nm). The positions of the pixels belonging to each marker were clustered, and the centroid of each cluster was used as the marker's precise location. Then, using the field layout and distances measured during each sampling campaign, the sampling plots were positioned along the cover crop strips according to the transect distances measured during each sampling campaign. Potential misalignment between the sampled locations in the field and the calculated locations due to imprecise placement of the measurement devices in the field could not be quantified. For subsequent biomass modelling and prediction, hyperspectral pixel-based VIs (Section 2.4.1) and LAI estimates (Section 2.4.2) were spatially matched to the biomass reference data by averaging all pixel values whose centres fell within the boundaries of the corresponding biomass sampling location polygons.

For the fractional cover data, a georeferencing offset between the RGB and hyperspectral data was evident from the GCPs and the blue markers for biomass sampling, which are present in both data sources. The magnitude of the offset was found to be within 1-2 hyperspectral pixels (4-8 cm). To reduce the impact of this misalignment, a ROI size of 1 x 1 m was selected, ensuring that the spatial offset has only a minor influence on the results. To ensure that data were consistently extracted from the same location on the cover crop strips for subsequent modelling and evaluation across acquisition dates, a fixed grid with a cell size of 1 m^2 was defined for each strip (Appendix Figure A.2).
For the fractional cover prediction, VI-, RTM-, and NN-based approaches included a modelling step. For these approaches, spatial matching between the fractional cover reference data and the extracted features (Sections 2.4.1, 2.4.2 and 2.4.4) was performed analogously to the biomass data, but using the fixed 1 m^2 grid cells. In contrast, the SMA-based approach directly produced green fractional cover estimates at the hyperspectral pixel level (Section 2.4.3). For this approach, the mean fractional cover value was computed for each grid cell by averaging the pixel-level SMA values. These aggregated values were used directly for model comparison without additional modelling.

2.6 Baseline modelling and evaluation

This section describes the baseline modelling and evaluation scheme used to address RQs 1 (biomass) and 2 (fractional cover). For VI- and RTM-based approaches, an additional regression step was applied to relate the extracted and spatially aggregated features to the target variables. For the SMA-based approach, fractional cover estimates were obtained directly from the aggregated unmixing results without an additional modelling step. However, the same evaluation scheme was applied across all three retrieval approaches to allow direct performance comparison.
Several studies have used empirical regression models to relate VIs to biomass and other biophysical parameters. Linear models are commonly used (Du Plessis, 1999; Calvão and Palmeirim, 2004 as cited in Muñoz et al., 2010), other studies found similar or better results by using non-linear models such as exponential regression and power functions (Freeman et al., 2007; Xu et al., 2008; Flynn et al., 2008 as cited in Muñoz et al., 2010). Based on this, linear and non-linear regression was performed to relate the extracted features from VI- and RTM-based approaches to biomass and fractional cover.

2.6.1 Biomass modelling and evaluation

The first RQ targets the accuracy of RTM- and VI-based biomass retrieval methods for individual cover crop species mixtures as well as across different mixtures. Thus the regression modelling and evaluation scheme was performed as described in the following sections for both fresh and dry biomass.

Biomass regression models

For biomass estimation both fresh and dry biomass values were used. Linear models (Equation 2.1) and power function models (Equation 2.2) were tested for each biomass type and retrieval approach. The models were fitted using non-linear least squares optimization implemented in the *curve_fit* function of the SciPy library (Virtanen et al., 2020). For the power function model, initial parameter values were set to $a = max(y)$ and $b = 5$. Parameter bounds were constrained to $a \geq 0$ and $0 \leq b \leq 10$ to ensure physically meaningful solutions. Several data transformations were tested (e.g. log, logit, square-root), but none improved model performance metrics. Therefore, models were fitted using untransformed data.

$$y = ax + b \qquad (2.1) \qquad\qquad y = ax^b \qquad (2.2)$$

Mixture-specific analyses

To compare the performance of the retrieval approaches for the four individual cover crop species mixtures (Lepha, Humus, Trias, and Express), mixture-specific modelling was performed. The procedure was applied separately for fresh and dry biomass, using only data from the respective mixture.

- **VI regression modelling:** For the VI-based approach, seven VIs were derived at the hyperspectral pixel level and subsequently aggregated to the biomass sampling locations (ROIs, Section 2.5), yielding for each VI one predictor value (x in the equations) per ROI. The corresponding biomass reference values (y in the equations) were used for fitting the models. For each mixture, linear and power-law regression models were fitted independently for each VI.
- **RTM regression modelling:** For the RTM-based approach, LAI estimates derived from hyperspectral data were aggregated to the biomass sampling ROIs and used as predictor variables. As for the VI-based approach, linear and power-law regression models were fitted separately for each mixture.
- **Selecting best fitting models:** Regression model performance was assessed during the modelling step. For each feature (individual VIs and LAI), the regression model (linear or power-law) that performed best for the specific mixture was selected based on R^2 and RMSE.
- **Evaluation of retrieval methods:** Biomass was predicted for each ROI by applying the previously selected best-fitting regression models to the corresponding VI- and LAI-derived features. Predictions were generated separately for each of the seven VIs and for LAI, and compared to the observed biomass reference data. For each VI and for LAI, model performance metrics were computed separately for each mixture type. Model performance was quantified using R^2 (coefficient of determination), RMSE, and normalized RMSE (nRMSE), computed from the relationship between predicted and observed biomass values at the ROI level. These metrics were used to evaluate and compare the accuracy of VI- and RTM-based retrieval approaches for specific mixtures.

Across-mixture analyses

To investigate model robustness and transferability under varying species compositions, an across-mixture modelling approach was applied. In contrast to the mixture-specific setup, data from all four cover crop species mixtures were pooled. For each feature (seven VIs and LAI), linear and power-law regression models were fitted using the combined dataset. Model selection and evaluation followed the same procedure as described for the mixture-specific modelling. For each feature, the best-fitting regression model was selected based on R^2 and RMSE. Biomass predictions were then generated for the whole dataset using the selected models and compared to observed biomass values. Model performance was quantified using R^2, RMSE, and nRMSE, enabling direct comparison with the mixture-specific results.

2.6.2 Fractional cover modelling and evaluation

The second RQ targets the accuracy of RTM-, VI-, and SMA-based fractional cover retrieval methods for individual cover crop species mixtures as well as across different mixtures. Thus the regression modelling scheme and evaluation was performed similarly as described above for biomass retrieval. For the SMA-based approach however, no regression modelling was needed and the evaluation scheme was directly applied.

Fractional cover regression models

For fractional cover estimation, linear models (Equation 2.1) and exponential saturation models (Equation 2.3) were tested. As for the biomass regression models, the fitting used non-linear least squares optimization and untransformed data, as data transformations did not improve model performance metrics. For the exponential saturation model, initial parameter values were set to $a = 0.0001$ and $b = 0.0001$. Parameter bounds were defined as $a \geq 0$ and $b \leq 10$.

$$y = a(1 - e^{-bx}) \quad (2.3)$$

Mixture-specific analyses

The mixture-specific modelling was performed as described above for biomass (Section 2.6.1), using only the data from the corresponding mixture. VI and RTM regression modelling was performed using linear and exponential saturation models (Equations 2.1 and 2.3). Predictor values were the derived seven VIs and LAI that were aggregated to the 1 m^2 grid cell ROIs. The corresponding fractional cover reference values were used for fitting the models. Best-fitting models were selected and used for predicting fractional cover. Model performance was quantified using R^2, RMSE, and nRMSE.
For the SMA-based approach, no regression modelling was needed and the evaluation scheme was directly applied. Thus the aggregated SMA-derived fractional cover predictions were compared with the observed fractional cover values separately for each mixture. This mixture-specific comparison was used to quantify the performance of the approach, using R^2, RMSE, and nRMSE.

Across-mixture analyses

Across-mixture fractional cover modelling was performed in the same way as the across-mixture biomass modelling. Data from all four cover crop mixtures were pooled and for the seven VIs and LAI linear and exponential saturation models were fitted on the pooled data. Best fitting models were selected, fractional cover predicted and performance metrics were calculated. For the SMA-based approach, performance metrics were directly computed on the pooled data.

2.7 Cross-validated fractional cover modelling and evaluation

In addition to the baseline modelling and evaluation scheme, a cross-validated modelling and evaluation scheme was applied to the fractional cover retrieval methods. This scheme addresses RQ3, which focuses on the performance of NNs for fractional cover estimation in comparison to VI-, RTM- and SMA-based approaches for mixture-specific and across-mixture models.

A NN modelling approach was tested because of their ability to handle high-dimensional hyperspectral data and to deal with non-linear properties (Im and Jensen, 2008), which are expected in heterogeneous mixed cover crop canopies. To ensure a robust evaluation of NN performance, cross-validation was applied, as machine learning methods are prone to overfitting data in small datasets. As discussed by Sun et al. (2024), k-fold cross-validation reduces the risk of biased performance estimations that can occur when model evaluation is based on a single, potentially unrepresentative subset of the data. By rotating the validation set across multiple folds, this approach allows assessing the variability within the full dataset.

Cross-validation was consistently applied to all retrieval approaches, including SMA-, RTM-, and VI-based fractional cover retrieval methods to ensure a fair and comparable evaluation framework. This evaluation

strategy closely reflects real-world application scenarios, in which models are typically trained for a specific period of time or location and then applied to independent conditions that were not observed during model training.

2.7.1 Neural network modelling architecture

A small fully connected neural network was implemented in PyTorch to predict fractional cover directly from hyperspectral reflectance (Paszke et al., 2019). Input features were mean reflectance values of each 1 m^2 grid cell (Section 2.5). The model consists of three fully connected layers (48, 24, and 12 neurons), each followed by batch normalization, ReLU activation and dropout regularization. The final layer returns a fractional cover value between 0 and 1. The architechture was selected to balance predictive capacity with robustness and to reduce overfitting.
Before training, input features were standardized using a StandardScaler fitted on the training set only. The network was trained using the Smooth L1 loss function and the Adam optimizer. Training used mini-batches of size 32 for up to 50 epochs, with early stopping when validation loss did not improve for 10 consecutive epochs.

2.7.2 Dataset splitting

To perform cross-validation for the mixture-specific models, each mixture dataset was split into 10 folds, where each fold corresponds to a single strip instance. This strip instance contains all aggregated 1 m^2 fractional cover observations and extracted features of one cover crop strip of a specific treatment acquired an a specific flight date. Figure 2.7 shows the dataset splits for each mixture (single-mixture dataset) into strip instances with their mean fractional cover and number of observations. Differences in the number of observations between strip instances occurred despite the use of a regular spatial grid. These differences resulted from cases where biomass sampling was conducted prior to RGB UAV acquisition, from which fractional cover reference data were derived. Grid cells affected by this mismatch of canopy state between hyperspectral observations and fractional cover reference data were excluded from the analysis.

The balanced across-mixture dataset (also shown in Figure 2.7) was used for evaluating the retrieval approach performances across mixtures. It was created by splitting the full dataset containing data from all mixtures into strip instances that matched the size and structure of those in the single-mixture datasets. To ensure that the across-mixture strip instances remained comparable in size with the mixture-specific models, only one quarter of the observations from each mixture-specific strip instance was included. To avoid over- or underrepresentation of any area within a cover crop strip, observations were selected using regular spatial subsampling along each cover crop strip. This balanced sampling pattern is illustrated by the orange grid cells in Appendix Figure A.2.

2.7.3 LOSIO-Cross-Validation and performance assessment

Based on the dataset splitting into strip instances corresponding to cover crop strips of a specific treatment and acquired on a specific flight date, the applied leave-one-strip-instance-out cross-validation scheme is called LOSIO-CV in the following. LOSIO-CV was applied independently to all retrieval approaches for both the single-mixture datasets and the balanced across-mixture dataset.

Mixture-specific vs. across-mixture LOSIO-CV

For mixture-specific LOSIO-CV, models were trained on all strip instances of a given mixture-specific dataset except one, and validation was performed on the full left-out strip instance. In contrast, across-

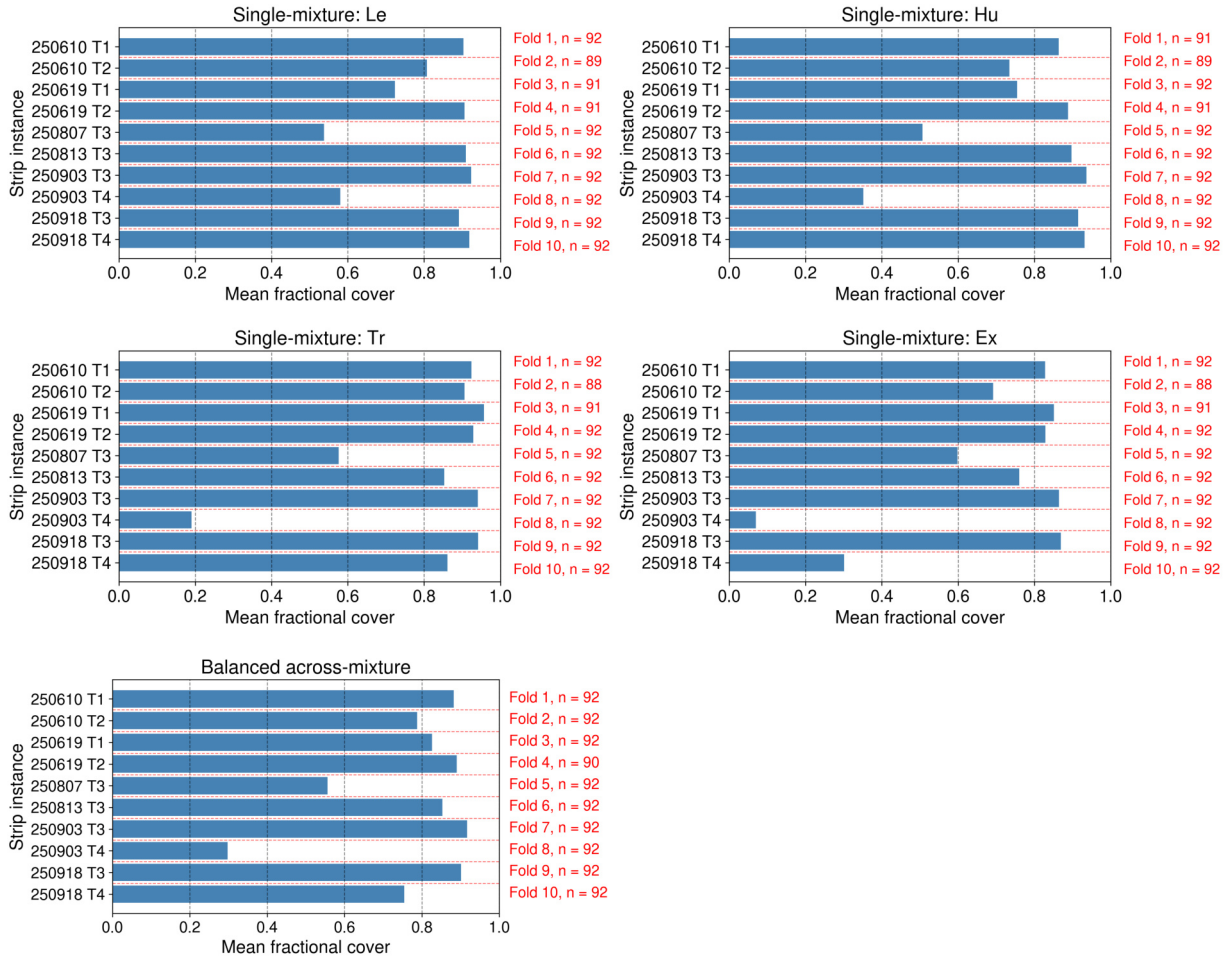

Figure 2.7: Dataset splits for single-mixture (Le: Lepha, Hu: Humus, Tr: Trias, Ex: Express) and the balanced across-mixture dataset. Mean fractional cover is displayed for each strip instance (cover crop strip of specific date and treatment). Strip instances are labelled according the fold number used in LOSIO-CV (leave-one-strip-instance-out cross-validation). The size of each strip instance subset is indicated in red (n = number of observations).

mixture LOSIO-CV models were trained on all strip instances of the balanced across-mixture dataset except the left-out one. Each left-out strip instance contained observations from all mixtures, and model predictions were evaluated separately for each mixture within the held-out strip instance using global performance metrics as described below.

Global statistics

LOSIO-CV performance was evaluated for all applications consistently using global statistics. To assess performance across all folds, the predictions from each left-out strip instance in the procedure were combined into a single dataset. Each prediction was generated by a model trained without the corresponding strip instance, to ensure independence of the evaluation. Global metrics were then computed as follows:

$$R^2_{\text{global}} = 1 - \frac{\sum_{j=1}^{m}\sum_{i=1}^{n_j}(y_{ij} - \hat{y}_{ij})^2}{\sum_{j=1}^{m}\sum_{i=1}^{n_j}(y_{ij} - \bar{y}_{\text{global}})^2} \tag{2.4}$$

$$\text{RMSE}_{\text{global}} = \sqrt{\frac{1}{\sum_{j=1}^{m} n_j}\sum_{j=1}^{m}\sum_{i=1}^{n_j}(y_{ij} - \hat{y}_{ij})^2} \tag{2.5}$$

$$\text{nRMSE}_{\text{global}} = \frac{\text{RMSE}_{\text{global}}}{y_{\text{max,global}} - y_{\text{min,global}}} \tag{2.6}$$

where:

- y_{ij}, $\hat{y}_{ij}$ = observed and predicted values for sample i in strip instance j
- n_j = number of samples in strip instance j
- m = total number of strip instances
- $\bar{y}_{\text{global}}$ = is the mean of all observed values across all strip instances
- $y_{\text{max,global}}$, $y_{\text{min,global}}$ = maximum and minimum observed values across all strip instances

This approach follows Linnenbrink et al. (2024), who recommend evaluating cross-validation model performance on the stacked out-of-sample predictions. Reason for this is, that individual folds can have an unbalanced fractional cover distribution, which leads to a bias in the statistic, if fold performances were averaged. Computing global metrics across all folds ensures, that all samples contribute equally to the model performance.

NN LOSIO-CV

Within the LOSIO-CV framework, NN models were trained and evaluated as follows. For each fold, one strip instance was held out as the validation set, while the remaining strip instances were used for training. Input standardization was performed independently for each fold, with the StandardScaler fitted on the training data only and applied to the corresponding validation data. For each fold, the NN architecture and training procedure described in Section 2.7.1 were used. Model predictions were generated for the held-out strip instance and stored for subsequent performance assessment. After completing all folds, predictions from all validation folds were pooled and compared to the corresponding reference fractional cover values to compute global performance metrics as described above.

VI- and RTM-based LOSIO-CV

Fractional cover modelling for VI- and RTM-based approaches within the LOSIO-CV framework followed the same regression formulations as described in the baseline modelling and evaluation section for fractional cover (Section 2.6.2). For the VI-based approach, only the best-performing VI was considered, together with the corresponding regression formulation (linear or exponential saturation) identified during the baseline mixture-specific and across-mixture modelling. Regression models were fitted using training data from all strip instances except the held-out one. For each fold, regression models were trained independently for the best performing VI and for LAI derived from RTM approach. The fitted models were then applied to the held-out strip instance to generate fractional cover predictions. Predictions of all folds were pooled and performance metrics were computed as described above.

SMA-based LOSIO-CV

The SMA-based approach did not involve an explicit modelling or training step, as fractional cover was retrieved directly from spectral unmixing. Nevertheless, LOSIO-CV was applied to the SMA results to ensure comparability with the other retrieval approaches. For each fold, fractional cover estimates from the held-out strip instance were treated as validation data, while no parameter fitting was performed on the remaining strip instances. Performance assessment was conducted by stacking fractional cover estimates from all validation folds and computing the same global performance metrics as for the other approaches using the observed fractional cover reference data. This ensured that performance metrics were derived from the same observations as used for the VI-, RTM-, and NN-based approaches.

3 Results

3.1 Hyperspectral data quality

To evaluate the quality of the hyperspectral data and the effects of the different processing steps, first the changes of the spectral signal and corresponding images from raw sensor signal to radiance and finally to surface reflectance were examined. Further, to give an impression of the final reflectance data, pixel spectra for different surface types and reference panels are shown.

Figure 3.2 shows individual vegetation pixel spectra outputs for different processing steps. The raw DNs recorded by the two sensors for VNIR and SWIR show the uncalibrated values. Physically meaningful at-sensor radiance were retrieved through radiometric calibration and are shown for the two individual sensors, as well as after the merging of the two sensor spectra. A small gap around 952 nm is visible at the sensor split. Illumination-independent reflectance values retrieved through atmospheric compensation show two minor peaks around 940 nm and 2000 nm. The final reflectance spectra were produced by removing these peaks and the noisy bands at the beginning and end of the spectral range.

Visual changes in the images between processing steps are shown for the second flight line scenes of the 2025-09-03 acquisition (Figure 3.3). The raw scenes show the original outputs of the VNIR and SWIR sensors, including distortions caused by platform movement. Detector striping visible in the raw SWIR scene was removed in the radiance SWIR scene. The rectified reflectance scene shows the image corrected for geometric distortions. The final orthorectified reflectance mosaic shows the combination of the three single flight scenes. The spatial accuracy of the hyperspectral data was checked using GCPs placed in the field and was found to be within one pixel (about 4 cm).

Example reflectance spectra from different surface types, including vegetation, shaded vegetation, bare soil and concrete, showed the expected spectral shapes and differences between surfaces classes (Figure 3.1). The reflectance values were within the expected range for these surfaces. Reference panel reflectance values remained largely stable across all acquisition dates, except for the flight on 2025-07-17 (Figure 3.4). Retrieved median panel reflectance spectra on this specific date showed reflectance up to 10% higher than on the other dates.

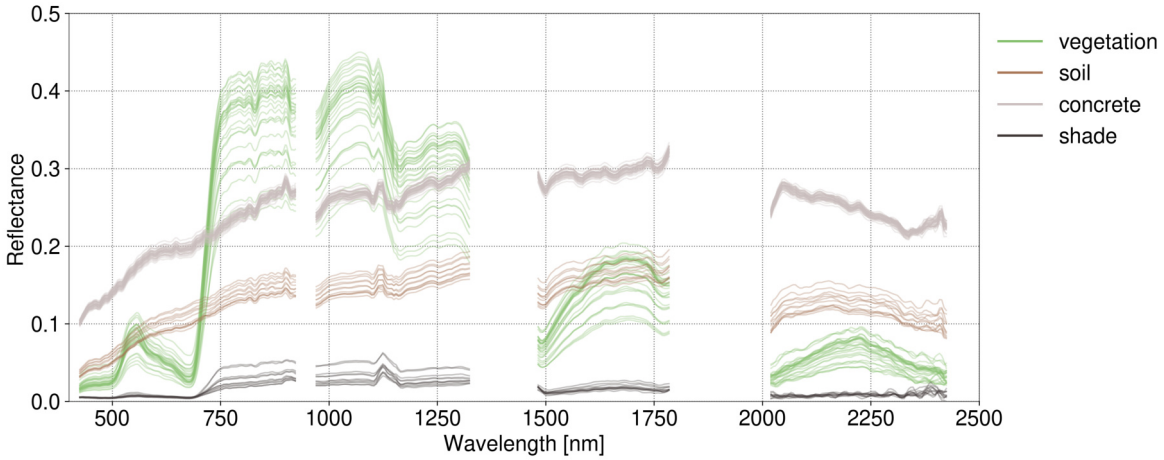

Figure 3.1: Example pixel spectra retrieved from flight 2025-09-03 for the surface type classes vegetation (including grass and cover crops from the Express mixture), soil, concrete and shaded vegetation.

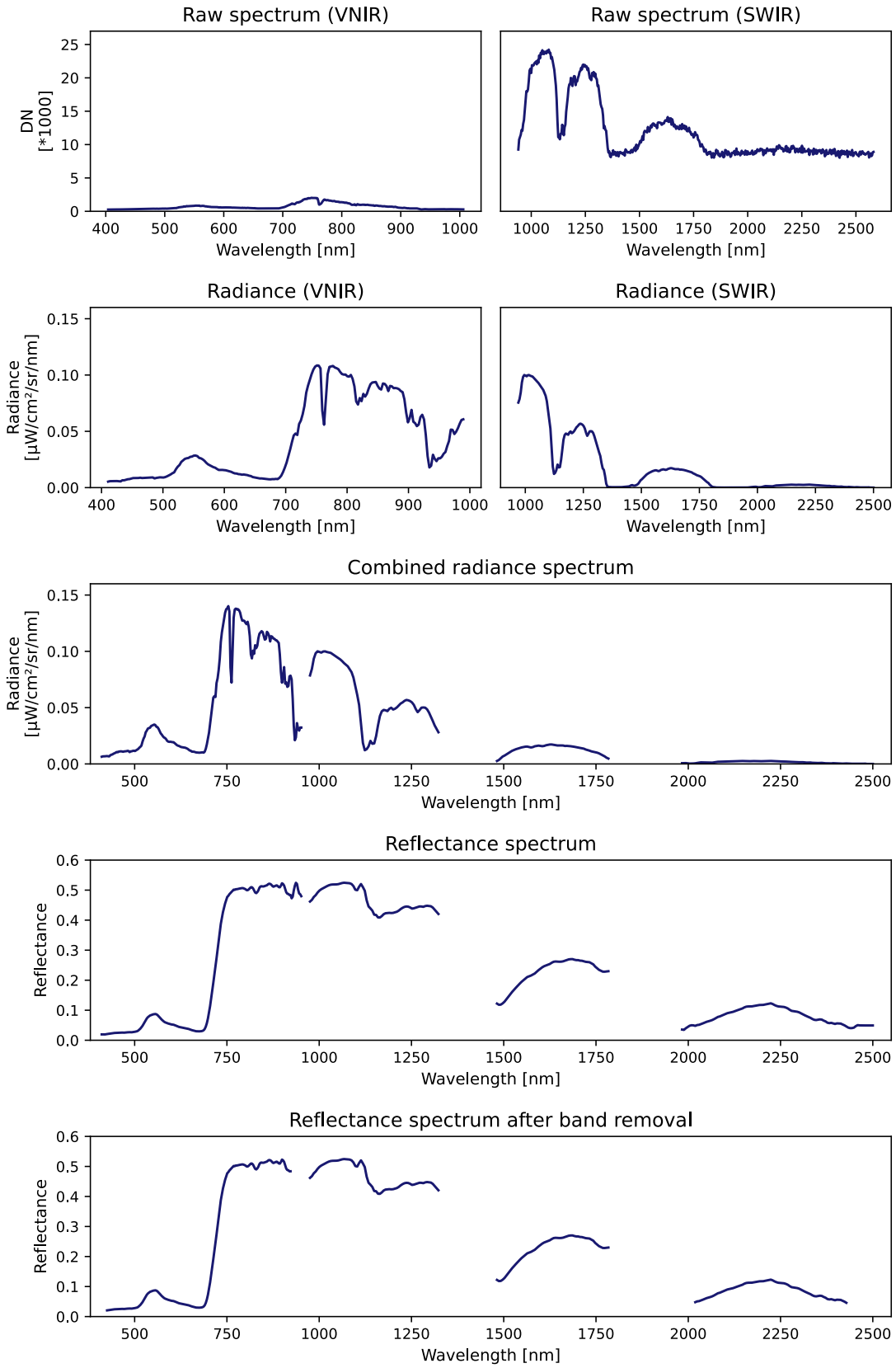

Figure 3.2: Radiometric processing outputs: DN (digital number), radiance and reflectance spectra. Representative single-pixel spectra extracted from the 2025-09-03 flight, show how the raw signal at the sensor is transformed into at-sensor radiance and final surface reflectance through radiometric calibration and atmospheric compensation at successive processing stages. VNIR: Visible and Near Infrared proportion of the light, SWIR: Short Wave Infrared proportion of the light. The VNIR sensor has a 12-bit and the SWIR sensor a 16-bit radiometric resolution (Norsk Elektro Optikk, 2025).

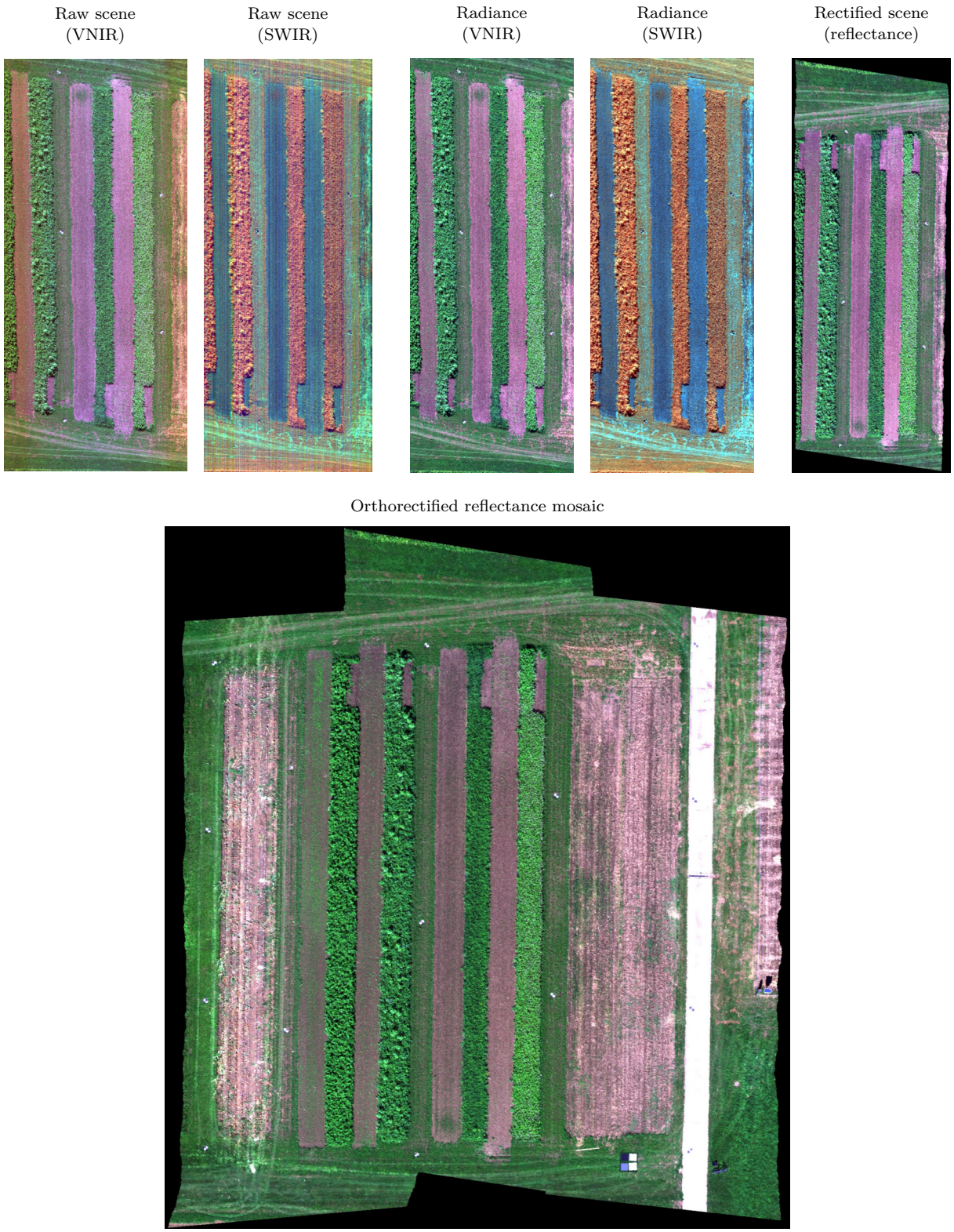

Figure 3.3: Processing effects on hyperspectral imagery. Visual comparison of the second flight line scene extracted from the 2025-09-03 flight across successive processing stages to the final geocoded and rectified orthomosaic. Radiometric processing reduces illumination differences and removes striping visible in the raw SWIR image. Geometric distortions present in the raw and radiance images are corrected, and the individual flight lines are placed with their proper geographic positions in the final orthomosaic. Band combinations for visualizations are for VNIR: 650-550-440 nm and for SWIR: 1077-1650-2250 nm. VNIR: Visible and Near Infrared proportion of the light, SWIR: Short Wave Infrared proportion of the light.

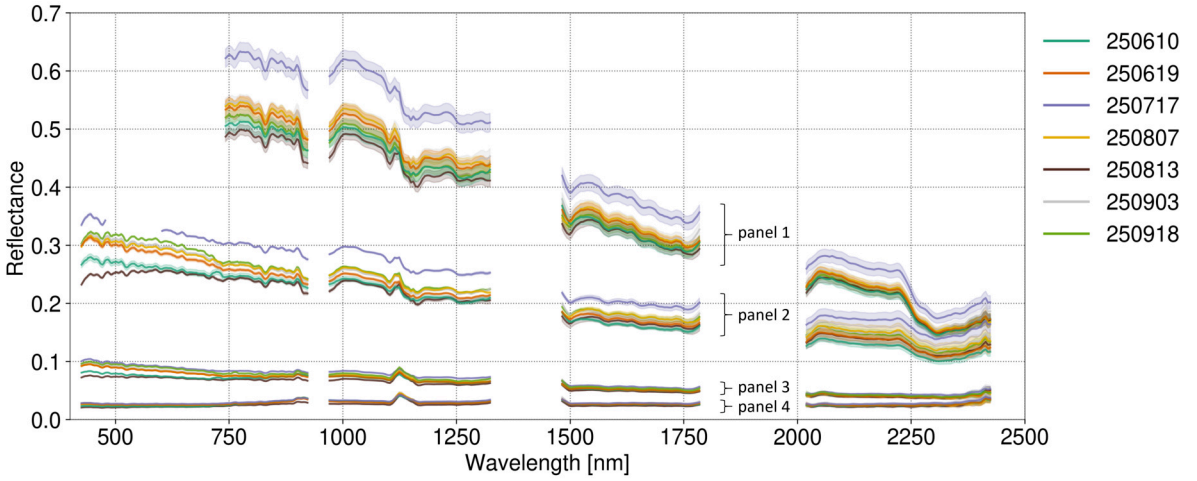

Figure 3.4: Comparison of four reference panel spectra (white to dark gray) across all hyperspectral UAV acquisitions (median reflectance of panel pixels and standard deviation). The missing data for panel 1 in the visible range is due to sensor saturation. The labels correspond to acqusitions dates (YYMMDD, e.g. 250610 = 2025-06-10).

3.2 Fractional cover reference data

The fractional cover reference dataset captured a wide range of canopy conditions across all mixtures, from sparse vegetation coverage to nearly complete ground coverage. Reliable segmentation of brown vegetation from soil was not possible from the collected high-resolution RGB imagery (as described in Section 2.3.2). Mean values of green vegetation fractions and standard deviation across all collected data for the mixtures are close to each other, with Express: mean = 0.63 (std = 0.25), Trias: mean = 0.76 (std = 0.23), Humus: mean = 0.75 (std = 0.20) and Lepha: mean = 0.79 (std = 0.16). Express had the lowest mean vegetation coverage, whereas Lepha reached the highest mean vegetation coverage with the lowest variability.

To illustrate these patterns, Figure 3.5 shows the distribution of the fractional cover observations for each mixture and each strip instance (mixture strip of specific treatment and collection date). Frequency histograms show the number of observations for fractional cover bins. For all mixtures, most data was collected for high fractional cover above 0.6. Especially for Lepha, only few observations were collected below a fractional vegetation cover of 0.4. The figure also includes distributions for the balanced across-mixture dataset, which was used for LOSIO-CV modelling to address RQ3, and the full dataset, which was used for across-mixture-models to address RQ2.

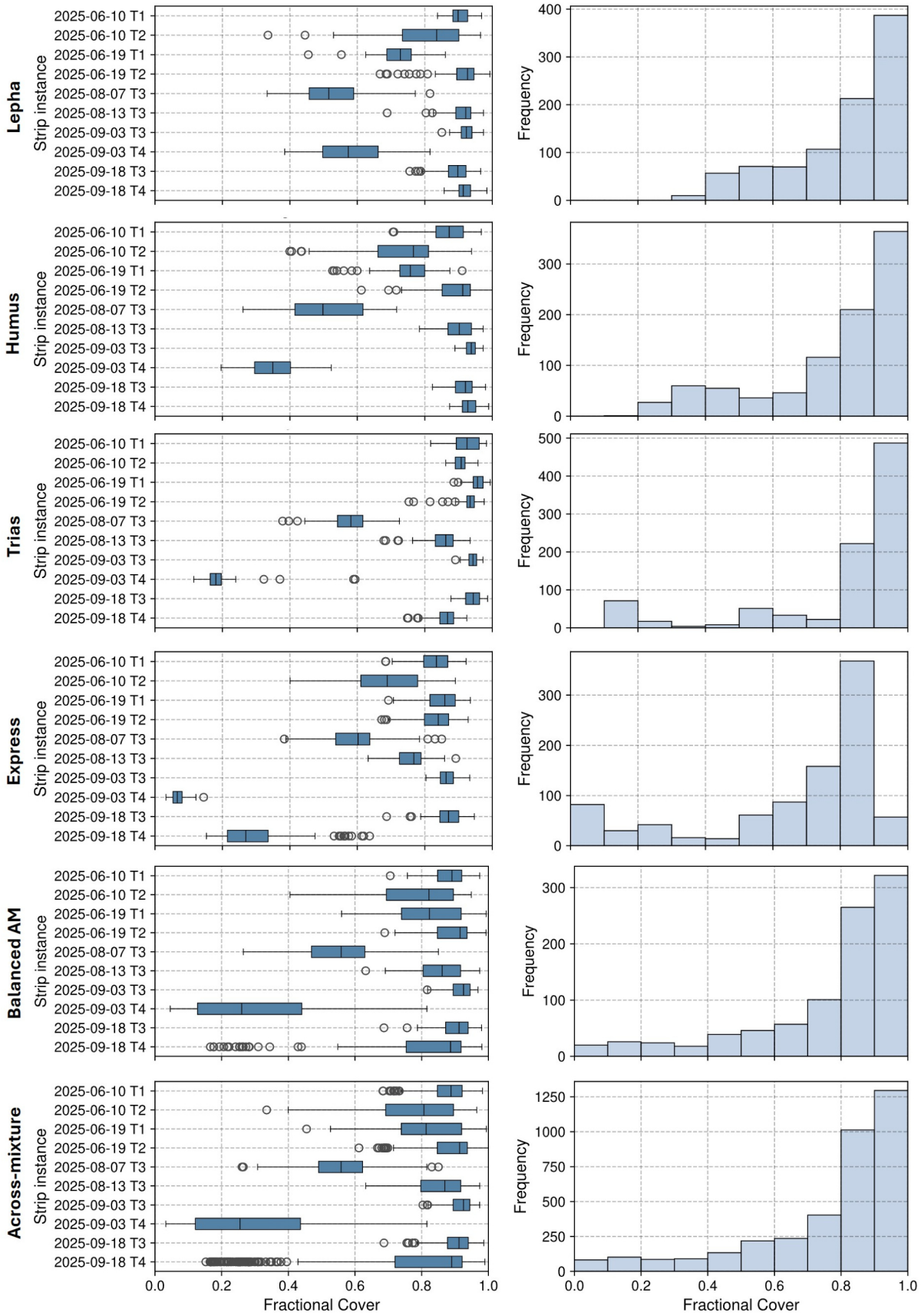

Figure 3.5: Dataset characteristics of fractional vegetation cover for each mixture as well as the balanced across-mixture (Balanced AM) and the across-mixture datasets. **Left:** Boxplots showing the distribution of fractional cover reference measurements for each mixture and strip instance (median, quartiles and data spread). **Right:** Frequency distribution (number of observations) of fractional cover values for each mixture across all observations.

3.3 Biomass reference data

Fresh and dry biomass data included a wide range of values for all mixtures (Figure 3.6). Fresh weight biomass values range from approximately 0.05 to 5 kg/m^2 and dry weight biomass values range from about 0.01 to 1 kg/m^2. The highest biomass values occured in the mixture Lepha, followed by Humus. These two mixtures also showed a greater variability, indicated by wider interquartile ranges and longer whiskers in the boxplots.

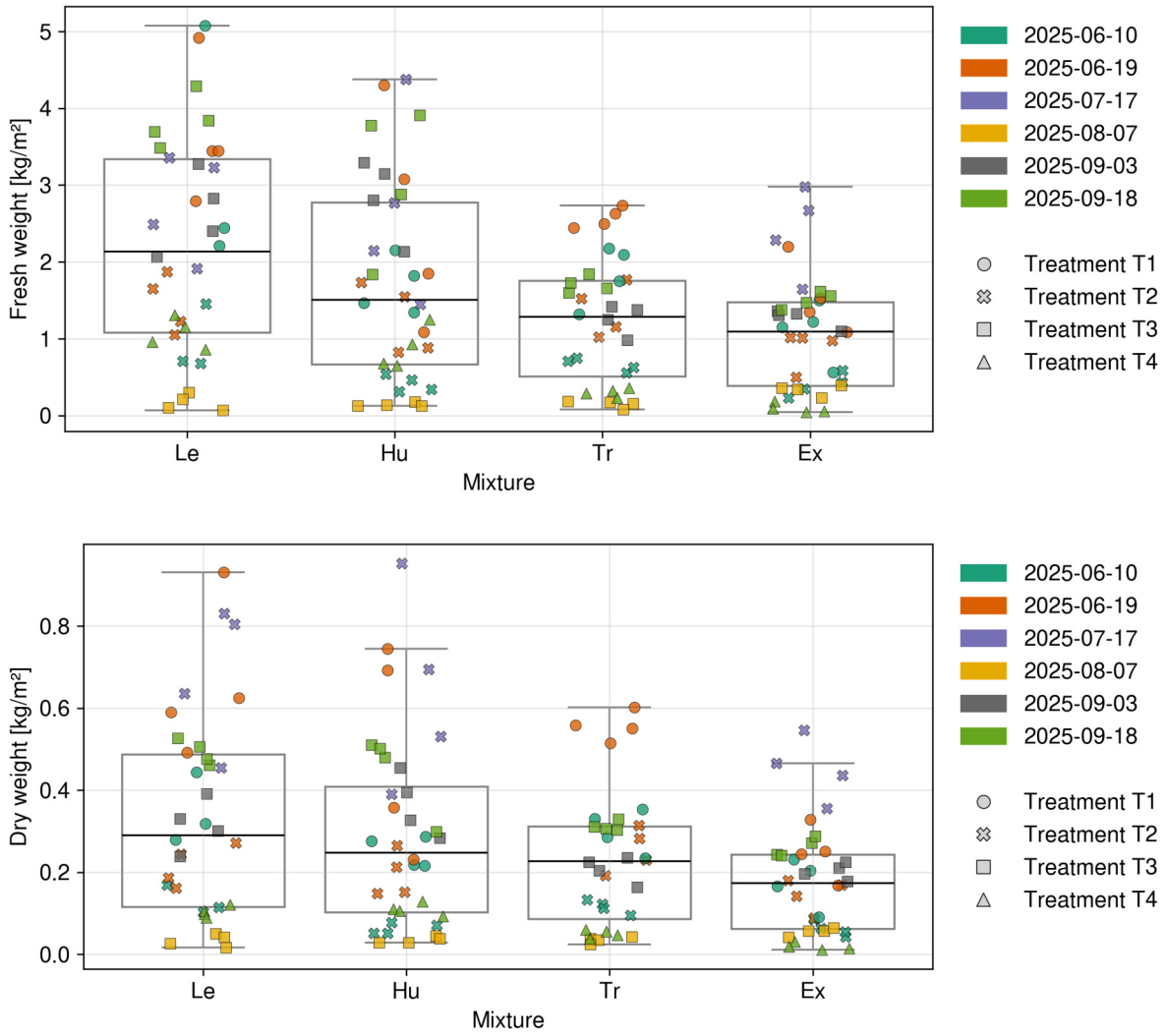

Figure 3.6: Distribution of biomass data. **Top:** Boxplots of fresh weight biomass for each mixture. **Bottom:** Boxplots of dry weight biomass for each mixture (median, quartiles and data spread). Colours indicate the sampling date and shapes indicate the treatment of the respective sample. Le: Lepha, Hu: Humus, Tr: Trias, Ex: Express.

3.4 Performance of RTM- and SMA-based feature extraction

Evaluation of the neural networks for RTM inversion and spectral unmixing was performed on separately generated test datasets. The NN trained on the generated look-up tables for RTM inversion (Section 2.4.2) retrieved LAI with an R^2 of 0.86 and a RMSE of 0.87 on the test set. For spectral unmixing, NNs predicted green fractional vegetation, brown fractional vegetation and fractions of soil with average R^2 values of 0.99, 0.93, and 0.95, and average RMSEs of 0.02, 0.06, and 0.05, respectively (averaged over five networks per class as described in Section 2.4.3).

3.5 Performance of biomass retrieval approaches

RTM- and VI-based approaches were compared to estimate biomass in mixed cover crops using baseline modelling and evaluation. Biomass was modelled separately for fresh and dry weight and both linear and power-law regression functions were applied to seven tested VIs as well as to RTM-derived LAI. Regression models were fitted separately for each mixture type (Lepha, Humus, Trias, and Express) and using pooled data across mixtures, and subsequently used to predict biomass. Model performance was evaluated in a mixture-specific and an across-mixture framework and quantified using R2 (coefficient of determination), RMSE, and nRMSE by comparing predicted values to the corresponding biomass reference data. The results of the mixture-specific and across-mixture biomass evaluations are summarized in Table 3.1 for RTM-based and the three best-performing VI-based approaches. Full tables of all VI-based evaluations for fresh and dry weight are available in the Appendix (Tables B.1 and C.1).

Table 3.1: Performance of fresh and dry weight biomass retrieval approaches for mixture-specific and across-mixture models displayed for radiative transfer models (RTM), and the three best performing vegetation indices: Normalized Difference Red Edge ($ND_{RedEdge}$), Simple Ratio Red Edge ($SR_{RedEdge}$) and GnyLi. The *Mean* column shows the average of performance metrics across the mixture-specific models (Le: Lepha, Hu: Humus, Tr: Trias, Ex: Express). Metrics include R^2, RMSE (kg/m^2), nRMSE (%) and the regression function used (linear or power).

		Fresh weight biomass models						Dry weight biomass models					
		Across-mixture	Mixture-specific					Across-mixture	Mixture-specific				
Approach	Metric		Le	Hu	Tr	Ex	Mean		Le	Hu	Tr	Ex	Mean
RTM	R2	0.45	0.50	0.47	0.90	0.77	0.66	0.34	0.19	0.25	0.85	0.77	0.52
	RMSE	0.86	0.96	0.90	0.26	0.35	0.62	0.17	0.22	0.20	0.06	0.06	0.13
	nRMSE	0.17	0.19	0.21	0.10	0.12	0.16	0.18	0.24	0.21	0.11	0.12	0.17
	fit	pow	pow	pow	pow	pow	-	pow	pow	pow	pow	lin	-
$ND_{RedEdge}$	R2	0.43	0.75	0.66	0.79	0.62	0.70	0.38	0.45	0.49	0.72	0.64	0.58
	RMSE	0.88	0.68	0.72	0.36	0.45	0.55	0.16	0.18	0.16	0.09	0.08	0.13
	nRMSE	0.17	0.14	0.17	0.14	0.15	0.15	0.17	0.20	0.18	0.15	0.15	0.17
	fit	lin	lin	lin	pow	lin	-	lin	lin	lin	pow	lin	-
$SR_{RedEdge}$	R2	0.41	0.75	0.67	0.80	0.61	0.71	0.36	0.43	0.49	0.71	0.63	0.56
	RMSE	0.89	0.69	0.72	0.36	0.46	0.56	0.16	0.18	0.16	0.09	0.08	0.13
	nRMSE	0.18	0.14	0.17	0.13	0.16	0.15	0.17	0.20	0.18	0.15	0.15	0.17
	fit	lin	lin	lin	lin	lin	-	lin	lin	lin	lin	lin	-
GnyLi	R2	0.60	0.64	0.53	0.82	0.66	0.66	0.49	0.36	0.42	0.79	0.60	0.54
	RMSE	0.74	0.82	0.85	0.34	0.43	0.61	0.15	0.19	0.17	0.07	0.08	0.13
	nRMSE	0.15	0.16	0.20	0.13	0.15	0.16	0.16	0.21	0.19	0.13	0.16	0.17
	fit	pow	pow	pow	pow	lin	-	pow	pow	pow	pow	lin	-

3.5.1 Linear vs. power-law regression

For RTM-derived LAI, linear and power-law regressions fits performed very similarly for fresh and dry biomass, with power-law regression resulting in slightly better R2 and RMSE values.
In contrast, the regression fits for VI-based models were not consistent. Depending on the index, the mixture and fresh versus dry weight fitting, some mixtures were better described by linear models, while others showed improved performance with power functions. All regression fitting plots for LAI and VIs are included in the Appendix (Figures B.1-B.3 and C.1-C.3).

3.5.2 Mixture-specific biomass models

Across all mixtures and retrieval approaches, fresh weight biomass was generally predicted with higher accuracy than dry weight biomass, as indicated by consistently higher R^2 values (Table 3.1). However, relative differences between RTM- and VI-based approaches were largely consistent for both biomass types. For dry weight biomass, RTM-based models showed strong performance for the mixtures Trias and Express with R2 values of 0.85 and 0.77 and nRMSE values of 11 and 12 % but weak performance for Lepha and Humus (R2 values = 0.19 and 0.25, nRMSEs = 24 and 21 %). In contrast, VI-based approaches, particularly $SR_{RedEdge}$ and $ND_{RedEdge}$, performed more robustly across all mixtures and achieved comparatively better results for Lepha and Humus.

3.5.3 Across-mixture biomass models

Across-mixture models generally showed lower predictive performance for both fresh and dry biomass compared to the average of the mixture-specific models. Among all tested approaches, the GnyLi index achieved the highest across-mixture performance, with an R^2 of 0.60 for fresh biomass and 0.49 for dry biomass and nRMSE values of 15-16 %. For average mixture-specific dry weight biomass models, R2 ranged between 0.52 and 0.54, with nRMSE of 17 %.

3.5.4 Prediction errors and saturation patters

All models showed a tendency to overpredict low biomass values and underpredict high biomass values, particularly in the mixtures Lepha and Humus, where observed biomass was highest (see also distribution of observed biomass in Section 3.3). For RTM and GnyLi, underprediction of high biomass started around 0.4 kg/m², whereas $ND_{RedEdge}$ and $SR_{RedEdge}$ better predicted biomass up to 0.5–0.6 kg/m² before also underpredicting higher values. These patterns are shown in the predicted versus observed plots in the Appendix (Figures B.4-B.6 and C.4-C.6).

Scatterplots of dry biomass versus the four retrieved traits for mixture-specific and across-mixture models are shown in Figure 3.7. Across all traits, high dry weight biomass values above 0.4 kg/m² were associated with increased scatter and saturation. For RTM-derived LAI, a subset of samples with high biomass at moderate LAI values of approximately 2-3 originated from the 2025-06-10 (treatment 1) and 2025-07-17 (treatment 2) acquisitions. Phenological characteristics and within-mixture heterogeneity for all acquisitions are displayed in Appendix Table A.1. For the mentioned acquisitions, the mixtures were characterized by pronounced within-mixture heterogeneity, including variations in plant size, leaf development and the presence of flowering plants. In the Lepha and Humus mixtures, violet flowers of Phacelia were clearly visible, whereas the Trias mixture exhibited grain structures of oat plants during the acquisition on 2025-06-10. Strongest saturation effects were observed for NDVI, as shown in the regression fit scatterplots (Appendix Figures B.2 and C.2).

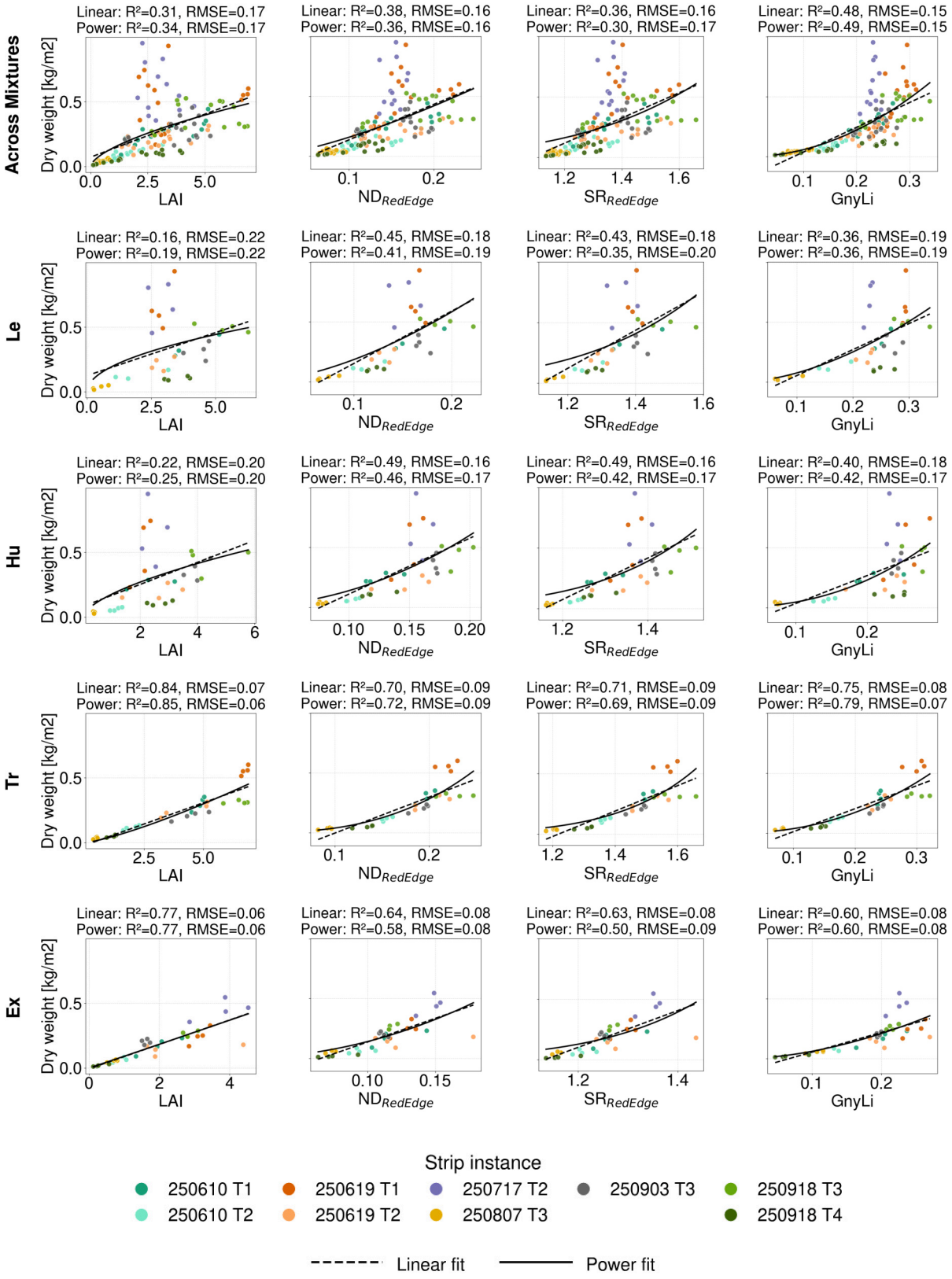

Figure 3.7: Scatterplots of dry weight biomass versus retrieved traits from radiative transfer model based approaches and the three best performing vegetation indices. Displayed from left to right are: Radiative transfer model derived Leaf Area Index (LAI), Normalized Difference Red Edge ($ND_{RedEdge}$), Simple Ratio Red Edge ($SR_{RedEdge}$) and GnyLi. Displayed from top to bottom are the across-mixture models, as well as the four mixture-specific models (Le: Lepha, Hu: Humus, Tr: Trias, Ex: Express). Performance of the linear regression vs. power function is evaluated with R^2, RMSE and nRMSE.

3.6 Performance of baseline fractional cover retrieval approaches

Three approaches (VIs, RTMs, and SMA) were compared using the baseline modelling and evaluation scheme. For VI- and RTM-based retrieval, both linear and exponential saturation functions were fitted separately for each mixture and using the pooled data across mixtures. The regression models were then used to predict fractional cover. Model performance was evaluated in a mixture-specific and across-mixture framework and quantified using R^2, RMSE and nRMSE. For SMA, performance metrics were directly retrieved by comparing the aggregated fractional cover predictions from the spectral unmixing against the reference data.

3.6.1 Linear regression vs. exponential saturation

Figure 3.8 shows scatterplots of fractional cover versus the independent variables for the RTM-based approach and the NDVI and MTVI2 indices, for all mixture-specific and across-mixture models. Points are coloured according to the specific strip instance (date and treatment) and linear versus exponential saturation fits are shown. For RTM-derived LAI, exponential saturation provided the better fit with the fractional cover reference data. All plots show strong saturation of LAI for high fractional coverage above 0.8 and thus better suitability of exponential saturation. Similarly, for most VIs such as MTVI2 and SR_{red}, exponential saturation provided the better fit. An exception was NDVI, where data points showed more scattering and no clear saturation was present. Fits for all VIs are shown in Appendix Figures D.1-D.3.

3.6.2 Mixture-specific fractional cover models

The performance of the mixture-specific and across-mixture fractional cover retrieval approaches is shown in Table 3.2 for SMA, RTM and the three best performing VIs. Complete results for all VI-based models are available in the Appendix (Table D.1). Across all mixtures, VI-based approaches achieved the highest predictive performance. MTVI2 showed the strongest overall results with an average R^2 of 0.90, followed by TVI and NDVI. Prediction errors for these VIs were consistently low, with mean nRMSE values of 7-9 %. RTM-based fractional cover retrieval performed slightly worse than the three best-performing VIs but sill showed very strong predictive ability, with an average R^2 of 0.86 and a nRMSE of 9 %. In contrast, SMA showed moderate performance for the mixture-specific models, with an average R^2 of 0.46 and substantially higher prediction errors (average nRMSE = 18 %). Performance of the retrieval approaches varied between mixtures. Express was generally the best-predicted mixture across the retrieval approaches, followed by Trias, whereas Lepha consistently showed the lowest performance. SMA exhibited almost no explanatory ability for Lepha (R^2 = -0.01), with a high nRMSE of 24 %. RTM- and VI-based approaches, however, still achieved good results for Lepha, with R^2 values above 0.74.

3.6.3 Across-mixture fractional cover models

For RTM- and VI-based approaches, across-mixture models were fitted and evaluated on pooled data from all mixtures. For SMA, no across-mixture modelling was performed, and predicted fractional cover was directly evaluated using all observations. The predictive performance of the across-mixture models was comparable to or even higher than the performance of the averaged mixture-specific models. MTVI2 achieved the highest across-mixture performance with an R^2 of 0.91 and nRMSE of 7 %. RTM-based retrieval also performed strongly in the across-mixture framework and was comparable with NDVI and TVI, with an R^2 value of 0.88 and nRMSE of 8 %. Consistent with the mixture-specific results, SMA performed substantially worse in comparison to the other retrieval approaches, with an R^2 of 0.59 and nRMSE of 15 %.

Table 3.2: Performance of fractional cover retrieval methods for mixture-specific and for across-mixture models, displayed for spectral mixture analysis (SMA), radiative transfer models (RTM) and the three best performing vegetation indices: Modified Triangular Vegetation Index 2 (MTVI2), Triangular Vegetation Index (TVI) and Normalized Difference Vegetation Index (NDVI). Metrics include R2, RMSE, nRMSE and the regression function used (linear or exponential saturation). Included in the *Mixture-specific* column is the mean of the four model performance metrics for Lepha (Le), Humus (Hu), Trias (Tr) and Express (Ex).

		Across-mixture	Mixture-specific				
Approach	Metric		Le	Hu	Tr	Ex	Mean
SMA	R2	0.59	-0.01	0.52	0.52	0.82	0.46
	RMSE	0.15	0.16	0.14	0.16	0.11	0.14
	nRMSE	0.15	0.24	0.18	0.19	0.12	0.18
	best fit	none	none	none	none	none	-
RTM	R2	0.88	0.74	0.86	0.93	0.92	0.86
	RMSE	0.08	0.08	0.08	0.06	0.08	0.07
	nRMSE	0.08	0.12	0.09	0.07	0.08	0.09
	best fit	exp	exp	exp	exp	exp	-
MTVI2	R2	0.91	0.77	0.90	0.97	0.97	0.90
	RMSE	0.07	0.07	0.06	0.04	0.04	0.05
	nRMSE	0.07	0.11	0.08	0.05	0.05	0.07
	best fit	exp	exp	exp	exp	exp	-
TVI	R2	0.89	0.74	0.89	0.95	0.96	0.89
	RMSE	0.08	0.08	0.07	0.05	0.05	0.06
	nRMSE	0.08	0.12	0.08	0.06	0.06	0.08
	best fit	exp	exp	exp	exp	exp	-
NDVI	R2	0.89	0.78	0.87	0.90	0.95	0.88
	RMSE	0.08	0.07	0.07	0.07	0.06	0.07
	nRMSE	0.08	0.11	0.09	0.08	0.06	0.09
	best fit	exp	exp	lin	exp	lin	-

3.6.4 Predicted vs. observed fractional cover

Predicted vs. observed fractional cover for SMA-, RTM-, and MTVI2-based across-mixture and mixture-specific models is shown in Figure 3.9. Complete results for all approaches are provided in Appendix Figures D.4-D.6. MTVI2-based models showed the tightest clustering around the 1:1 line. RTM-based models slightly overpredicted low fractional cover values (< 0.4) and showed a plateau at high observed values (> 0.8), indicating saturation. A similar, but less pronounced, saturation effect was observed for MTVI2. Lepha and Trias exhibited stronger plateauing than the other mixtures, corresponding to observations from 2025-06-19 (treatment 1) and 2025-09-18 (treatment 3 and 4). Model performance varied across acquisition dates and treatments, as indicated by the distinct colour clusters in the plots. For SMA, performance strongly depended on the strip instance. Some instances substantially underestimated fractional cover, whereas others showed saturation effects similar to RTM. Predictions for Express showed better agreement with the 1:1 line than the other mixtures, indicating higher prediction accuracy.

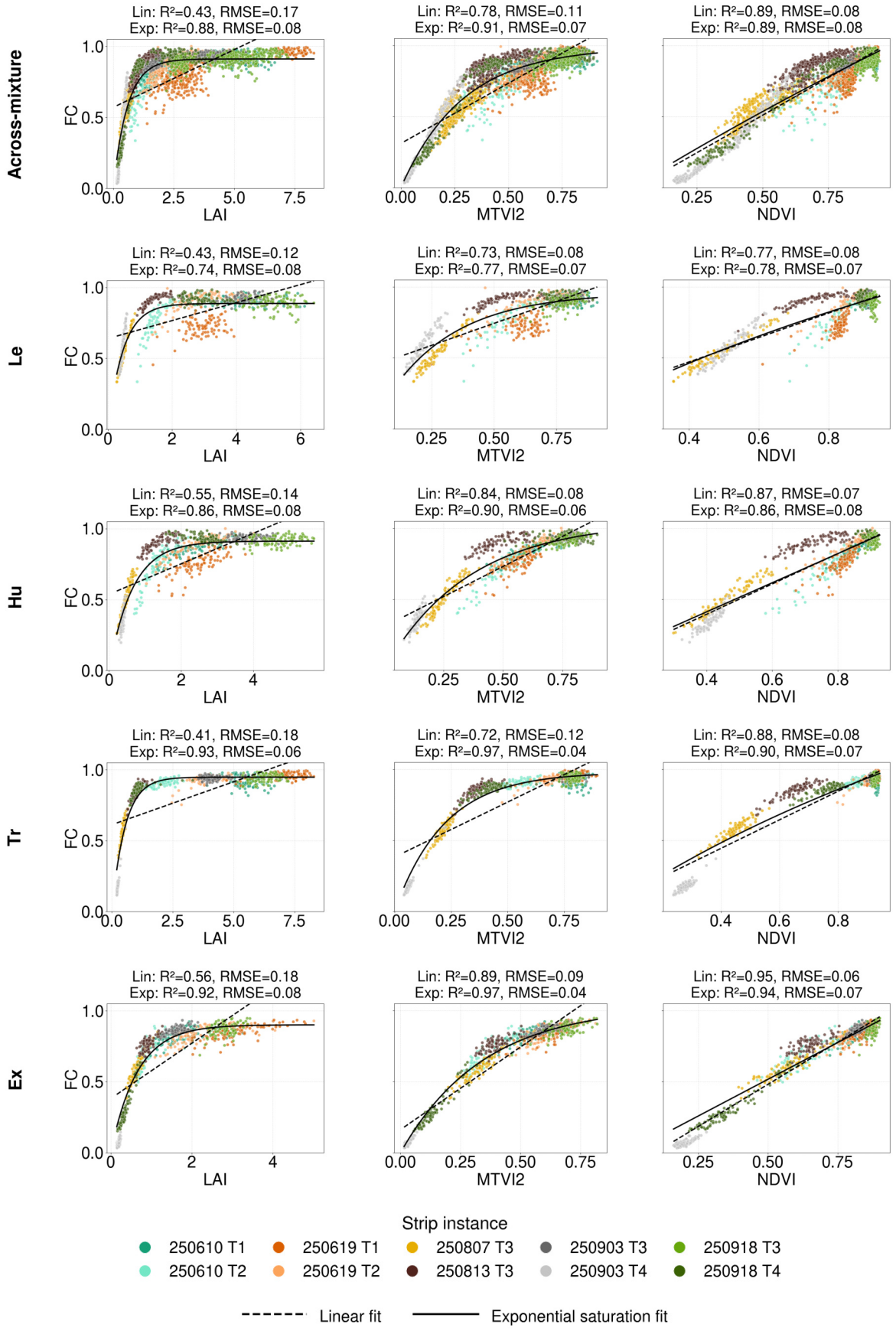

Figure 3.8: Fractional cover scatterplots and linear vs. exponential regression fits for selected retrieval methods. **Left:** Radiative transfer model derived Leaf Area Index (LAI), **middle:** Modified Triangular Vegetation Index 2 (MTVI2), **right:** Normalized Difference Vegetation Index (NDVI). Displayed from top to bottom are across-mixture models and the four mixture-specific models (Le: Lepha, Hu: Humus, Tr: Trias, Ex: Express). Performance of the linear regression versus exponential saturation is evaluated with R^2, RMSE and nRMSE.

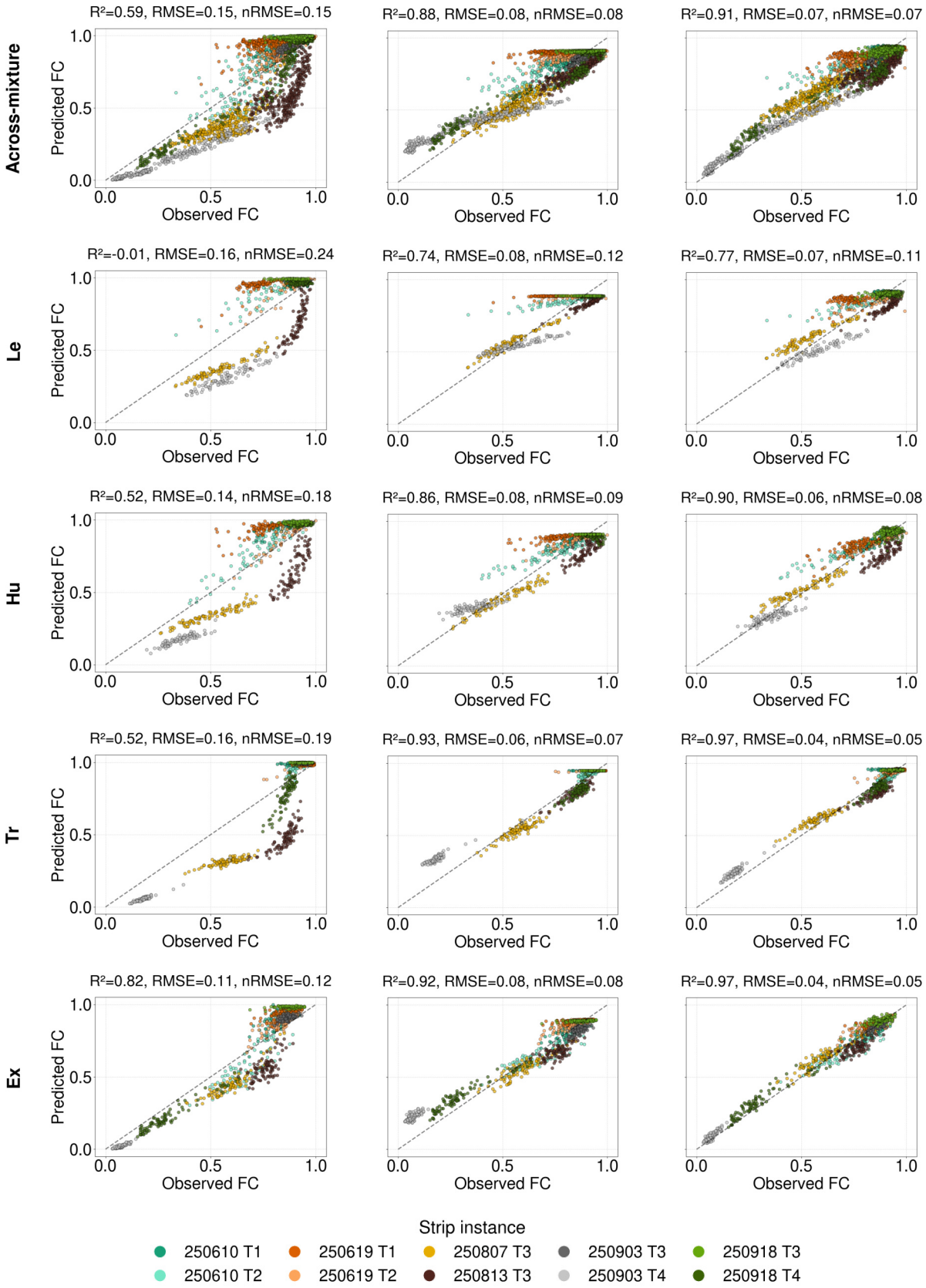

Figure 3.9: Predicted versus observed scatterplots of across-mixture and mixture-specific models for fractional cover retrieval methods. **Left:** Spectral mixture analysis (SMA), **middle:** Radiative transfer model (RTM), **right:** Modified Triangular Vegetation Index 2 (MTVI2). From top to bottom are the across-mixture plots, followed by the mixture-specific plots for Lepha (Le), Humus (Hu), Trias (Tr), and Express (Ex).

3.7 Performance of fractional cover retrieval approaches under LOSIO-CV

This section presents the results of the NN-based fractional cover retrieval evaluated using the LOSIO-CV framework. NN performance is reported for mixture-specific LOSIO-CV (mixture-specific datasets) and for across-mixture LOSIO-CV using the balances across-mixture dataset. For mixture-specific LOSIO-CV, models were trained within individual mixtures and evaluated on complete left-out strip instances. For across-mixture LOSIO-CV, predictions for the held-out strip instances were evaluated separately for each mixture. Results are compared to VI-, RTM-, and SMA-based fractional cover retrieval approaches evaluated under the same LOSIO-CV scheme, using global R^2, RMSE, and nRMSE metrics. For the VI-based approach, only MTVI2 was considered, as it showed the best performance for fractional cover estimation in the baseline evaluation (Section 3.6). The resulting global performance metrics for each mixture, for both the mixture-specific and across-mixture models, are presented in Table 3.3.

For the mixture-specific NN models, the mean performance across all mixtures was good (R^2 = 0.69, nRMSE = 14 %), but lower than that of the RTM- and MTVI2-based models. For Lepha, Humus, and Express, the mixture-specific NNs achieved performance comparable to the RTM- and MTVI2-based models. In contrast, performance for Trias decreased substantially, with a nRMSE of 21 % and an R^2 of 0.41. NN across-mixture models performed similarly to the RTM-based across-mixture models, achieving an overall mean R^2 of 0.82. Contrary to expectations, across-mixture NNs provided better predictions for Lepha, Humus and Trias than the mixture-specific models. Mixture-specific NN models outperformed the across-mixture models only for Express.

Table 3.3: Global performance metrics (R^2, RMSE, nRMSE) for fractional cover retrieval methods under leave-one-strip-instance-out cross-validation for following approaches: Radiative transfer model based Leaf Area Index (LAI), vegetation index based Modified Triangular Vegetation Index 2 (MTVI2), neural networks (NN) and spectral mixture analysis (SMA). Mean values for mixture-specific and across-mixture models are included. Mixtures: Lepha (Le), Humus (Hu), Trias (Tr) and Express (Ex).

		Mixture-specific					Across-mixture				
Approach	Metric	Le	Hu	Tr	Ex	mean	Le	Hu	Tr	Ex	mean
RTM	R^2	0.67	0.82	0.89	0.90	0.82	0.68	0.83	0.88	0.90	0.82
	RMSE	0.09	0.09	0.08	0.08	0.09	0.09	0.08	0.08	0.09	0.09
	nRMSE	0.14	0.11	0.09	0.09	0.11	0.14	0.12	0.09	0.10	0.11
MTVI2	R^2	0.68	0.88	0.95	0.97	0.87	0.73	0.88	0.90	0.96	0.87
	RMSE	0.09	0.07	0.05	0.05	0.07	0.08	0.07	0.07	0.05	0.07
	nRMSE	0.13	0.09	0.06	0.05	0.08	0.13	0.10	0.09	0.06	0.10
NN	R^2	0.68	0.73	0.41	0.94	0.69	0.79	0.86	0.83	0.81	0.82
	RMSE	0.09	0.10	0.18	0.07	0.11	0.07	0.07	0.10	0.12	0.09
	nRMSE	0.14	0.13	0.21	0.07	0.14	0.11	0.10	0.11	0.13	0.11
SMA	R^2	-0.01	0.52	0.52	0.82	0.46	-0.03	0.53	0.53	0.83	0.47
	RMSE	0.16	0.14	0.16	0.11	0.14	0.16	0.14	0.16	0.11	0.14
	nRMSE	0.24	0.18	0.19	0.12	0.18	0.25	0.19	0.19	0.12	0.19

Figure 3.10 shows the global NN predictions across all folds for the mixture-specific (top row) and across-mixture models (bottom row), evaluated for each mixture individually. Consistent with the previous findings, Express was the easiest mixture for the NN models to predict. For both mixture-specific and across-mixture models, the predictions clustered tightly around the 1:1 line. Only very low fractional cover values (< 0.2) were strongly overestimated. These points originate exclusively from test fold 8, which con-

tains data from the 2025-09-03 treatment 4 strip instance. As shown in the fractional cover distribution of all strip instances (Figure 3.5), this is the only strip instance with such low fractional cover values.

For Humus, Lepha and Trias, the mixture-specific NNs showed poorer performance and multiple distinct clusters. These clusters with weak predictions were produced by several folds, particularly for fractional cover values below 0.5, where models exhibited little predictive ability. In contrast, these mixtures benefitted from across-mixture training. The across-mixture models yielded substantially lower prediction errors for the problematic folds. Predicted vs. observed plots based on LOSIO-CV for all retrieval methods are shown in Appendix Figures E.1 and E.2. Detailed fold-specific prediction plots for all mixtures are provided in Appendix Figures E.3-E.5 for reference.

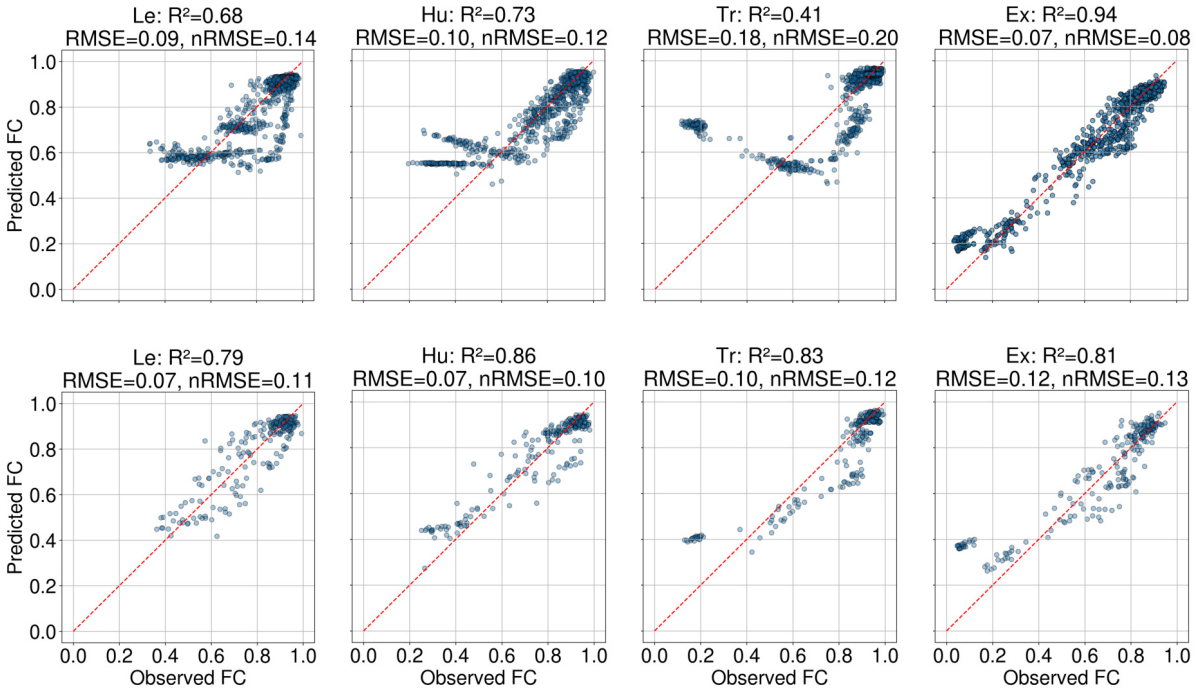

Figure 3.10: Predicted versus observed fractional cover for the neural network models, shown as global predictions across all test folds. **Top row:** Mixture-specific models, evaluated on the corresponding mixtures Lepha (Le), Humus (Hu), Trias (Tr) and Express (Ex). **Bottom row:** Across-mixture models, evaluated on the corresponding mixtures. Each point represents a test sample from one of the cross-validation folds.

4 Discussion

4.1 Dataset characteristics and experimental context

4.1.1 Hyperspectral UAV data

The hyperspectral UAV data provided a reliable basis for biomass and fractional cover analysis. Its high spatial (4 cm) and spectral resolution captured the heterogeneity of cover crop canopies, supporting both baseline and cross-validated modelling. Overall data quality was high, though some limitations should be considered when interpreting results.

Geometric accuracy was generally good, but the initial georeferencing showed spatial offsets along flight lines due to a malfunctioning IMU. Although additional georeferencing using GCPs substantially improved the spatial accuracy of the final hyperspectral mosaic, small residual errors cannot be ruled out. Radiometric quality was generally reliable. Reflectance spectra showed realistic magnitudes and characteristic shapes for the respective surface types. Potential residual effects related to spectral artifacts were minimized by excluding affected wavelength regions during preprocessing (Section 2.3.1). Although UAV flights were conducted under defined acquisition constraints to limit radiometric variability, some variability between acquisitions remained. The comparison of reference panel reflectance showed consistently higher reflectance values for the acquisitions on 2025-07-17. The observed pattern was most pronounced for the white and light grey reference panels, while it was negligible for the dark grey and black panels. This behaviour is consistent with increased diffuse irradiance under the partly cloudy conditions (Arroyo-Mora et al., 2021). Despite the observed radiometric offset for this specific date, the data was still included into the analysis as these conditions reflect realistic acquisition conditions.

A key limitation of the dataset was the under-representation of low fractional cover conditions. Rapid canopy closure of the cover crop mixtures, combined with weather-related constraints on flight scheduling, reduced the number of observations at early growth stages. This affected model performance, especially for LOSIO-CV, as discussed further in Section 4.3.4. Despite this, the dataset captured a wide range of phenological stages and within-mixture variability, supporting robust analysis of biomass and fractional cover retrieval approaches.

4.1.2 Fractional cover reference data

Fractional cover reference data provided a reliable basis for model development and evaluation. The mosaics were spatially accurate, and geometric distortions were minimal, supporting reliable fractional cover measurements. The data were spatially well-aligned with the hyperspectral mosaics, and the use of 1 m^2 observation units reduced potential uncertainties due to minor misalignment, wind-induced plant movement, and the temporal offset of one day between hyperspectral and RGB UAV flights.
Segmentation of vegetation and soil visually achieved high accuracy for green vegetation. However, it was not possible to quantify the segmentation accuracy for the reference data used in this study. Some images showed saturation in the brightest areas, which introduced minor uncertainties in distinguishing vegetation from soil. Further, image quality was not sufficient to reliably distinguish brown vegetation from bare soil. A more sophisticated segmentation approach would be helpful in this regard. Consequently, the reference data were limited to green vegetation. While this restricts the ability to estimate total vegetation cover, including senescent material, it provides consistent and reliable measurements of green fractional cover.

4.1.3 Biomass reference data

Biomass reference data provided a reliable ground truth for model calibration and validation. The sampled above-ground fresh and dry biomass covered a wide range of values, from approximately 0.1 to 5 kg/m² for fresh weight and from about 0.01 to 1 kg/m² for dry weight. These ranges reflect the different growth stages and species compositions of the cover crop mixtures, supporting the development of robust models across diverse canopy structures and phenologies. Maximum dry biomass values were generally comparable to those reported in previous remote sensing studies on cover crop mixtures. Goffart et al. (2021), Holzhauser et al. (2022) and Salehin et al. (2025) reported slightly lower maximum dry biomass values, generally not exceeding 0.5 kg/m². Whereas Poudel et al. (2025) reported dry biomass ranges similar to this study, with values up to approximately 1 kg/m².

Several sources of uncertainty affect the biomass reference data and should be considered when interpreting the results. The rectangular sampling plots provided a consistent and repeatable protocol, harvesting all biomass rooted within the two-dimensional area. While the sampling captured the three-dimensional structure of the plants within the rectangle, it excluded vegetation extending into the plot from outside. As a result, the measured biomass does not fully represent the canopy volume observed by the hyperspectral sensor. Applying the same sampling approach across all plots reduces systematic inconsistencies, but minor discrepancies between sampled biomass and sensor-observed canopy structure remain.
Scaling total amount of dry biomass from dried subsamples introduced additional uncertainty, as subsamples were not necessarily fully representative of the entire sample in terms of moisture content. Variability in water content across species, growth stages, and plant components could propagate into the final dry biomass estimates, potentially influencing model accuracy. This additional uncertainty may also partly explain the generally lower performance observed for dry biomass retrieval compared to fresh biomass.
The spatial alignment of biomass plots with the hyperspectral data was generally reliable. Rather than relying on absolute coordinates, sampling locations were derived relative to blue markers visible in the imagery. This reduced the influence of potential residual georeferencing errors in the hyperspectral mosaic. However, the spatial definition of the sampling locations is subject to uncertainty, as the placement of the wooden sticks and rulers used to delineate the sampling areas was performed manually in the field. This manual alignment, guided by visual estimation to follow the cover crop strips, introduces a small but unquantifiable spatial offset between the true sampling location and the derived sampling location polygons. Despite this limitation, the applied approach enabled rapid and straightforward marking of sampling locations in the field, which was essential for collecting a sufficiently large number of biomass samples over several sampling campaigns.

4.1.4 Mixture characteristics and sources of spectral variability

To support the interpretation of the results, the following section examines mixture characteristics and sources of spectral variability, with details provided in Appendix Table A.1. The investigated cover crop mixtures differed substantially in species composition, canopy structure and phenological development. This resulted in varying degrees of structural and spectral heterogeneity not only between mixtures but also across data acquisitions within mixtures. Express and Trias consisted of three species each and formed comparatively homogeneous canopies. Express was dominated by broadleaf species with a relatively open but vertically coherent canopy. Trias formed a dense and uniform grass-legume canopy. In contrast, Lepha and Humus exhibited higher species richness and stronger structural complexity. Humus included eleven species comprising legumes, grasses and broadleaf species with distinct growth forms, resulting in pronounced vertical stratification of the canopy. Lepha contained fewer species but exhibited strong structural diversity. The canopy was characterized by a combination of horizontal and vertical growth forms

as well as variations in leaf morphology, including both fine- and broad-leaved species. The dominance of Phacelia introduced large flowering structures during specific phenological stages.

Increased species richness and vertical stratification are associated with larger variability in plant height, leaf orientation and canopy architecture, which increases spectral heterogeneity within and between image acquisitions (Holzhauser et al., 2022). Structural heterogeneity within the canopy also increases the occurrence of shaded areas, particularly at high biomass levels. Shaded areas add complex irradiance components, which affect the resulting reflectance of the canopy. In shaded areas, illumination is dominated by diffuse radiation and multiple scattering from surrounding vegetation and soil. At the spatial scale of the UAV imagery, spatial variations in irradiance caused by shadowing add on the intrinsic anisotropic reflectance of the canopy, and are a major source of increasing spectral variability within and between pixels (Damm et al., 2015). Such effects are more pronounced in structurally complex mixtures such as Lepha and Humus than in more homogeneous mixtures like Trias and Express.

These differences provide a key explanatory basis for the observed variability in biomass and fractional vegetation cover retrieval performance across mixtures. In particular, mixture-specific model performance for both biomass and fractional cover was consistently higher for the structurally more homogeneous mixtures Trias and Express than for the comparatively more heterogeneous mixtures Lepha and Humus.

4.2 Performance of biomass retrieval approaches in mixed cover crops

4.2.1 Overall performance of biomass retrieval approaches

VI- and RTM-based approaches were evaluated for estimating above-ground biomass of mixed cover crops using hyperspectral UAV data, considering both mixture-specific and across-mixture baseline modelling and evaluation strategies. Overall, the results demonstrate that biomass retrieval in mixed cover crops can be achieved reliably from UAV-based spectral observations. Moderate to good accuracies were achieved for both band-limited and full-spectral approaches across structurally and compositionally diverse mixtures. Across all evaluated approaches, nRMSE values typically ranged between 10 % and 20 %, indicating stable absolute prediction accuracy even when explained variance differed substantially between approaches and mixtures.

Across-mixture models generally achieved lower prediction accuracy than mixture-specific models. Among the evaluated approaches, GnyLi achieved the highest across-mixture performance ($R^2 = 0.49$ for dry weight biomass), outperforming both red-edge-based indices and the RTM-based approach. This performance can be attributed to GnyLi's reliance on NIR wavelengths, which are less sensitive to chlorophyll-driven differences between mixtures (Bendig et al., 2015). Performance still decreased for highly heterogeneous mixtures, such as Lepha and Humus, where flowering and shadowing introduced additional spectral variability (as discussed in Section 4.2.2).

Mixture-specific models generally explained more variance than across-mixture models, highlighting the need of tailoring biomass retrieval models to individual cover crop mixtures. Fresh weight biomass was predicted more accurately than dry weight, although prediction errors (nRMSE) were similar for both, indicating that absolute accuracy is comparable. Fresh weight biomass, however, is strongly influenced by plant water status, which varies temporally due to transpiration, water availability in the soil, and time of measurement. Dry weight biomass therefore more directly reflects biomass accumulation within a field

and is more commonly used as a reference variable in the literature (Wei, 2010).

The prediction accuracy obtained for mixture-specific dry weight biomass models for Trias and Express (R^2 = 0.6-0.85 and nRMSE = 11-16 %) are comparable or slightly higher to those reported in previous studies. In contrast, prediction accuracies for Lepha and Humus as well as for across-mixture models are slightly lower than reported values, reflecting the increased complexity of these canopies. For example, Holzhauser et al. (2022) reported an R^2 of 0.53 for SR_{Red}-based (broad-band) biomass estimation of mixed cover crops using UAV data. This value lies within the range of mixture-specific model performances observed in this study, exceeding the explained variance achieved for the more structurally complex mixtures Lepha and Humus, but remaining below the accuracies obtained for the more homogeneous mixtures Trias and Express. Direct comparison of absolute prediction errors is not possible, as nRMSE values were not reported in that study. Similarly, Goffart et al. (2021) reported an R^2 value of 0.66 and substantially higher cross-validation RMSE for mixed cover crop models than for single-species models, highlighting the impact of canopy heterogeneity on biomass retrieval performance.

Higher accuracies reported in some studies can largely be attributed to differences in canopy complexity or model inputs. For instance, Poudel et al. (2025) achieved an R^2 of 0.63 with a nRMSE of 15 % using a NN approach. They combined broad-band VIs with canopy height information, using structural information that was not considered in this study. Using airborne hyperspectral data and a full-spectral approach, Wang et al. (2023) reported good biomass estimates for single-species cereal rye (R^2 = 0.72 and RMSE = 12 %). This is a considerably more homogeneous canopy than the mixed cover crops investigated here. Very high biomass estimation accuracy was achieved by Salehin et al. (2025) using UAV data and band-limited multiple regression (R^2 = 0.93) . However, maximum biomass values reported in that study were limited to 0.4 kg/m². This suggests that part of the reported high performance can be attributed to the limited biomass range.

4.2.2 Comparison of biomass retrieval approaches

VI-based retrieval and saturation effects

VI-based biomass retrieval was strongly affected by index-specific sensitivity and saturation. NDVI showed pronounced saturation at relatively low biomass levels (0.1 - 0.2 kg/m²), limiting its suitability for dense mixed cover crop canopies. In contrast, red-edge-based indices such as $ND_{RedEdge}$ and $SR_{RedEdge}$ exhibited substantially weaker saturation effects and maintained sensitivity across a wider biomass range, leading to improved predictive performance. This is consistent with previous studies reporting improved performance of red-edge indices under high biomass conditions (Goffart et al., 2021).

Across all VI models, increased scatter was observed at high biomass levels, particularly for the structurally complex mixtures Lepha and Humus. This reduced performance arises from multiple factors. First, index saturation limits the sensitivity of commonly used VIs at high biomass levels (Myneni and Williams, 1994). Second, flowering modifies canopy reflectance by reducing chlorophyll absorption in the visible domain and altering scattering behaviour. As described by Fang et al. (2016), these effects disproportionately affect VIs combining visible and NIR bands, particularly NDVI and to a lesser extent red-edge-based indices. Third, shadowing introduces additional spectral variability within the canopy, as reflected in wavelength-dependent changes in VI values (Damm et al., 2015). For the more complex mixtures, mixture-specific VI models were affected more strongly by these factors. Red-edge-based indices, however, showed slightly better performance for these complex mixtures and more consistent behaviour across all mixtures compared to NDVI and other indices. This suggests that red-edge-based indices are comparatively less sensitive to

effects such as flowering and shadowing, explained in their improved predictive performance under high-biomass conditions.

RTM-based biomass retrieval and canopy homogeneity

RTM-based biomass retrieval achieved the highest accuracies for mixture-specific models in structurally homogeneous canopies. For Trias and Express, RTM-derived LAI showed a strong relationship with both fresh and dry biomass, resulting in low nRMSE values and high explained variance. These results support the theoretical advantage of the PROSAIL RTM when canopy structure approximates the model assumptions of a homogeneous, turbid medium (Jacquemoud et al., 2009).

RTM performance decreased substantially for the structurally complex mixtures Lepha and Humus. High observed biomass values were frequently associated with moderate LAI values, leading to an underestimation of these biomass values in prediction. This decoupling coincided with dates of pronounced flowering and vertical stratification within the canopies. Thus, non-leaf biomass components contributed substantially to total biomass but were not explicitly represented in the RTM framework. Furthermore, PROSAIL assumes a homogeneously illuminated canopy (Jacquemoud et al., 2009). In Lepha and Humus, the pronounced vertical layering and dense canopy structure increased shading, introducing additional spectral variability that further limits biomass estimation. Similar decoupling between LAI and biomass has been reported by Schiefer et al. (2021), who highlighted the sensitivity of RTM-based LAI retrieval to phenological stage and the importance of explicit representation of non-leaf elements in RTM-based approaches. The results of this study suggest that LAI alone is not sufficient to capture total above-ground biomass in structurally complex canopies. Additionally, the RTM-based approach was constrained by the intermediate retrieval of LAI. The NN used for inversion was trained exclusively on synthetically generated PROSAIL reflectance data and achieved high accuracy on the synthetic test set. However, its performance may degrade when applied to real canopy reflectance, particularly for conditions not well represented in the simulated training data as described by Danner et al. (2021).

4.2.3 RTM- vs. VI-based biomass retrieval (RQ1)

This section addresses RQ1 by comparing the accuracy of RTM- and VI-based approaches for estimating above-ground biomass in mixed cover crops. RTM-based approaches predicted biomass accurately for mixture-specific models of structurally homogeneous canopies (Trias and Express), achieving R^2 values up to 0.85 for dry weight biomass with nRMSE values between 11-12 %. For structurally complex mixtures (Lepha and Humus), RTM performance decreased substantially ($R^2 < 0.25$ for dry weight biomass), likely due to violations of model assumptions, including canopy homogeneity and the presence of non-leaf elements such as flowers. Consequently, RTM approaches also performed less well in the across-mixture evaluation. In comparison, red-edge-based VI approaches showed the most consistent performance across all mixture-specific models, with R^2 values ranging from 0.43 to 0.72 for dry weight biomass. This can partly be explained by their reduced saturation at higher biomass levels compared to other VIs. In the across-mixture evaluation, prediction accuracy declined for all approaches. However, GnyLi outperformed both RTM- and red-edge-based approaches ($R^2 = 0.49$, nRMSE = 16 % for dry weight biomass), likely due to its reduced sensitivity to chlorophyll-driven differences between mixtures.

4.3 Performance of fractional cover retrieval approaches in mixed cover crops

4.3.1 Overall performance of fractional cover retrieval approaches

SMA-, RTM-, VI-, and NN-based approaches were evaluated for estimating fractional vegetation cover of mixed cover crops, using baseline and a LOSIO-CV modelling and evaluation schemes. Overall, fractional cover was retrieved with particularly high performance for VI- and RTM-based approaches for all individual mixtures with R^2 values above 0.74 and nRMSE below 12 %. Baseline across-mixture models also achieved high performance for these approaches. This indicates that, despite differences in species composition between the mixtures, the general relationship between spectrum and green fractional cover remains stable across mixtures. Compared to the literature, these results align well with previous studies. For instance, Prabhakara et al. (2015) reported R^2 values up to 0.87 between broad-band NDVI and fractional cover for single-species cover crops, and Meyer et al. (2017) found only marginal improvements using full-spectral information versus band-limited data within a machine learning framework. This suggests that the high accuracy achieved here is consistent with expectations, and that full spectral information of hyperspectral data is not essential for accurate fractional cover estimation in green canopies.

However, limitations remain. SMA performance was strongly mixture-dependent. Good performance was achieved for structurally simple canopies (Express), while only moderate performance was observed for Humus and Trias, and fractional cover estimation failed entirely for Lepha. This highlights the limitations of SMA for vegetation cover estimation in agricultural systems that have been reported previously. For example, Pacheco et al. (2008) showed that SMA performance strongly depends on crop species and reference data generation. They reported high R^2 values for canola (0.94) and wheat (0.85), but substantially lower performance for bean and corn (R^2 = 0.64 and 0.59). NN-based approaches generally performed well, particularly in the across-mixture setting. However, training variability influenced model robustness for Trias, indicating sensitivity to the representativeness of the training data.

4.3.2 Comparison of fractional cover retrieval approaches

VI-based and RTM-based fractional cover retrieval

VI-based and RTM-based approaches showed very similar performance for fractional cover estimation across all cover crop mixtures in both the baseline and LOSIO-CV evaluation schemes. For the structurally homogeneous mixtures Trias and Express, both approaches achieved excellent prediction accuracies with R^2 values above 0.9 and low nRMSE values. Slightly reduced performance was observed for Lepha and, to a lesser extent, Humus, reflecting their increased structural and phenological complexity. In contrast to biomass retrieval, these reductions were minor and did not substantially compromise model robustness.

Among the evaluated VIs, MTVI2 achieved the highest and most consistent performance for fractional cover estimation for all mixture-specific models. This is in contrast with the biomass retrieval results, where red-edge-based indices performed best. Fractional cover estimation benefited more from indices optimized for vegetation–soil contrast. MTVI2 is specifically designed to minimize soil background effects while maintaining sensitivity to green vegetation (Zou and Mõttus, 2017), which can explain its strong performance under the conditions of this study and in relation to the limitations of the reference data, which are discussed in the next section.

SMA-based retrieval and robustness limitations

SMA showed substantially lower and more variable performance than VI- and RTM-based approaches, particularly for structurally complex mixtures. A key insight was that SMA performance clustered by strip instance rather than mixture type, visible in the across-mixture results (Figure 3.9). This suggests that temporal variability and acquisition conditions influenced unmixing results more strongly than species composition. One likely explanation is endmember selection. Vegetation endmembers were primarily selected from medium to late growing stages, which differ from the spectral and structural characteristics of earlier growing stages, especially in heterogeneous mixtures. In addition, soil endmembers were selected under dry conditions only, while soil moisture varied across acquisition dates, further reducing the representativeness of the endmember set.

Another contributing factor is radiometric inconsistency across acquisition dates. Small but systematic differences in reflectance levels, as indicated by variability in reference panel reflectance across acquisition dates, may not have been fully accounted for during post-processing. In SMA, endmember spectra were linearly combined with fractions summing to one. Because the method relies on the absolute reflectance values of the endmembers, these differences in spectral magnitude can shift pixel spectra relative to the selected endmembers, thereby reducing robustness across strip instances. In contrast, this effect is expected to be less critical for VI- and RTM-based approaches. VIs were largely ratio-based and normalized, which reduces their sensitivity to absolute radiometric offsets. RTM-based retrievals relied on synthetic PROSAIL spectra that covered a wide range of illumination and canopy conditions, making them more robust to radiometric inconsistencies.

Part of the reduced SMA performance is also related to limitations in the reference data. In the RGB-based fractional cover reference, both shaded areas and flowers were classified as background (fraction = 0), although they contribute to the hyperspectral reflectance signal. Shaded areas were also more extensive in the hyperspectral UAV data due to differences in spatial resolution, flight altitude, and acquisition timing. This mismatch between spectral observations and reference data increased uncertainty for all retrieval approaches, but its impact was strongest for SMA. In particular, SMA was insensitive to soil contributions in shaded pixels and frequently assigned vegetation fractions close to one. An explicit treatment or exclusion of shaded pixels could therefore be a relevant consideration for improving SMA performance in future UAV applications.
Finally, the reliance on linear spectral mixing represents an additional limitation. Volumetric scattering, multiple interactions between canopy elements, and mutual shading violate linear mixing assumptions in dense and heterogeneous canopies (Schweiger et al., 2015). This further constrained SMA performance, especially under variable illumination and structural conditions.

4.3.3 SMA-based vs. VI- and RTM-based fractional cover retrieval (RQ2)

This section addresses RQ2 by comparing the accuracy of SMA-, VI-, and RTM-based approaches for estimating fractional cover in mixed cover crops using the baseline evaluation scheme. The SMA-based approach was expected to perform best because of its ability to distinguish between non-photosynthetic vegetation and soil. However, this potential advantage could not be assessed, as the reference data classified only green vegetation versus background, without separating non-photosynthetic vegetation.

For mixture-specific models, band-limited VI- and full-spectral RTM-based approaches achieved high accuracy on all mixture-specific models, with R^2 values above 0.74 and nRMSE below 12 %. These approaches also showed high predictive ability in the across-mixture evaluation scheme, with R^2 values above 0.88

and nRMSE below 8 %. Among the VIs, MTVI2 showed particularly strong performance, likely due to its ability to minimize soil background effects. In contrast, SMA performance was highly variable. Good performance was achieved only for the structurally simple mixture Express, moderate performance for Humus and Trias, and predictions failed for Lepha. Performance clustered by strip instance rather than mixture identity, indicating high sensitivity to the applied endmember selection, temporal variability, and acquisition conditions.

4.3.4 NN performance within and across mixtures

NNs trained using LOSIO-CV on mixture-specific data achieved excellent performance for some mixtures, (e.g. Express, $R^2 = 0.94$), while performance for other mixtures ranged from good to moderate. These differences indicate that mixture-specific NNs can be highly effective when the training data sufficiently cover the variability present in the target mixture. However, their performance is sensitive to representativeness of the training data, and predictions can degrade when the test data include conditions or fractional cover values not well represented in training. This is a common limitation of machine learning models for out-of-distribution predictions (Sun et al., 2024), as seen for Trias.

Across-mixture NN models unexpectedly outperformed the mixture-specific models. This is likely due to the fact that, as shown in the baseline results for fractional cover retrieval, mixture composition had only a minor effect on the relationship between spectra and green fractional cover. Consequently, models performed well even in the across-mixture setting. For the LOSIO-CV-trained NNs, pooling data across mixtures increased the coverage of the training dataset, providing a more continuous and representative range of fractional cover values for each fold. The improved performance of across-mixture NN models in comparison to the mixture-specific NN models therefore reflects the benefits of a larger and more diverse training set, which provided a wider and more continuous coverage of fractional cover values during training. An additional opportunity for across-mixture evaluation would be a leave-one-mixture-out cross-validation, which would test model performance on mixtures entirely unseen during training. This approach could provide a more realistic assessment of true across-mixture generalization and better reflect real-world scenarios for model transfer to new sites or species compositions.

Despite its simplicity, the implemented NN architecture, consisting of three fully connected layers with batch normalization, already achieved strong performance across mixtures. Nevertheless, previous studies have shown that NN performance can be further improved through more sophisticated architectures, hyperparameter selection and enhanced input representation. In particular, incorporating VIs or RTM-derived traits alongside spectral bands improved NN as reported by Kharel et al. (2023) and Wang et al. (2023).

4.3.5 NN-based across-mixture fractional cover retrieval (RQ3)

This section addresses RQ3 by evaluating how precisely across-mixture NN models can predict fractional vegetation cover in comparison to mixture-specific NNs and the alternative SMA-, VI-, and RTM-based approaches. Mixture-specific NN models achieved good to excellent performance for most mixtures ($R^2 > 0.68$, nRMSE < 14 %) and were generally comparable to VI- and RTM-based approaches. However, they did not consistently exceed the performance of these methods. In particular, NN performance deteriorated when the range of fractional cover values in the mixture-specific training data was limited. This was most evident for Trias, where incomplete coverage of the fractional cover range resulted in reduced prediction accuracy, highlighting the sensitivity of mixture-specific NN models to the representativeness of the training data.

In contrast, across-mixture NN models showed consistently good performance for all mixtures ($R^2 > 0.79$, nRMSE < 13 %). Pooling data across mixtures increased the value ranges of the training datasets, resulting in more representative fractional cover distributions within each LOSIO-CV training fold. As a result, across-mixture NNs provided better predictions across mixtures.

Overall, these findings suggest that under data-limited conditions, generic across-mixture NN models can provide more robust fractional cover predictions than mixture-specific NN models. At the same time, the results indicate that tailoring mixture-specific NN models for green fractional cover retrieval is not required, as the spectral–fractional-cover relationship was largely consistent across mixtures. Moreover, given that band-limited VI-based approaches (e.g. MTVI2) already achieved similarly high accuracy, the added complexity of NN-based models may not be necessary for reliable fractional cover estimation in mixed cover crop canopies.

4.4 Methodological considerations and comparability of retrieval approaches

The evaluated retrieval approaches differed substantially in their methodological complexity and in the degree of intermediate modelling involved. VI- and RTM-based approaches relied on an explicit regression modelling step to translate spectral information into fractional cover or biomass, whereas SMA directly estimated fractional cover from spectral mixtures without empirical calibration. The NN-based approach was purely data driven and relationships between spectral information and the target variable were learnt during training. VI- and RTM-based approaches therefore required both spectral sensitivity to the target variable and a well-performing calibration. These approaches can achieve high accuracy under well-controlled conditions as seen in this study, but their transferability may be limited when applied outside the range of conditions covered by the calibration data. From an operational perspective, approaches that do not rely on empirical calibration such as SMA are often considered attractive, because they can be applied across sites, seasons and acquisition conditions (Small, 2004; Li et al., 2023). Further, all approaches were compared at the output level using the same reference data and evaluation schemes, so the results reflect their operational performance under realistic UAV conditions rather than the theoretical potential of each method.

5 Conclusions

This thesis investigated band-limited and full-spectral approaches for retrieving above-ground biomass and fractional vegetation cover in mixed cover crop systems using hyperspectral UAV data. Precise biomass retrieval remains challenging and results showed generally moderate performance across approaches and pronounced sensitivity to mixture complexity. RTM-based methods performed well for structurally simple mixtures but deteriorated with increasing canopy heterogeneity and the presence of non-leaf elements, likely due to stronger violations of underlying model assumptions. In mixture-specific settings, red-edge-based VIs showed the most consistent biomass estimates, exhibiting robust performance across all individual mixtures. In across-mixture scenarios, the GnyLi index achieved the best performance, likely due to its reduced sensitivity to chlorophyll-driven differences between mixtures.

For green fractional vegetation cover, VI- and RTM-based approaches achieved robust results, with MTVI2 emerging as the best-performing method in both mixture-specific and across-mixture evaluations. These findings indicate that full spectral information is not necessarily required for accurate fractional cover estimation in green, mixed canopies. In contrast, SMA showed pronounced dependence on mixture composition and phenological stage, and performed reliably only for the least complex mixture. The pronounced clustering of the results by strip instance suggests a high sensitivity to endmember representativeness across growth stages as well as to radiometric consistency. NNs showed unexpectedly strong performance in across-mixture evaluations, likely benefiting from a broader range of fractional cover values available in the training data and the relatively similar green-spectral relationships across mixtures.

A main limitation of this study lies in the fractional cover reference data, which represented green vegetation only. Flowers and shaded vegetation, however, contributed to the hyperspectral signal and likely causing mismatches between remote sensing observations and ground truth. As a result, the capability of SMA to retrieve non-photosynthetic vegetation could not be fully assessed. Future work should therefore improve reference data generation to explicitly include non-photosynthetic vegetation, enabling a more comprehensive evaluation of retrieval approaches in regard to soil-erosion relevant fractional cover. In addition, shadows were not treated explicitly and likely introduced additional variability in the UAV data, particularly in structurally complex canopies. For operational applications based on satellite data, however, shadow effects are expected to be less pronounced due to spatial aggregation. To improve biomass estimation, future research could explore the use of three-dimensional RTMs to better account for canopy structure.

Overall, this thesis contributes to a better understanding of the potential and limitations for assessing biomass and fractional vegetation cover in mixed cover crop systems. In addition to the methodological evaluation of retrieval approaches, this work involved the implementation and validation of a recommended hyperspectral UAV data processing workflow for a newly deployed sensor system. Iterative adjustments were required to ensure reliable radiometric, geometric and spectral data quality. This highlights the challenges and feasibility of using emerging hyperspectral UAV technology for quantitative vegetation analysis. From an application perspective, this study shows that hyperspectral UAV data can serve as a controlled test environment for evaluating biomass and fractional cover retrieval methods. The insights form a foundation for improving, transferring and evaluating these methods to multispectral and hyperspectral satellite sensors. In the long term, these advances contribute to the development of operational large-scale monitoring systems for cover crop quality and associated ecosystem services.

References

Adetunji, A. T., Ncube, B., Mulidzi, R., and Lewu, F. B. (2020). Management impact and benefit of cover crops on soil quality: A review. *Soil and Tillage Research*, 204:104717.

Applanix (2021). *POSPac MMS GNSS-Inertial Tools User Guide*. Applanix Corportation, Richmodn Hill, Canada. Version 8.7.

Arroyo-Mora, J. P., Kalacska, M., Løke, T., Schläpfer, D., Coops, N. C., Lucanus, O., and Leblanc, G. (2021). Assessing the impact of illumination on UAV pushbroom hyperspectral imagery collected under various cloud cover conditions. *Remote Sensing of Environment*, 258:112396.

Asam, S., Klein, D., and Dech, S. (2015). Estimation of grassland use intensities based on high spatial resolution LAI time series. *The International Archives of the Photogrammetry, Remote Sensing and Spatial Information Sciences*, XL-7/W3:285–291.

Bashagaluke, J. B., Logah, V., Opoku, A., Sarkodie-Addo, J., and Quansah, C. (2018). Soil nutrient loss through erosion: Impact of different cropping systems and soil amendments in Ghana. *PLOS ONE*, 13(12):1–17.

Bendig, J., Yu, K., Aasen, H., Bolten, A., Bennertz, S., Broscheit, J., Gnyp, M. L., and Bareth, G. (2015). Combining UAV-based plant height from crop surface models, visible, and near infrared vegetation indices for biomass monitoring in barley. *International Journal of Applied Earth Observation and Geoinformation*, 39:79–87.

Bendini, H. d. N., Fieuzal, R., Carrere, P., Clenet, H., Galvani, A., Allies, A., and Ceschia, E. (2024). Estimating winter cover crop biomass in France using optical Sentinel-2 dense image time series and machine learning. *Remote Sensing*, 16(5).

Berger, K., Atzberger, C., Danner, M., D'Urso, G., Mauser, W., Vuolo, F., and Hank, T. (2018). Evaluation of the PROSAIL model capabilities for future hyperspectral model environments: A review study. *Remote Sensing*, 10(1).

Boos, T. (2025). Using high-resolution satellite data to estimate canopy cover in plot experiments. Master's thesis, Universität Zürich.

Broge, N. and Leblanc, E. (2001). Comparing prediction power and stability of broadband and hyperspectral vegetation indices for estimation of green Leaf Area Index and canopy chlorophyll density. *Remote Sensing of Environment*, 76(2):156–172.

Büchi, L., Valsangiacomo, A., Burel, E., and Charles, R. (2016). Integrating simulation data from a crop model in the development of an agri-environmental indicator for soil cover in Switzerland. *European Journal of Agronomy*, 76:149–159.

Calvão, T. and Palmeirim, J. (2004). Mapping Mediterranean scrub with satellite imagery: Biomass estimation and spectral behaviour. *International Journal of Remote Sensing*, 25:3113–3126.

Damm, A., Guanter, L., Verhoef, W., Schläpfer, D., Garbari, S., and Schaepman, M. E. (2015). Impact of varying irradiance on vegetation indices and chlorophyll fluorescence derived from spectroscopy data. *Remote Sensing of Environment*, 156:202–215.

Danner, M., Berger, K., Wocher, M., Mauser, W., and Hank, T. (2021). Efficient RTM-based training of machine learning regression algorithms to quantify biophysical & biochemical traits of agricultural crops. *ISPRS Journal of Photogrammetry and Remote Sensing*, 173:278–296.

Daryanto, S., Fu, B., Wang, L., Jacinthe, P. A., and Zhao, W. (2018). Quantitative synthesis on the ecosystem services of cover crops. *Earth-Science Reviews*, 185:357–373.

Delegido, J., Verrelst, J., Rivera, J. P., Ruiz-Verdú, A., and Moreno, J. (2015). Brown and green LAI mapping through spectral indices. *International Journal of Applied Earth Observation and Geoinformation*, 35:350–358.

DJI (2022). DJI Mavic 3E / 3T. https://enterprise.dji.com/mavic-3-enterprise. Accessed: 2025-11-10.

Du Plessis, W. (1999). Linear regression relationships between NDVI, vegetation and rainfall in Etosha National Park, Namibia. *Journal of Arid Environments*, 42:235–260.

Fang, S., Tang, W., Peng, Y., Gong, Y., Dai, C., Chai, R., and Liu, K. (2016). Remote estimation of vegetation fraction and flower fraction in oilseed rape with unmanned aerial vehicle data. *Remote Sensing*, 8(5).

Finney, D. M., White, C. M., and Kaye, J. P. (2016). Biomass production and carbon/nitrogen ratio influence ecosystem services from cover crop mixtures. *Agronomy Journal*, 108(1):39–52.

Flynn, E., Dougherty, C., and Wendroth, O. (2008). Assessment of pasture biomass with the Normalized Difference Vegetation Index from active ground-based sensors. *Agronomy Journal*, 100:114–121.

Freeman, K., Girma, K., Arnall, B., Mullen, R., Martin, K., Teal, R., and Raun, W. (2007). By-plant prediction of corn forage biomass and nitrogen uptake at various growth stages using remote sensing and plant height. *Agronomy Journal*, 99:530–536.

Gitelson, A. A. and Merzlyak, M. N. (1996). Signature analysis of leaf reflectance spectra: Algorithm development for remote sensing of chlorophyll. *Journal of Plant Physiology*, 148(3):494–500.

Gnyp, M. L., Bareth, G., Li, F., Lenz-Wiedemann, V. I., Koppe, W., Miao, Y., Hennig, S. D., Jia, L., Laudien, R., Chen, X., and Zhang, F. (2014). Development and implementation of a multiscale biomass model using hyperspectral vegetation indices for winter wheat in the North China Plain. *International Journal of Applied Earth Observation and Geoinformation*, 33(1):232–242.

Goffart, D., Curnel, Y., Planchon, V., Goffart, J. P., and Defourny, P. (2021). Field-scale assessment of Belgian winter cover crops biomass based on Sentinel-2 data. *European Journal of Agronomy*, 126:126278.

Gomez-Dans, J. (2019). ProSAIL Python Bindings. https://github.com/jgomezdans/prosail. [Source code]. [GitHub]. Accessed: 2025-08-12.

Haboudane, D., Miller, J. R., Pattey, E., Zarco-Tejada, P. J., and Strachan, I. B. (2004). Hyperspectral vegetation indices and novel algorithms for predicting green LAI of crop canopies: Modeling and validation in the context of precision agriculture. *Remote Sensing of Environment*, 90(3):337–352.

He, L., Li, A., Yin, G., Nan, X., and Bian, J. (2019). Retrieval of grassland aboveground biomass through inversion of the PROSAIL model with MODIS imagery. *Remote Sensing*, 11(13):1597.

Hively, W. D., Lang, M., McCarty, G. W., Keppler, J., Sadeghi, A., and McConnell, L. L. (2009). Using satellite remote sensing to estimate winter cover crop nutrient uptake efficiency. *Journal of Soil and Water Conservation*, 64(5):303–313.

Holzhauser, K., Räbiger, T., Rose, T., Kage, H., and Kühling, I. (2022). Estimation of biomass and N uptake in different winter cover crops from UAV-based multispectral canopy reflectance data. *Remote Sensing*, 14(18):4525.

Huang, S., Tang, L., Hupy, J. P., Wang, Y., and Shao, G. (2021). A commentary review on the use of Normalized Difference Vegetation Index (NDVI) in the era of popular remote sensing.

Im, J. and Jensen, J. R. (2008). Hyperspectral remote sensing of vegetation. *Geography Compass*, 2(6):1943–1961.

Jacquemoud, S., Verhoef, W., Baret, F., Bacour, C., Zarco-Tejada, P. J., Asner, G. P., François, C., and Ustin, S. L. (2009). PROSPECT + SAIL models: A review of use for vegetation characterization. *Remote Sensing of Environment*, 113(Supplement 1):S56–S66.

Jordan, C. F. (1969). Derivation of Leaf-Area Index from quality of light on the forest floor. *Ecology*, 50:663–666.

Kharel, T. P., Bhandari, A. B., Mubvumba, P., Tyler, H. L., Fletcher, R. S., and Reddy, K. N. (2023). Mixed-species cover crop biomass estimation using Planet imagery. *Sensors*, 23(3):1541.

Kooistra, L., Berger, K., Brede, B., Graf, L. V., Aasen, H., Roujean, J. L., Machwitz, M., Schlerf, M., Atzberger, C., Prikaziuk, E., Ganeva, D., Tomelleri, E., Croft, H., Reyes Muñoz, P., Garcia Millan, V., Darvishzadeh, R., Koren, G., Herrmann, I., Rozenstein, O., Belda, S., Rautiainen, M., Rune Karlsen, S., Figueira Silva, C., Cerasoli, S., Pierre, J., Tanlr Kaylkçl, E., Halabuk, A., Tunc Gormus, E., Fluit, F., Cai, Z., Kycko, M., Udelhoven, T., and Verrelst, J. (2024). Reviews and syntheses: Remotely sensed optical time series for monitoring vegetation productivity. *Biogeosciences*, 21(2):473–511.

Kumar, L. and Mutanga, O. (2017). Remote sensing of above-ground biomass.

Lamb, B. T., Dean Hively, W., Jennewein, J., Thieme, A., Soroka, A. M., Santos, L., Jones, D., and Mirsky, S. (2025). Multiyear crop residue cover mapping using narrow-band vs. broad-band shortwave infrared satellite imagery. *Soil and Tillage Research*, 251:106524.

Ledain, Sélène (2025). ProSAIL forward. https://github.com/EOA-team/ProSAIL_forward. [Source code]. [GitHub]. Accessed: 2025-08-12.

Li, L., Mu, X., Jiang, H., Chianucci, F., Hu, R., Song, W., Qi, J., Liu, S., Zhou, J., Chen, L., Huang, H., and Yan, G. (2023). Review of ground and aerial methods for vegetation cover fraction (fCover) and related quantities estimation: Definitions, advances, challenges, and future perspectives. *ISPRS Journal of Photogrammetry and Remote Sensing*, 199:133–156.

Linnenbrink, J., Milà, C., Ludwig, M., and Meyer, H. (2024). KNNDM CV: K-fold nearest-neighbour distance matching cross-validation for map accuracy estimation. *Geoscientific Model Development*, 17(15):5897–5912.

Lobert, F., Schwieder, M., Alsleben, J., Broeg, T., Kowalski, K., Okujeni, A., Hostert, P., and Erasmi, S. (2025). Unveiling year-round cropland cover by soil-specific spectral unmixing of Landsat and Sentinel-2 time series. *Remote Sensing of Environment*, 318:114594.

Meyer, H., Lehnert, L. W., Wang, Y., Reudenbach, C., Nauss, T., and Bendix, J. (2017). From local spectral measurements to maps of vegetation cover and biomass on the Qinghai-Tibet-Plateau: Do we need hyperspectral information? *International Journal of Applied Earth Observation and Geoinformation*, 55:21–31.

Muñoz, J. D., Finley, A. O., Gehl, R., and Kravchenko Sasha, S. (2010). Nonlinear hierarchical models for predicting cover crop biomass using Normalized Difference Vegetation Index. *Remote Sensing of Environment*, 114(12):2833–2840.

Myneni, R. and Williams, D. (1994). On the relationship between FAPAR and NDVI. *Remote Sensing of Environment*, 49(3):200–211.

Nguy-Robertson, A. L. (2013). The mathematical identity of two vegetation indices: MCARI2 and MTVI2. *International Journal of Remote Sensing*, 34(21):7504–7507.

Norsk Elektro Optikk (2025). HySpex Mjolnir VS-620. https://www.hyspex.com/hyspex-products/hyspex-mjolnir/mjolnir-vs-620. Accessed: 2025-11-10.

OpenDroneMap ODM (2020). A command line toolkit to generate maps, point clouds, 3D models and DEMs from drone, balloon or kite images. https://github.com/OpenDroneMap/ODM. Version 2.8.0. [Source code]. [GitHub]. Accessed: 2025-11-10.

Pacheco, A., Bannari, A., Staenz, K., and McNairn, H. (2008). Deriving percent crop cover over agriculture canopies using hyperspectral remote sensing. *Canadian Journal of Remote Sensing*, 34:S110–S123.

Papadopoulos, A. A., Moonea, S. J., and Bird, N. R. A. (2006). Quantification of the effects of contrasting crops in the development of soil structure: An organic conversion. *Soil Use and Management*, 22(2):172–179.

Paszke, A., Gross, S., Massa, F., Lerer, A., Bradbury, J., Chanan, G., Killeen, T., Lin, Z., Gimelshein, N., Antiga, L., Desmaison, A., Köpf, A., Yang, E., DeVito, Z., Raison, M., Tejani, A., Chilamkurthy, S., Steiner, B., Fang, L., Bai, J., and Chintala, S. (2019). *PyTorch: An imperative style, high-performance deep learning library*. Curran Associates Inc., Red Hook, NY, USA.

Pereira, L. S., Paredes, P., Melton, F., Johnson, L., Wang, T., López-Urrea, R., Cancela, J. J., and Allen, R. G. (2020). Prediction of crop coefficients from fraction of ground cover and height. Background and validation using ground and remote sensing data. *Agricultural Water Management*, 241:106197.

Poudel, A., Burns, D., Adhikari, R., Duron, D., Hendrix, J., Gentimis, T., Tubana, B., and Setiyono, T. (2025). Cover crop biomass predictions with unmanned aerial vehicle remote sensing and TensorFlow machine learning. *Drones*, 9(2):131.

Prabhakara, K., Hively, W. D., and McCarty, G. W. (2015). Evaluating the relationship between biomass, percent groundcover and remote sensing indices across six winter cover crop fields in Maryland, United States. *International Journal of Applied Earth Observation and Geoinformation*, 39:88–102.

Punalekar, S. M., Verhoef, A., Quaife, T. L., Humphries, D., Bermingham, L., and Reynolds, C. K. (2018). Application of Sentinel-2A data for pasture biomass monitoring using a physically based radiative transfer model. *Remote Sensing of Environment*, 218:207–220.

Richter, K., Atzberger, C., Vuolo, F., and D'Urso, G. (2011). Evaluation of Sentinel-2 spectral sampling for radiative transfer model based LAI estimation of wheat, sugar beet, and maize. *IEEE Journal of Selected Topics in Applied Earth Observations and Remote Sensing*, 4(2):458–464.

Rouse, J., Haas, W., H, S. R., and Deering, J. A. (1973). Monitoring vegetation systems in the great plains with ERTS (Earth Resources Technology Satellite). *Third ERTS Symposium, Washington, DC (NASA)*, pages 309–317.

Salehin, S. M. U., Poudyal, C., Rajan, N., and Bagavathiannan, M. (2025). Cover crop types influence biomass estimation using unmanned aerial vehicle-mounted multispectral sensors. *Remote Sensing*, 17:1471.

Schiefer, F., Schmidtlein, S., and Kattenborn, T. (2021). The retrieval of plant functional traits from canopy spectra through RTM-inversions and statistical models are both critically affected by plant phenology. *Ecological Indicators*, 121:107062.

Schläpfer, D. and Popp, C. (2025). *DROACOR User Manual*. ReSe Applications LLC, Wil, Switzerland. Version 2.1.

Schweiger, A. K., Risch, A. C., Damm, A., Kneubühler, M., Haller, R., Schaepman, M. E., and Schütz, M. (2015). Using imaging spectroscopy to predict above-ground plant biomass in alpine grasslands grazed by large ungulates. *Journal of Vegetation Science*, 26(26):175–190.

Schweizerischer Bundesrat (2013). Verordnung über die Direktzahlungen an die Landwirtschaft. https://www.fedlex.admin.ch/eli/cc/2013/765/de#tit_1/chap_2/sec_2. Accessed: 2025-11-10.

Sims, D. A. and Gamon, J. A. (2002). Relationships between leaf pigment content and spectral reflectance across a wide range of species, leaf structures and developmental stages. *Remote Sensing of Environment*, 81(2):337–354.

Small, C. (2004). The Landsat ETM+ spectral mixing space. *Remote Sensing of Environment*, 93(1):1–17.

Sun, K., Hu, Y., Labhanpal, G., and Zhou, R. Z. (2024). Spatial cross-validation for GeoAI. In Gao, S., Hu, Y., and Li, W., editors, *Handbook of Geospatial Artificial Intelligence*, pages 201–213. CRC Press, Boca Raton.

Swisstopo (2025). AGNES station ETH2. https://pnac.swisstopo.admin.ch/pages/en/eth2.html. Accessed: 2025-11-10.

Tucker, C. J. (1979). Red and photographic infrared linear combinations for monitoring vegetation. *Remote Sensing of Environment*, 8(2):127–150.

Vincent-Caboud, L., Peigné, J., Casagrande, M., and Silva, E. M. (2017). Overview of organic cover crop-based no-tillage technique in Europe: Farmers' practices and research challenges. *Agriculture*, 7(5).

Virtanen, P., Gommers, R., Oliphant, T. E., Haberland, M., Reddy, T., Cournapeau, D., Burovski, E., Peterson, P., Weckesser, W., Bright, J., van der Walt, S. J., Brett, M., Wilson, J., Millman, K. J., Mayorov, N., Nelson, A. R. J., Jones, E., Kern, R., Larson, E., Carey, C. J., Polat, İ., Feng, Y., Moore, E. W., VanderPlas, J., Laxalde, D., Perktold, J., Cimrman, R., Henriksen, I., Quintero, E. A., Harris, C. R., Archibald, A. M., Ribeiro, A. H., Pedregosa, F., van Mulbregt, P., and SciPy 1.0 Contributors (2020). SciPy 1.0: Fundamental Algorithms for Scientific Computing in Python. *Nature Methods*, 17:261–272.

Wang, S., Guan, K., Zhang, C., Jiang, C., Zhou, Q., Li, K., Qin, Z., Ainsworth, E. A., He, J., Wu, J., Schaefer, D., Gentry, L. E., Margenot, A. J., and Herzberger, L. (2023). Airborne hyperspectral imaging of cover crops through radiative transfer process-guided machine learning. *Remote Sensing of Environment*, 285:113386.

Wei, X. (2010). Biomass estimation: A remote sensing approach. *Geography Compass*, 4(11):1635–1647.

Xu, B., Yang, X., Tao, W., Qin, Z., Liu, H., Miao, J., and Bi, Y. (2008). MODIS-based remote sensing monitoring of grass production in China. *International Journal of Remote Sensing*, 29:5313–5327.

Yue, J. and Tian, Q. (2020). Estimating fractional cover of crop, crop residue, and soil in cropland using broadband remote sensing data and machine learning. *International Journal of Applied Earth Observation and Geoinformation*, 89:102089.

Zou, X. and Mõttus, M. (2017). Sensitivity of common vegetation indices to the canopy structure of field crops. *Remote Sensing*, 9(10).

A Appendix: Data and Methods

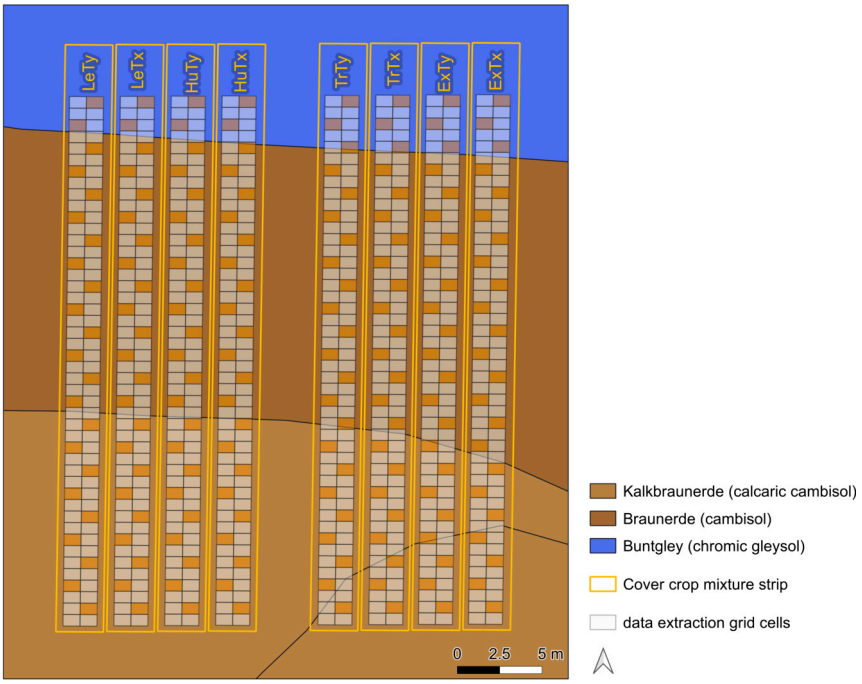

Figure A.1: Three soil types within the cover crop mixture strips: Calcaric cambisol, cambisol and chromic gleysol. Displayed are the cover crop mixture strips and the data extraction grid cells. Soil type data: Agroscope.

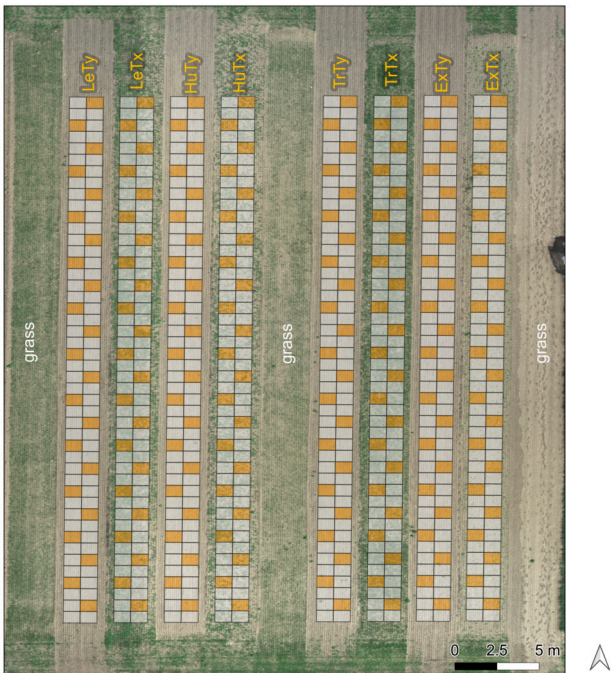

Figure A.2: Fractional cover grid cells as region of interests: Grid cells of size 1 x 1 m for every cover crop strip. Orange cells: Data points for balanced across-mixture models in LOSIO-CV (leave-one-strip-instance-out cross-valildation). Note that grid cells do no appear square due to the map projection (WGS 84).

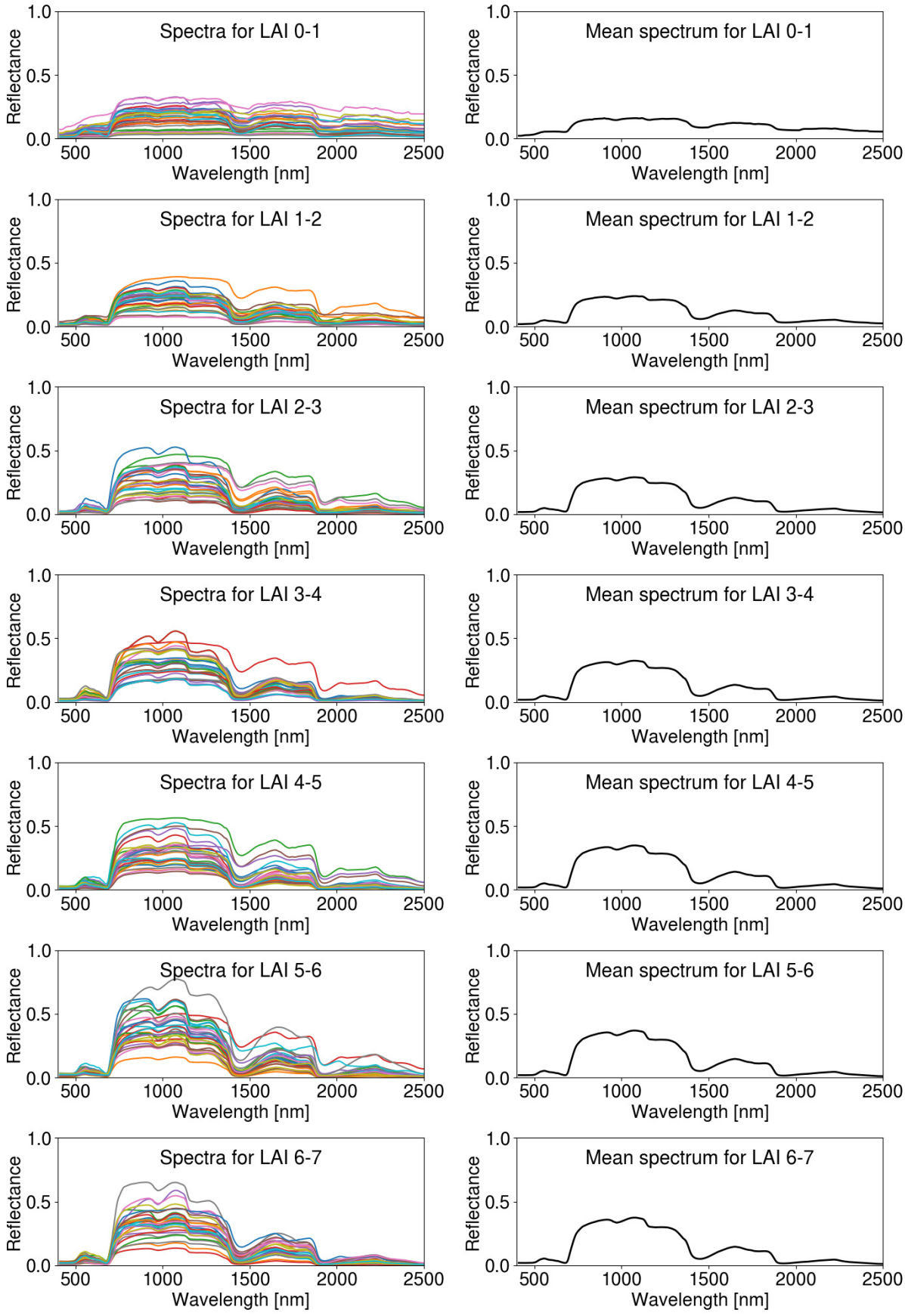

Figure A.3: With PROSAIL simulated reflectances for different Leaf Area Index values (LAI) under defined parameter ranges. **Left:** Subset of example spectra within defined LAI ranges. **Right:** Mean spectrum of all simulated reflectances for the defined LAI range.

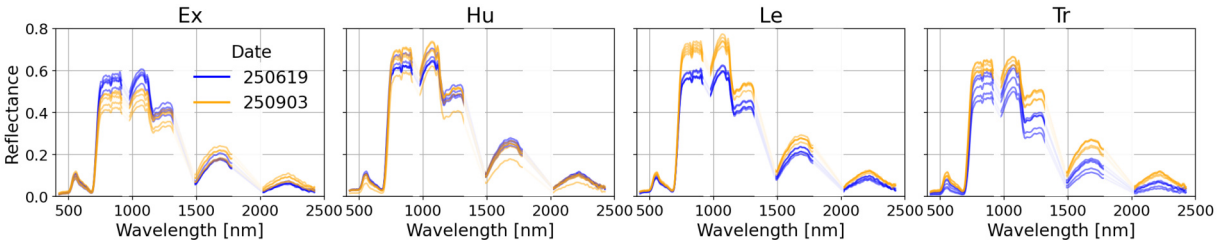

Figure A.4: Green vegetation endmembers for each cover crop mixture, extracted from the datasets from 2025-06-19 and 2025-09-03. Mixtures: Express (Ex), Humus (Hu), Lepha (Le), Trias (Tr).

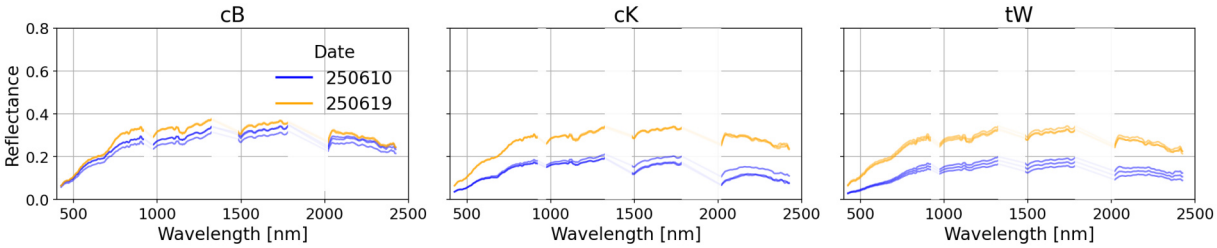

Figure A.5: Soil endmembers for each soil type, extracted from the datasets from 2025-06-10 and 2025-06-19. Soil types: calcaric cambisol (cK), cambisol (cB), chromic gleysol (tW).

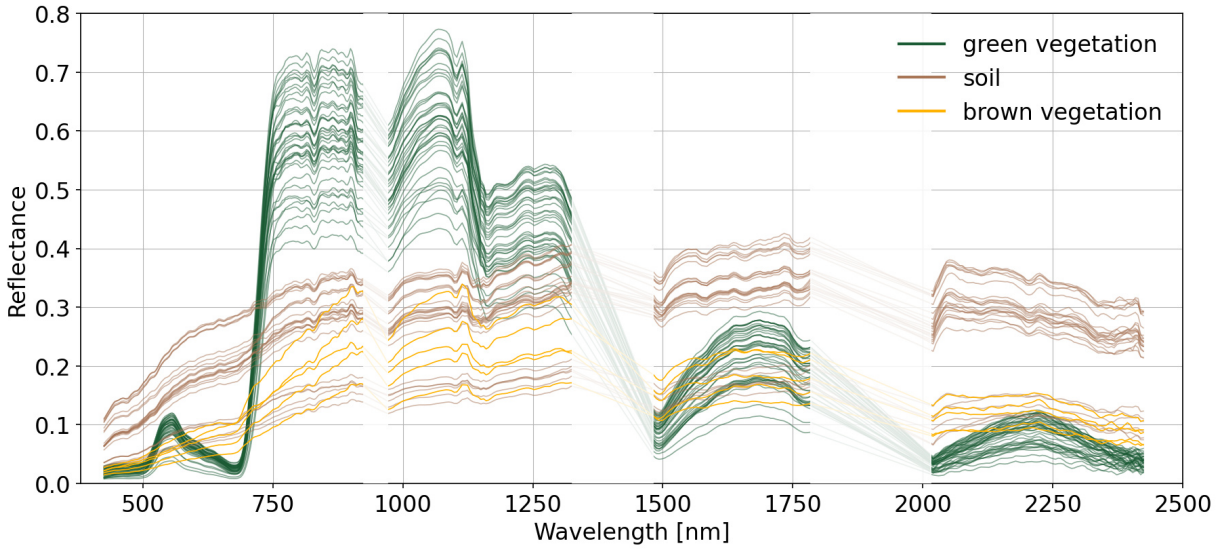

Figure A.6: Selected soil, green and brown vegetation endmembers for spectral unmixing.

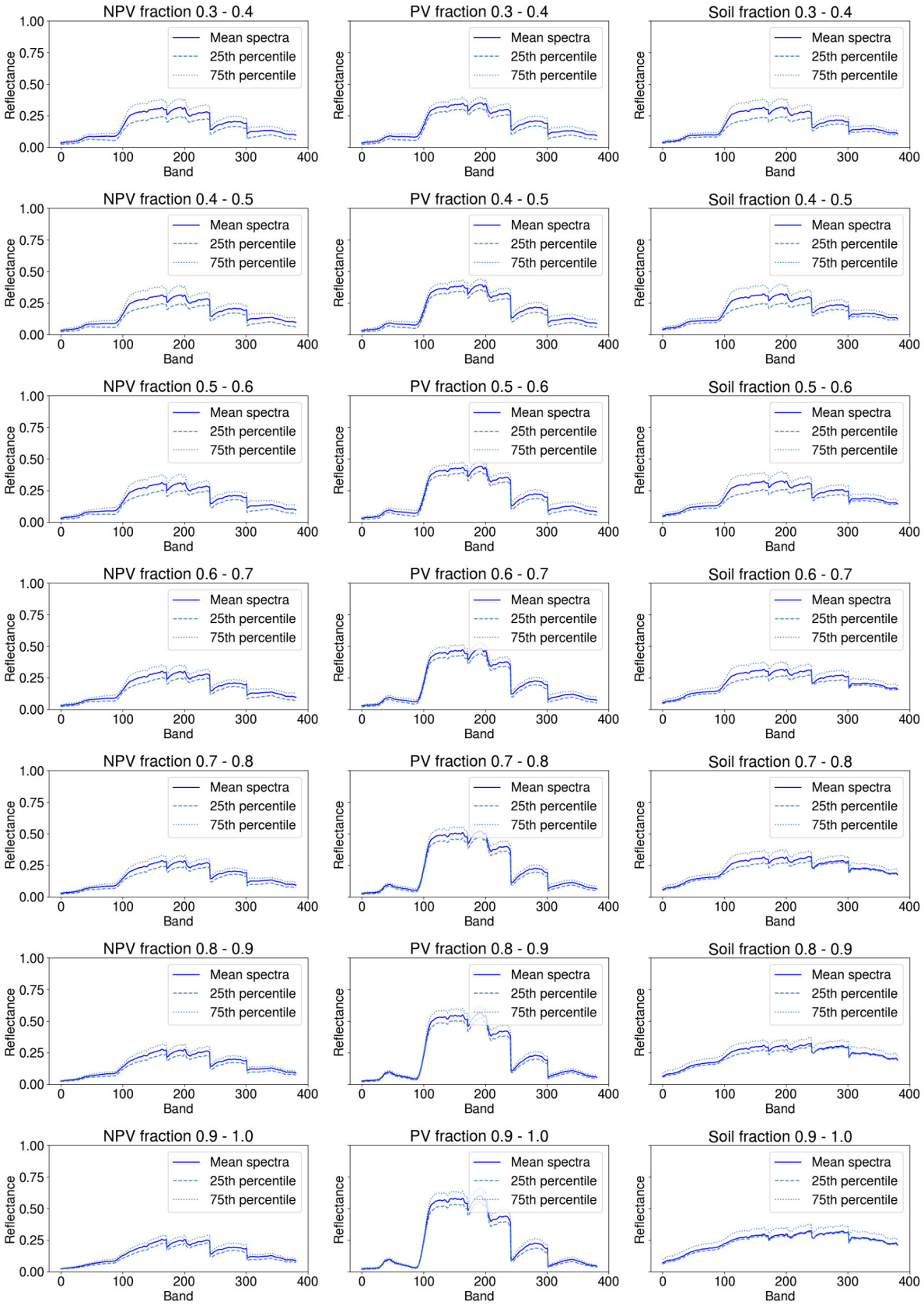

Figure A.7: Synthetic spectra for each fraction above 0.3 using the selected endmembers and a shade component. NPV: Non-photosynthetic vegetation, PV: Photosynthetic-vegetation.

Table A.1: Examples of RGB (unmanned aerial vehicle) images acquired with a Mavic 3E for each cover crop mixture and acquisition date.

Strip instance	Lepha	Humus	Trias	Express
2025-06-10 T1				
2025-06-10 T2				
2025-06-19 T1	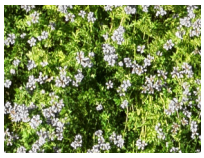	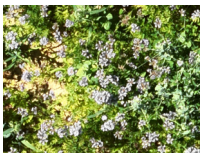		
2025-06-19 T2	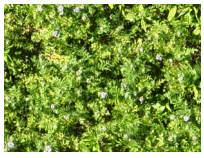			
2025-07-17 T2				
2025-08-07 T3	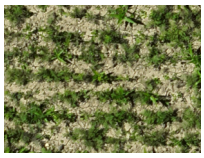	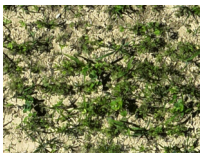	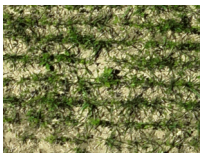	
2025-08-13 T3				
2025-09-03 T3				
2025-09-03 T4			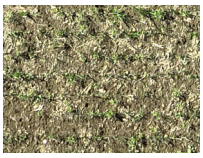	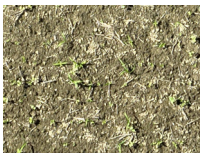
2025-09-18 T3				
2025-09-18 T4				

B Appendix: Results biomass (fresh weight)

Table B.1: Performance metrics of vegetation index-based fresh weight biomass models for the mixture-specific and across-mixture models. Metrics include R2, RMSE (kg/m2), nRMSE (%) and the regression function used (linear or power).

		Across-mixture	Mixture-specific				
Approach	Metric		Le	Hu	Tr	Ex	Mean
GnyLi	R2	0.60	0.64	0.53	0.82	0.66	0.66
	RMSE	0.74	0.82	0.85	0.34	0.43	0.61
	nRMSE	0.15	0.16	0.20	0.13	0.15	0.16
	fit	pow	pow	pow	pow	lin	-
MTVI2	R2	0.38	0.19	0.32	0.71	0.78	0.50
	RMSE	0.92	1.23	1.02	0.43	0.34	0.76
	nRMSE	0.18	0.25	0.24	0.16	0.12	0.19
	fit	lin	pow	lin	pow	pow	-
NDVI	R2	0.37	0.29	0.29	0.83	0.82	0.56
	RMSE	0.92	1.15	1.05	0.33	0.31	0.71
	nRMSE	0.18	0.23	0.25	0.12	0.11	0.18
	fit	pow	pow	pow	pow	pow	-
$ND_{RedEdge}$	R2	0.43	0.75	0.66	0.79	0.62	0.71
	RMSE	0.88	0.68	0.72	0.36	0.45	0.55
	nRMSE	0.17	0.14	0.17	0.14	0.15	0.15
	fit	lin	lin	lin	pow	lin	-
$SR_{RedEdge}$	R2	0.41	0.75	0.67	0.80	0.61	0.71
	RMSE	0.89	0.69	0.72	0.36	0.46	0.56
	nRMSE	0.18	0.14	0.17	0.13	0.16	0.15
	fit	lin	lin	lin	lin	lin	-
SR_{Red}	R2	0.41	0.37	0.31	0.87	0.83	0.59
	RMSE	0.89	1.09	1.03	0.29	0.30	0.68
	nRMSE	0.18	0.22	0.24	0.11	0.10	0.17
	fit	pow	pow	pow	pow	pow	-
TVI	R2	0.37	0.13	0.35	0.59	0.71	0.44
	RMSE	0.92	1.28	1.00	0.51	0.40	0.80
	nRMSE	0.18	0.26	0.24	0.19	0.14	0.21
	fit	lin	pow	lin	lin	pow	-

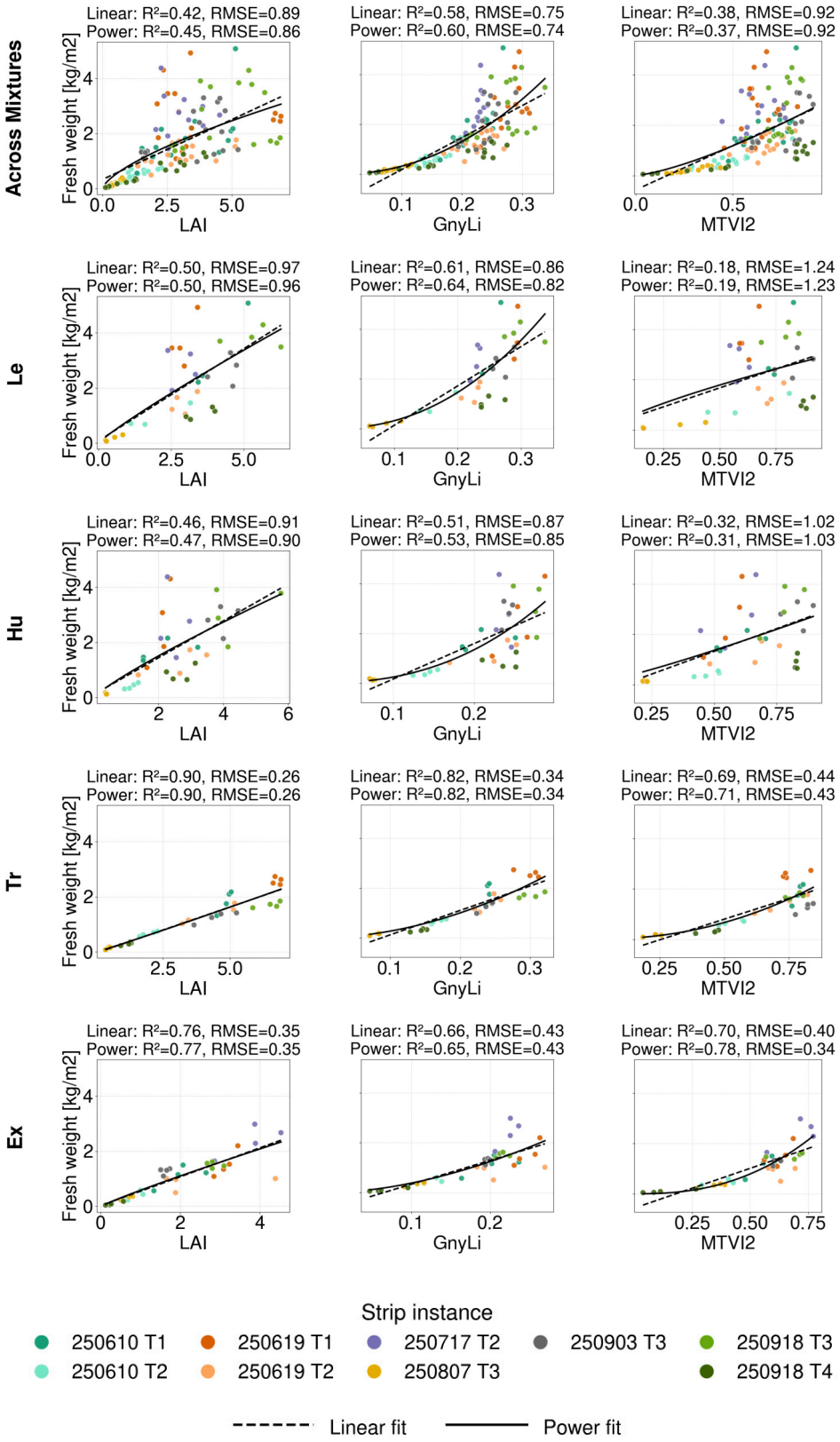

Figure B.1: Scatterplots of fresh weight biomass versus retrieved trait from radiative transfer model based and vegetation indices based approaches (part 1). **Left:** Radiative transfer model derived Leaf Area Index (LAI), **middle:** GnyLi, **right:** MTVI. Displayed from top to bottom are across-mixture models and the four mixture-specific models (Le: Lepha, Hu: Humus, Tr: Trias, Ex: Express). Performance of the linear regression vs. power function is evaluated with R^2, RMSE and nRMSE.

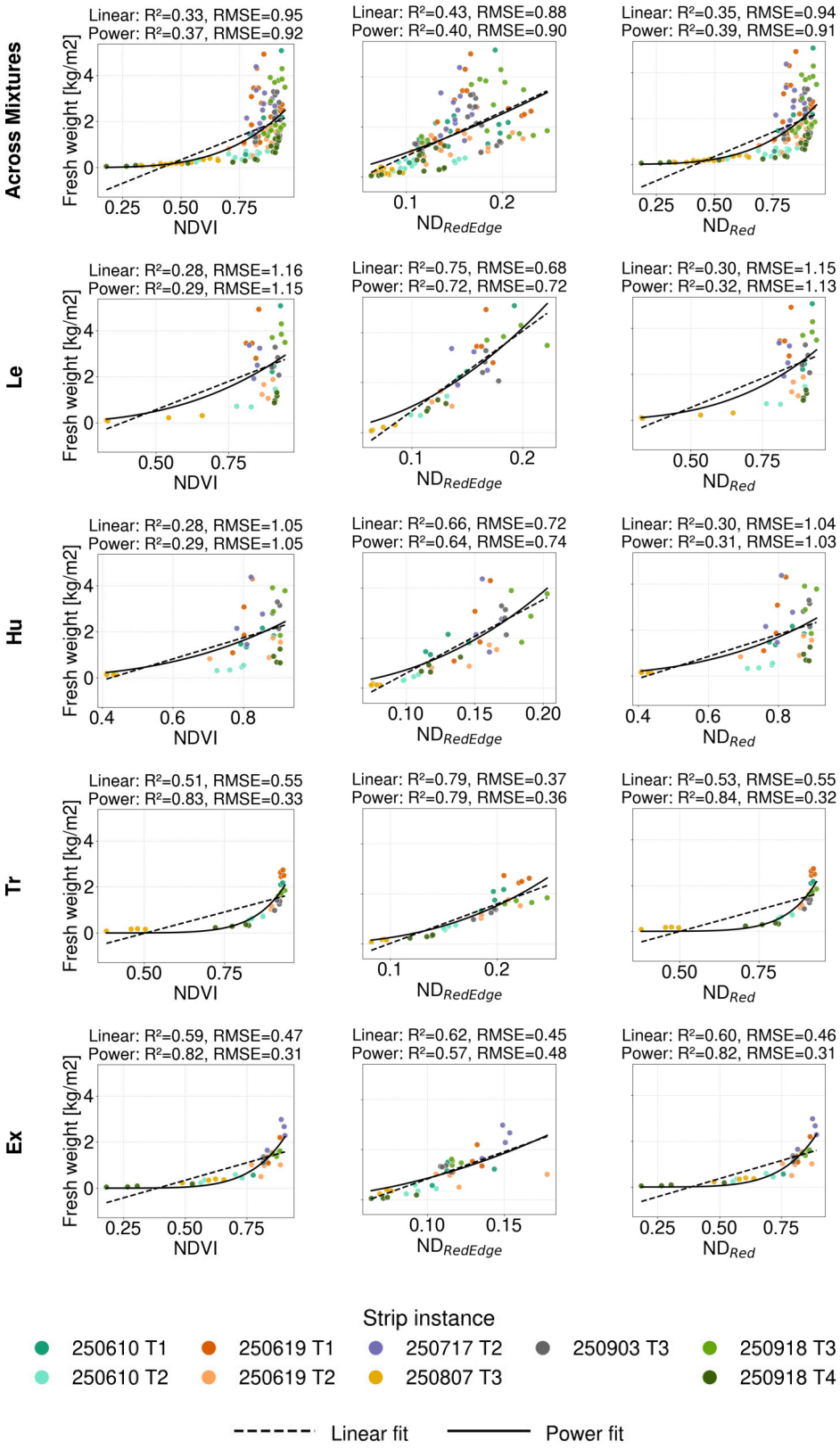

Figure B.2: Scatterplots of fresh weight biomass versus retrieved trait from radiative transfer model based and vegetation indices based approaches (part 2). **Left:** NDVI, **middle:** $ND_{RedEdge}$, **right:** ND_{Red}. Displayed from top to bottom are across-mixture models and the four mixture-specific models (Le: Lepha, Hu: Humus, Tr: Trias, Ex: Express). Performance of the linear regression vs. power function is evaluated with R^2, RMSE and nRMSE.

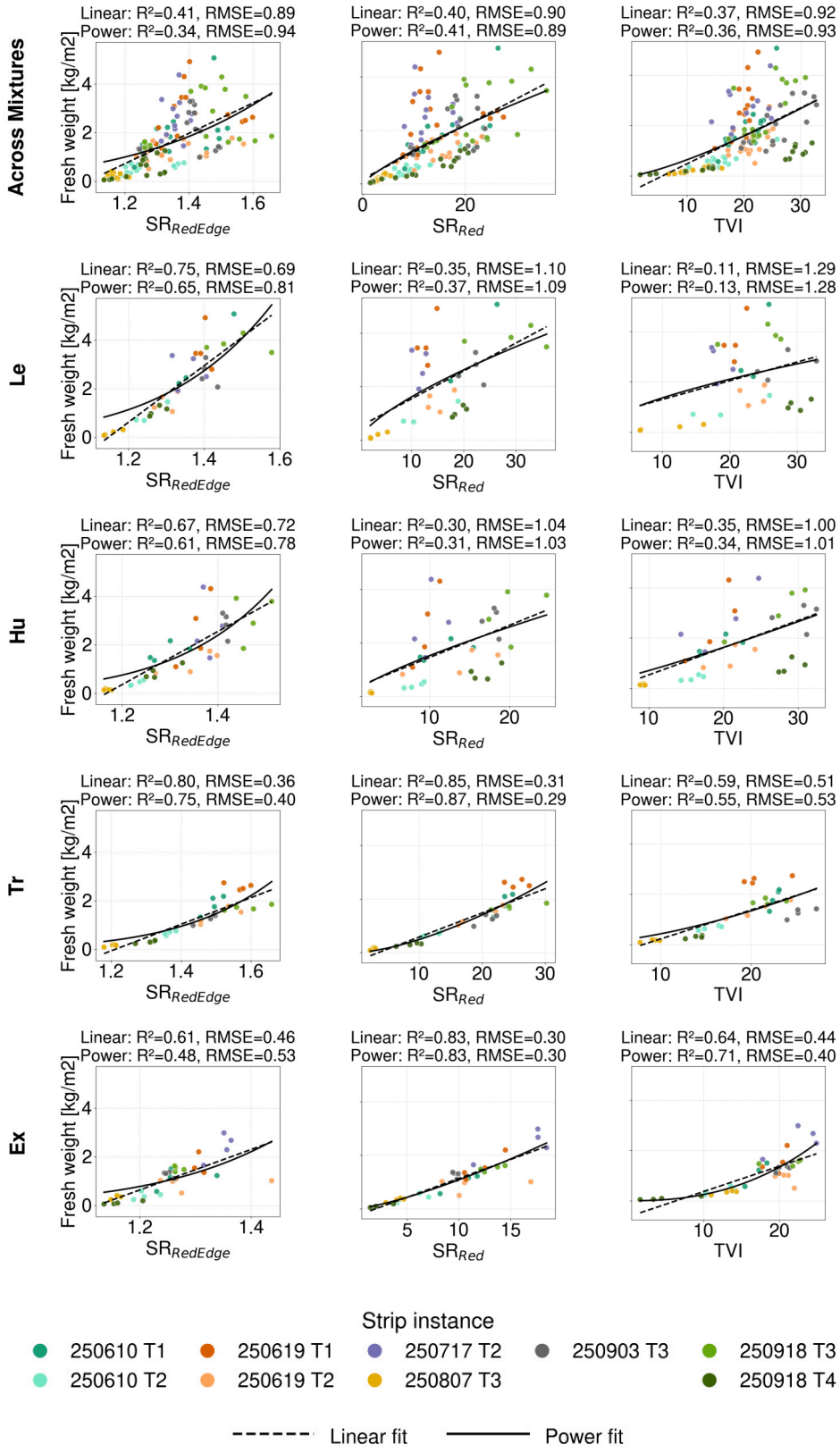

Figure B.3: Scatterplots of fresh weight biomass versus retrieved trait from radiative transfer model based and vegetation indices based approaches (part 3). **Left:** $SR_{RedEdge}$, **middle:** SR_{Red}, **right:** TVI. Displayed from top to bottom are across-mixture models and the four mixture-specific models (Le: Lepha, Hu: Humus, Tr: Trias, Ex: Express). Performance of the linear regression vs. power function is evaluated with R^2, RMSE and nRMSE.

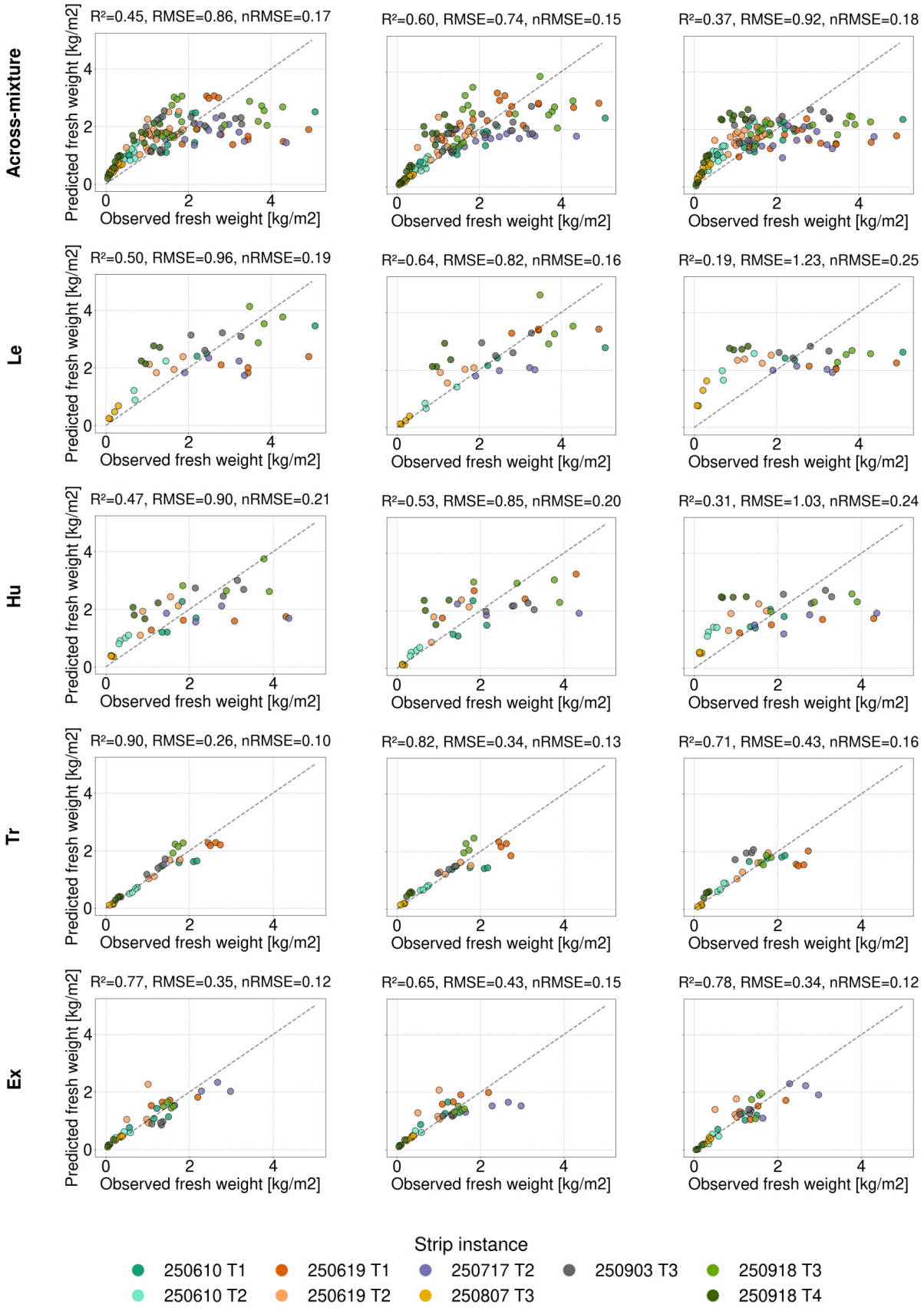

Figure B.4: Predicted versus observed scatter plots for fresh weight biomass across-mixture and mixture-specific models (part 1). **Left:** Radiative transfer model, **middle:** GnyLi, **right:** Modified Triangular Vegetation Index 2. Displayed from top to bottom are across-mixture models and the four mixture-specific models (Le: Lepha, Hu: Humus, Tr: Trias, Ex: Express).

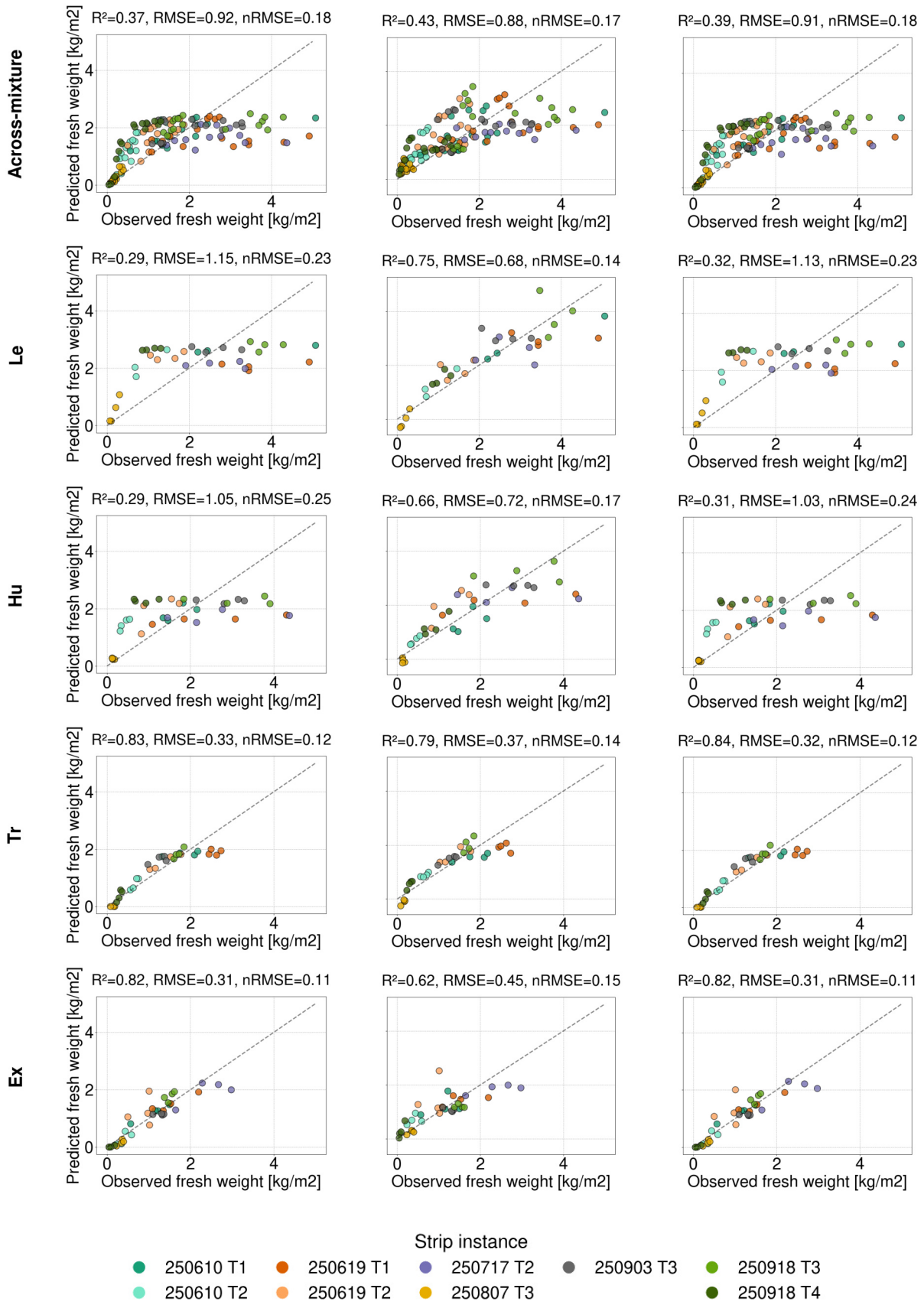

Figure B.5: Predicted versus observed scatter plots for fresh weight biomass across-mixture and mixture-specific models (part 2). **Left:** Normalized Difference Vegetation Index, **middle:** Normalized Difference red edge, **right:** Normalized Difference red. Displayed from top to bottom are across-mixture models and the four mixture-specific models (Le: Lepha, Hu: Humus, Tr: Trias, Ex: Express).

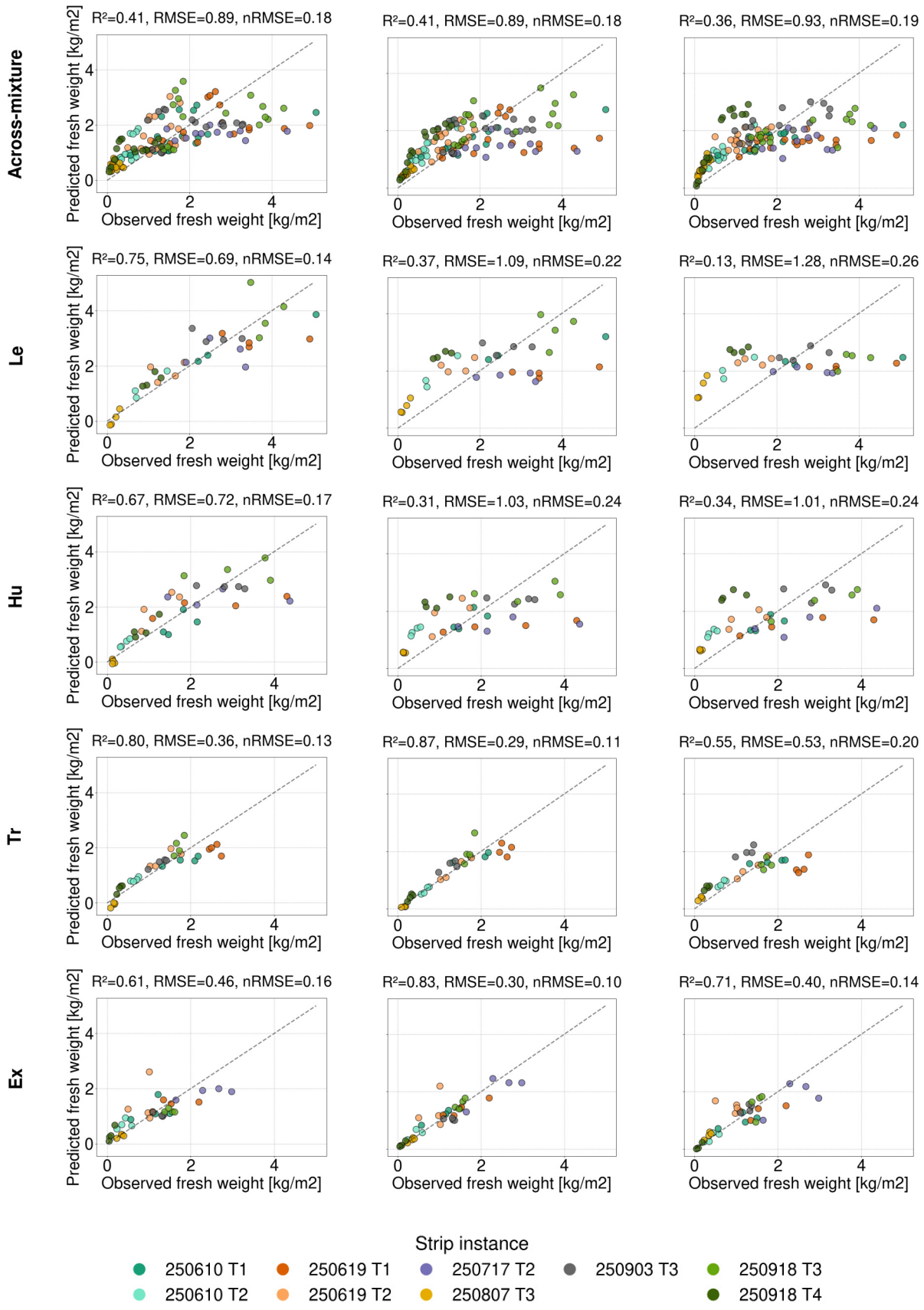

Figure B.6: Predicted versus observed scatter plots for fresh weight biomass across-mixture and mixture-specific models (part 3). **Left:** Simple Ratio red edge, **middle:** Simple ratio red, **right:** Triangular Vegetation Index. Displayed from top to bottom are across-mixture models and the four mixture-specific models (Le: Lepha, Hu: Humus, Tr: Trias, Ex: Express).

C Appendix: Results biomass (dry weight)

Table C.1: Performance metrics of VI-based dry weight biomass models for the mixture-specific and across-mixture models. Metrics include R2, RMSE (kg/m2), nRMSE (%) and the regression function used (linear or power).

		Across-mixture	Mixture-specific				
Approach	Metric		Le	Hu	Tr	Ex	Mean
GnyLi	R2	0.49	0.36	0.42	0.79	0.60	0.54
	RMSE	0.15	0.19	0.17	0.07	0.08	0.13
	nRMSE	0.16	0.21	0.19	0.13	0.16	0.17
	fit	pow	pow	pow	pow	lin	-
MTVI2	R2	0.22	0.05	0.14	0.55	0.72	0.36
	RMSE	0.18	0.24	0.21	0.11	0.07	0.16
	nRMSE	0.19	0.26	0.23	0.19	0.13	0.20
	fit	lin	pow	pow	pow	pow	-
NDVI	R2	0.25	0.12	0.16	0.70	0.77	0.44
	RMSE	0.18	0.23	0.21	0.09	0.06	0.15
	nRMSE	0.19	0.25	0.23	0.15	0.12	0.19
	fit	pow	lin	lin	pow	pow	-
$ND_{RedEdge}$	R2	0.38	0.45	0.49	0.72	0.64	0.57
	RMSE	0.16	0.18	0.16	0.09	0.08	0.13
	nRMSE	0.17	0.20	0.18	0.15	0.15	0.17
	fit	lin	lin	lin	pow	lin	-
$SR_{RedEdge}$	R2	0.36	0.43	0.49	0.71	0.63	0.56
	RMSE	0.16	0.18	0.16	0.09	0.08	0.13
	nRMSE	0.17	0.20	0.18	0.15	0.15	0.17
	fit	lin	lin	lin	lin	lin	-
SR_{Red}	R2	0.24	0.09	0.12	0.75	0.81	0.44
	RMSE	0.18	0.23	0.21	0.08	0.06	0.15
	nRMSE	0.19	0.25	0.23	0.14	0.11	0.18
	fit	pow	pow	pow	pow	pow	-
TVI	R2	0.20	0.02	0.15	0.44	0.65	0.32
	RMSE	0.18	0.24	0.21	0.12	0.08	0.16
	nRMSE	0.20	0.26	0.23	0.21	0.15	0.21
	fit	lin	pow	pow	lin	pow	-

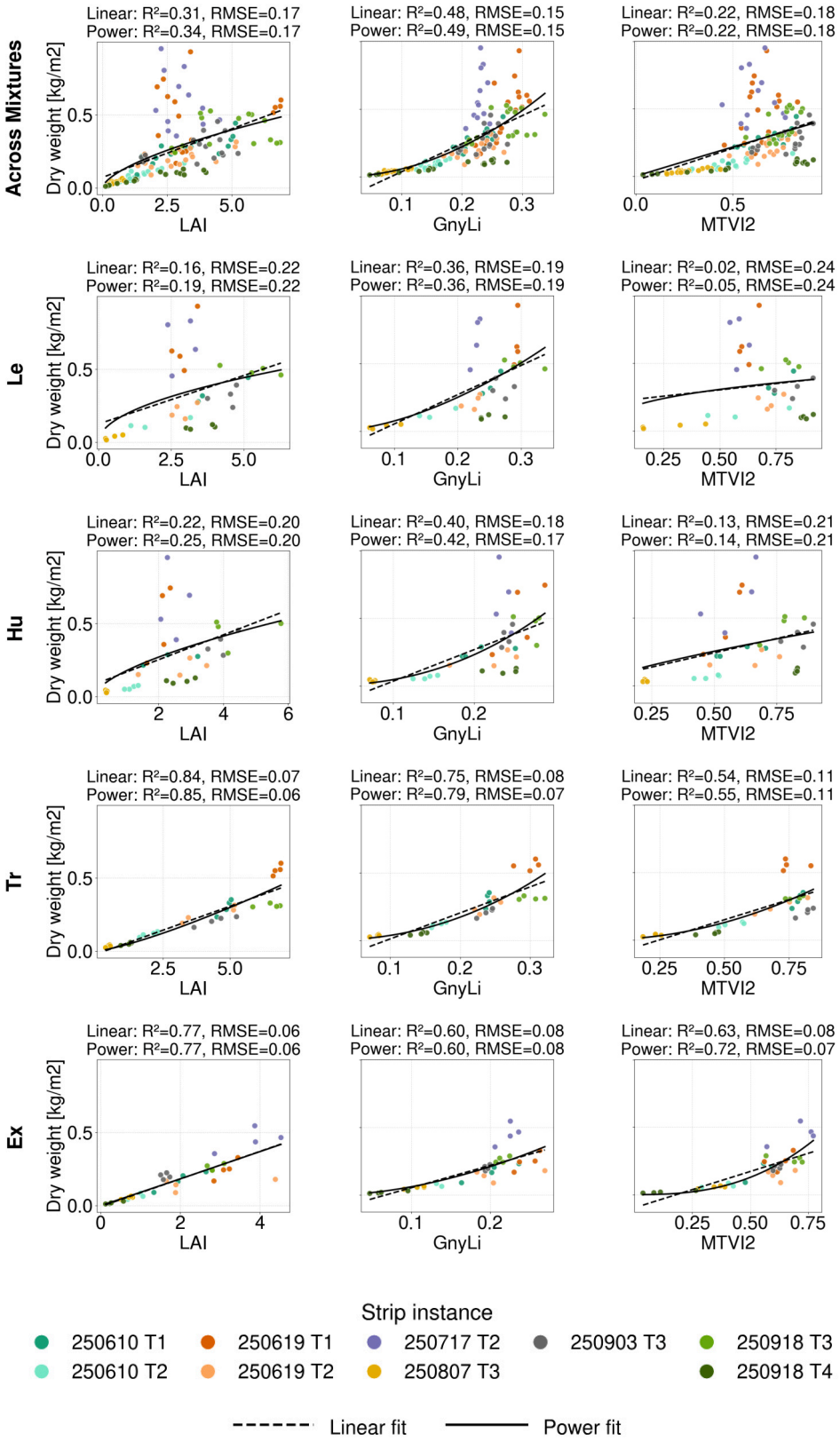

Figure C.1: Scatterplots of dry weight biomass versus retrieved trait from radiative transfer model based and vegetation indices based approaches (part 1). Left: Radiative transfer model derived Leaf Area Index (LAI), **middle:** GnyLi, **right:** Modified Triangular Vegetation Index 2 (MTVI2). Displayed from top to bottom are across-mixture models and the four mixture-specific models (Le: Lepha, Hu: Humus, Tr: Trias, Ex: Express). Performance of the linear regression vs. power function is evaluated with R^2, RMSE and nRMSE.

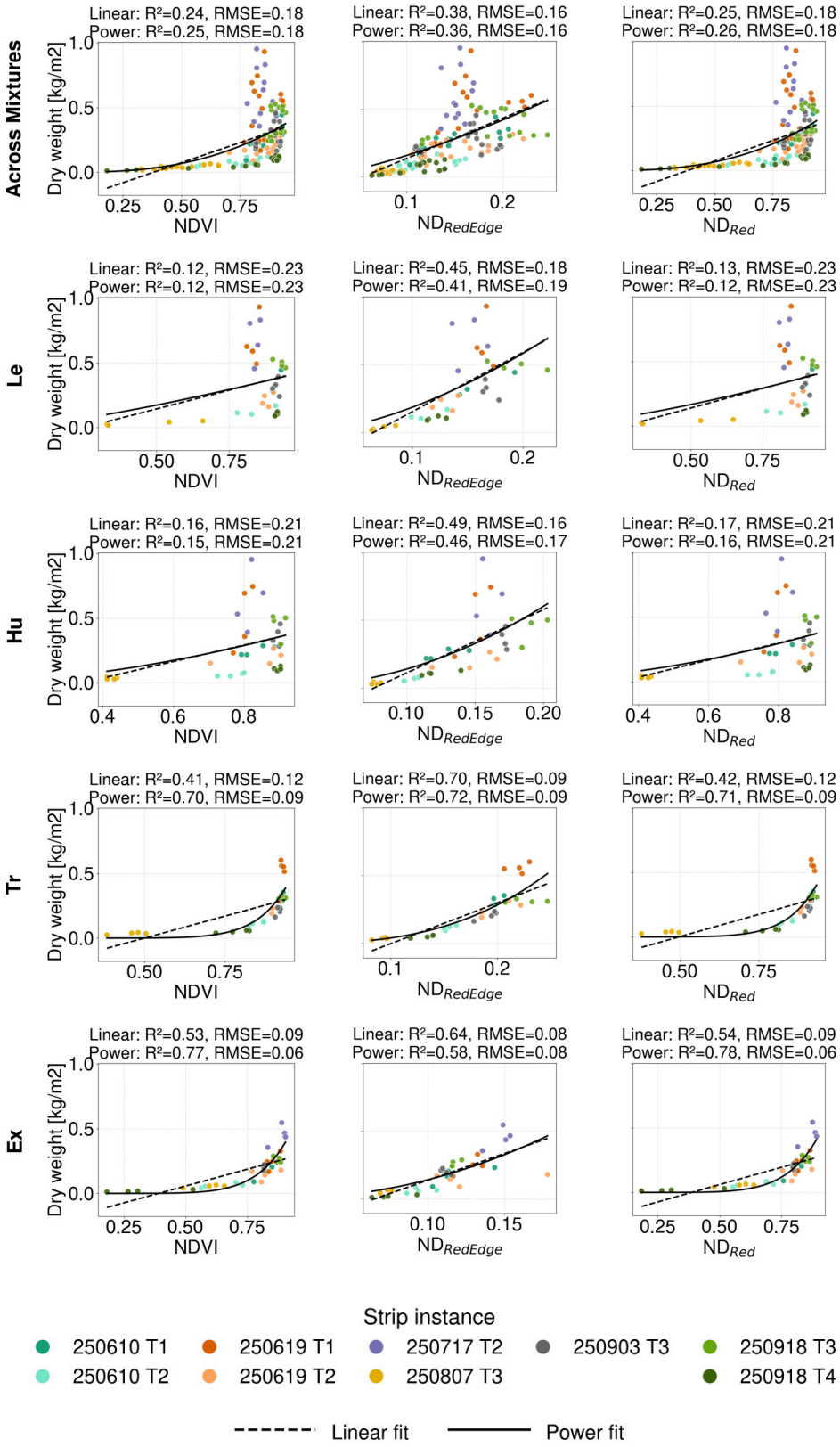

Figure C.2: Scatterplots of dry weight biomass versus retrieved trait from radiative transfer model based and vegetation indices based approaches (part 2). **Left:** Normalized Difference Vegetation Index (NDVI), **middle:** Normalized Difference red edge ($ND_{RedEdge}$), **right:** ND_{Red}. Displayed from top to bottom are across-mixture models and the four mixture-specific models (Le: Lepha, Hu: Humus, Tr: Trias, Ex: Express). Performance of the linear regression vs. power function is evaluated with R^2, RMSE and nRMSE.

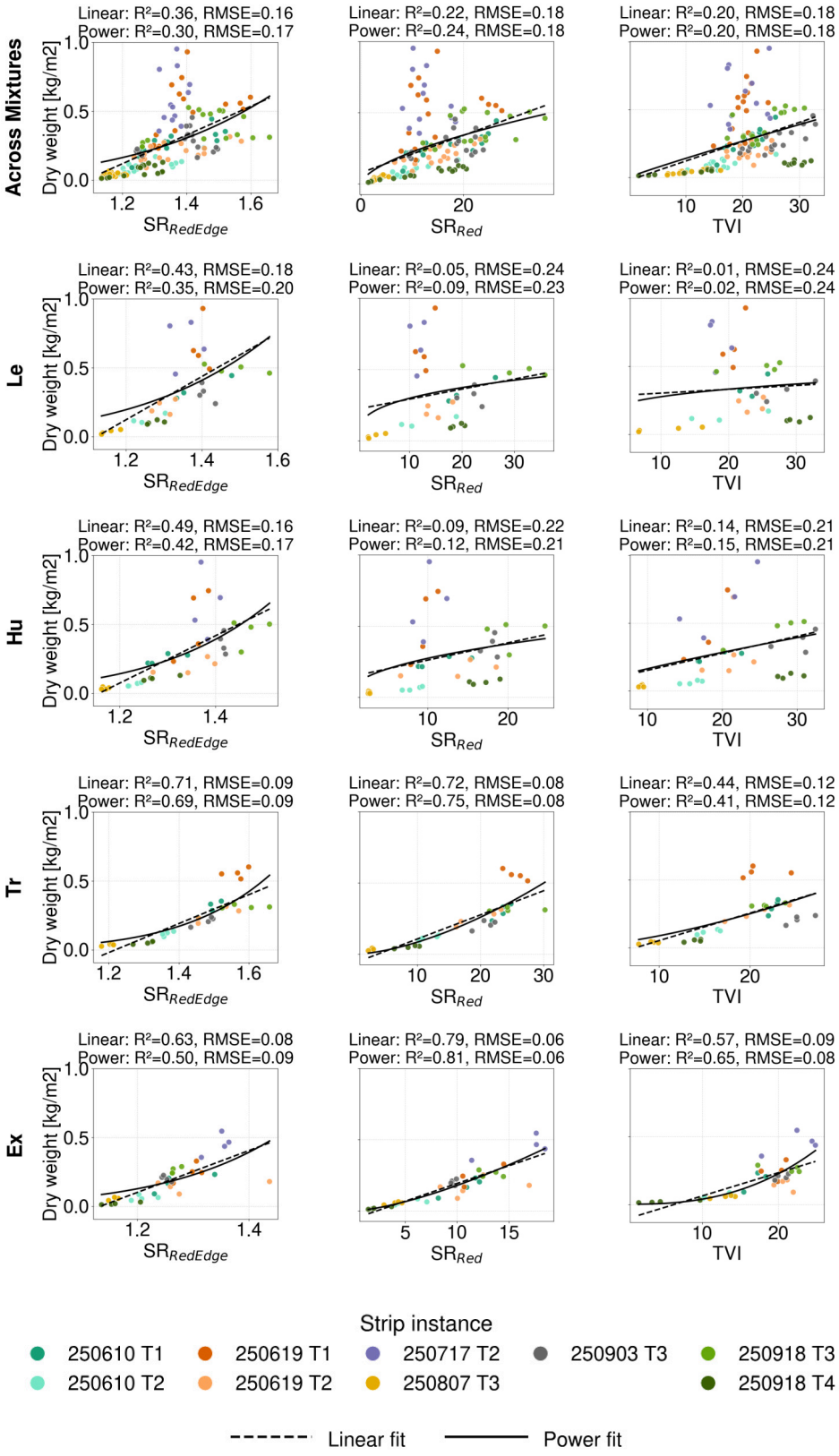

Figure C.3: Scatterplots between dry weight biomass and retrieved trait from radiative transfer model based and Vegetation Indices based approaches (part 3). **Left:** $SR_{RedEdge}$, **middle:** SR_{Red}, **right:** TVI. Displayed from top to bottom are across-mixture models and the four mixture-specific models (Le: Lepha, Hu: Humus, Tr: Trias, Ex: Express). Performance of the linear regression vs. power function is evaluated with R^2, RMSE and nRMSE.

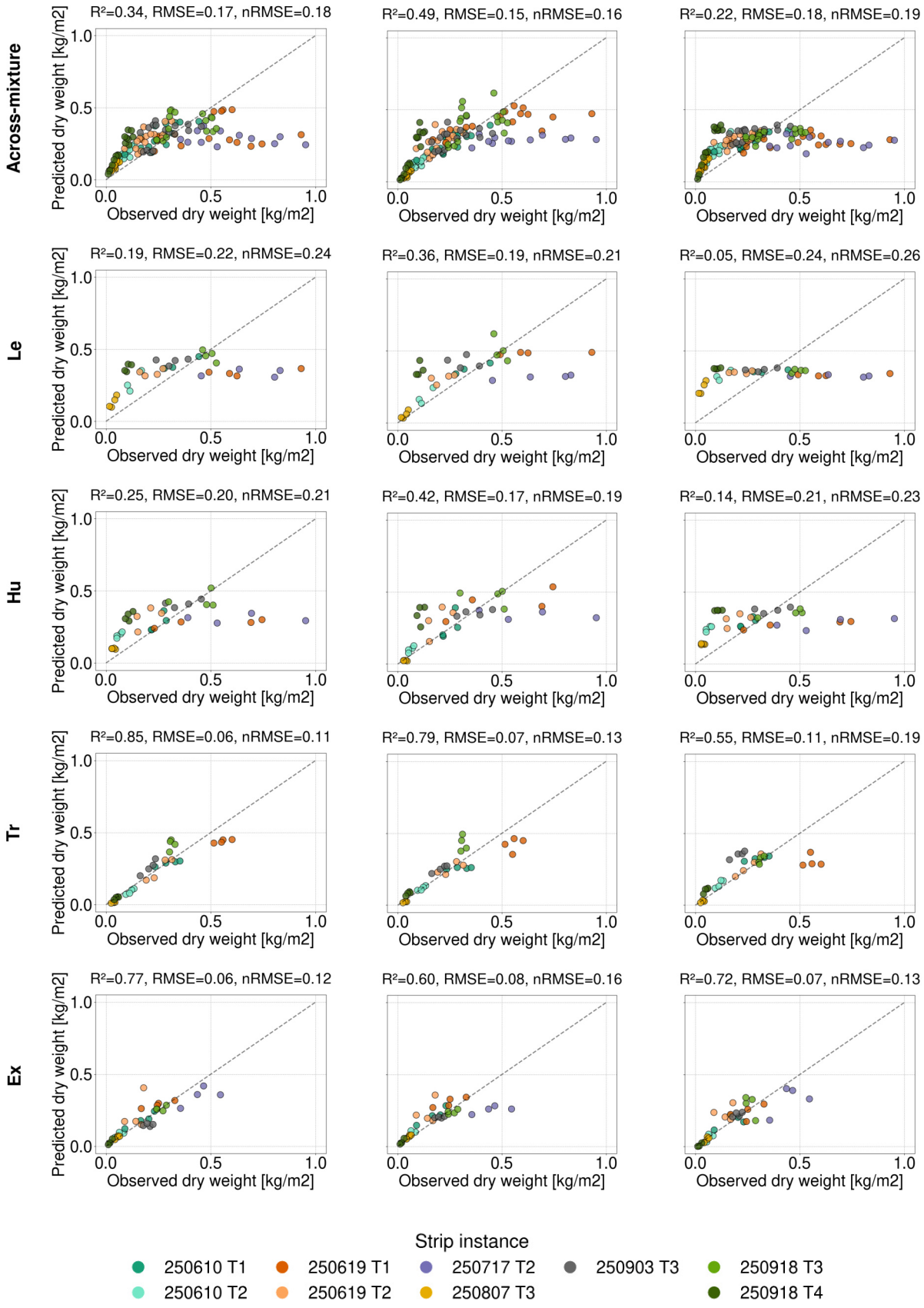

Figure C.4: Predicted versus observed scatter plots for dry weight biomass across-mixture and mixture-specific models (part 1). **Left:** Radiative transfer model, **middle:** GnyLi, **right:** Modified Triangular Vegetation Index 2. Displayed from top to bottom are across-mixture models and the four mixture-specific models (Le: Lepha, Hu: Humus, Tr: Trias, Ex: Express).

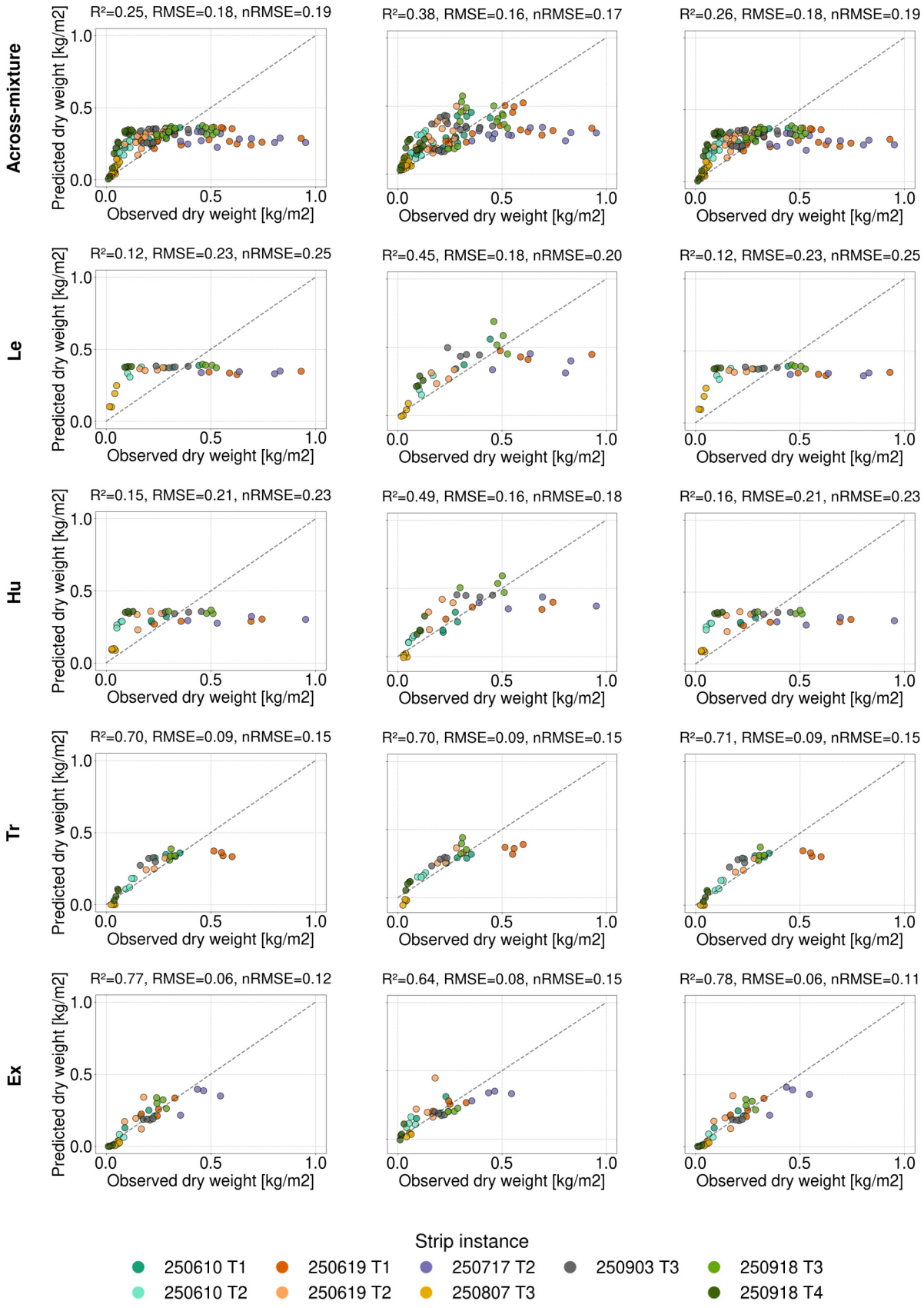

Figure C.5: Predicted vs. observed scatter plots for dry weight biomass across-mixture and mixture-specific models (part 2). **Left:** Normalized Difference Vegetation Index, **middle:** Normalized Difference red edge, **right:** Normalized Difference red. Displayed from top to bottom are across-mixture models and the four mixture-specific models (Le: Lepha, Hu: Humus, Tr: Trias, Ex: Express).

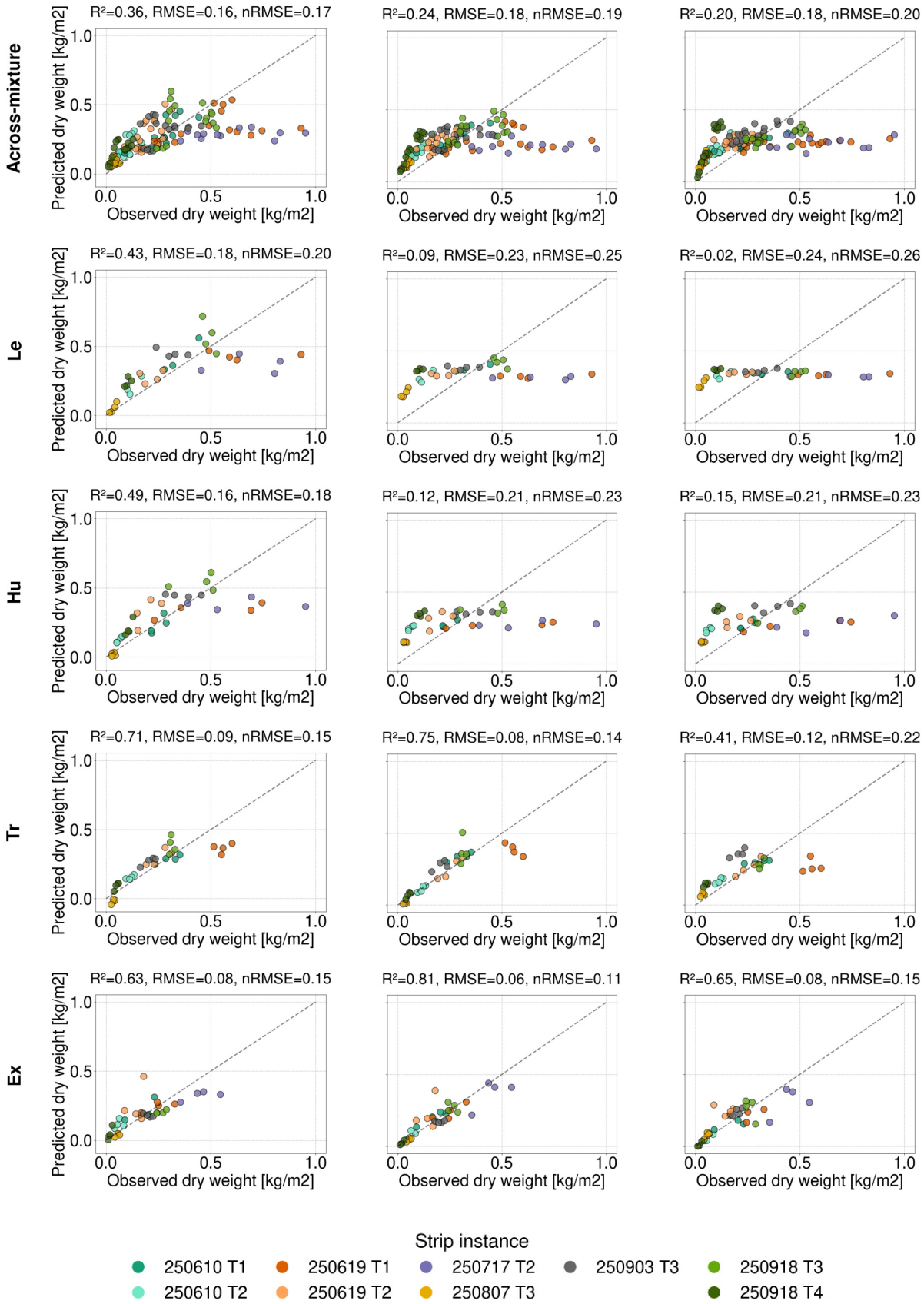

Figure C.6: Predicted vs. observed scatter plots for dry weight biomass across-mixture and mixture-specific models (part 3). **Left:** Simple Ratio red edge, **middle:** Simple ratio red, **right:** Triangular Vegetation Index. Displayed from top to bottom are across-mixture models and the four mixture-specific models (Le: Lepha, Hu: Humus, Tr: Trias, Ex: Express).

D Appendix: Results fractional cover under baseline modelling

Table D.1: Performance metrics of VI-based fractional cover models for mixture-specific and across-mixture models.

Approach	Metric	Across-mixture	Mixture-specific				
			Le	Hu	Tr	Ex	Mean
NDVI	R2	0.89	0.78	0.87	0.90	0.95	0.88
	RMSE	0.08	0.07	0.07	0.07	0.06	0.07
	nRMSE	0.08	0.11	0.09	0.08	0.06	0.09
	best fit	exp	exp	lin	exp	lin	-
GnyLi	R2	0.80	0.66	0.78	0.85	0.88	0.79
	RMSE	0.10	0.09	0.09	0.09	0.09	0.09
	nRMSE	0.11	0.14	0.12	0.10	0.10	0.11
	best fit	exp	exp	exp	exp	exp	-
SR_{Red}	R2	0.85	0.75	0.86	0.88	0.88	0.84
	RMSE	0.09	0.08	0.07	0.08	0.09	0.08
	nRMSE	0.09	0.12	0.09	0.09	0.10	0.10
	best fit	exp	exp	exp	exp	exp	-
$SR_{RedEdge}$	R2	0.44	0.31	0.53	0.59	0.65	0.52
	RMSE	0.17	0.13	0.14	0.15	0.16	0.15
	nRMSE	0.18	0.20	0.17	0.17	0.17	0.18
	best fit	lin	lin	lin	lin	lin	-
ND_{Red}	R2	0.88	0.77	0.87	0.90	0.95	0.87
	RMSE	0.08	0.08	0.07	0.07	0.06	0.07
	nRMSE	0.08	0.11	0.09	0.09	0.06	0.09
	best fit	exp	exp	lin	exp	lin	-
$ND_{RedEdge}$	R2	0.57	0.51	0.65	0.71	0.67	0.64
	RMSE	0.15	0.11	0.12	0.13	0.16	0.13
	nRMSE	0.15	0.17	0.15	0.15	0.17	0.16
	best fit	exp	exp	exp	exp	lin	-
TVI	R2	0.89	0.74	0.89	0.95	0.96	0.89
	RMSE	0.08	0.08	0.07	0.05	0.05	0.06
	nRMSE	0.08	0.12	0.08	0.06	0.06	0.08
	best fit	exp	exp	exp	exp	exp	-
MTVI2	R2	0.91	0.77	0.90	0.97	0.97	0.90
	RMSE	0.07	0.07	0.06	0.04	0.04	0.05
	nRMSE	0.07	0.11	0.08	0.05	0.05	0.07
	best fit	exp	exp	exp	exp	exp	-

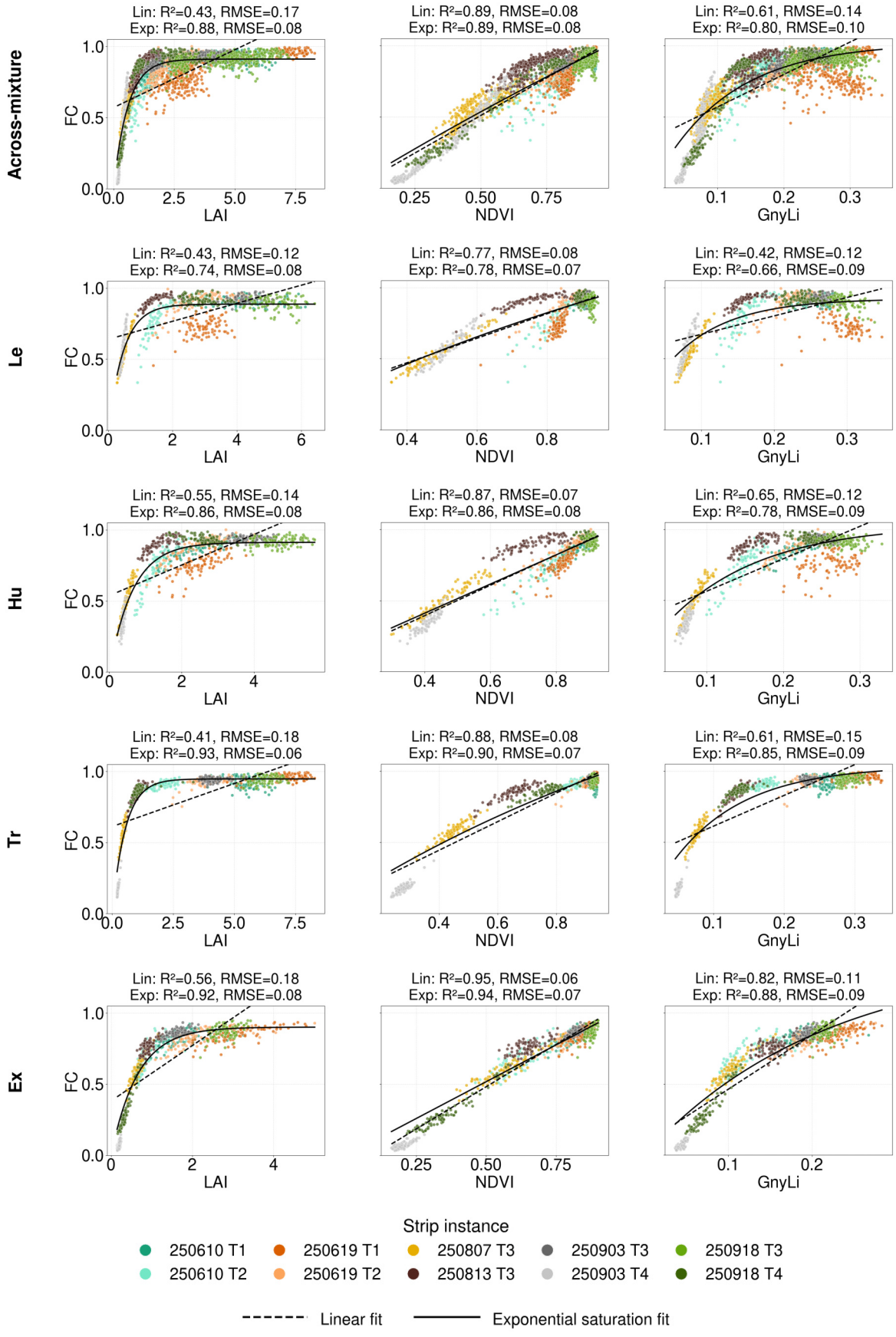

Figure D.1: Scatterplots of fractional cover versus retrieved trait from radiative transfer model based and vegetation indices based approaches (part 1). **Left:** Radiative transfer model derived Leaf Area Index (LAI), **middle:** Normalized Difference Vegetation Index (NDVI), **right:** GnyLi. Displayed from top to bottom are across-mixture models and the four mixture-specific models (Le: Lepha, Hu: Humus, Tr: Trias, Ex: Express). Performance of the linear regression vs. exponential saturation is evaluated with R^2, RMSE and nRMSE.

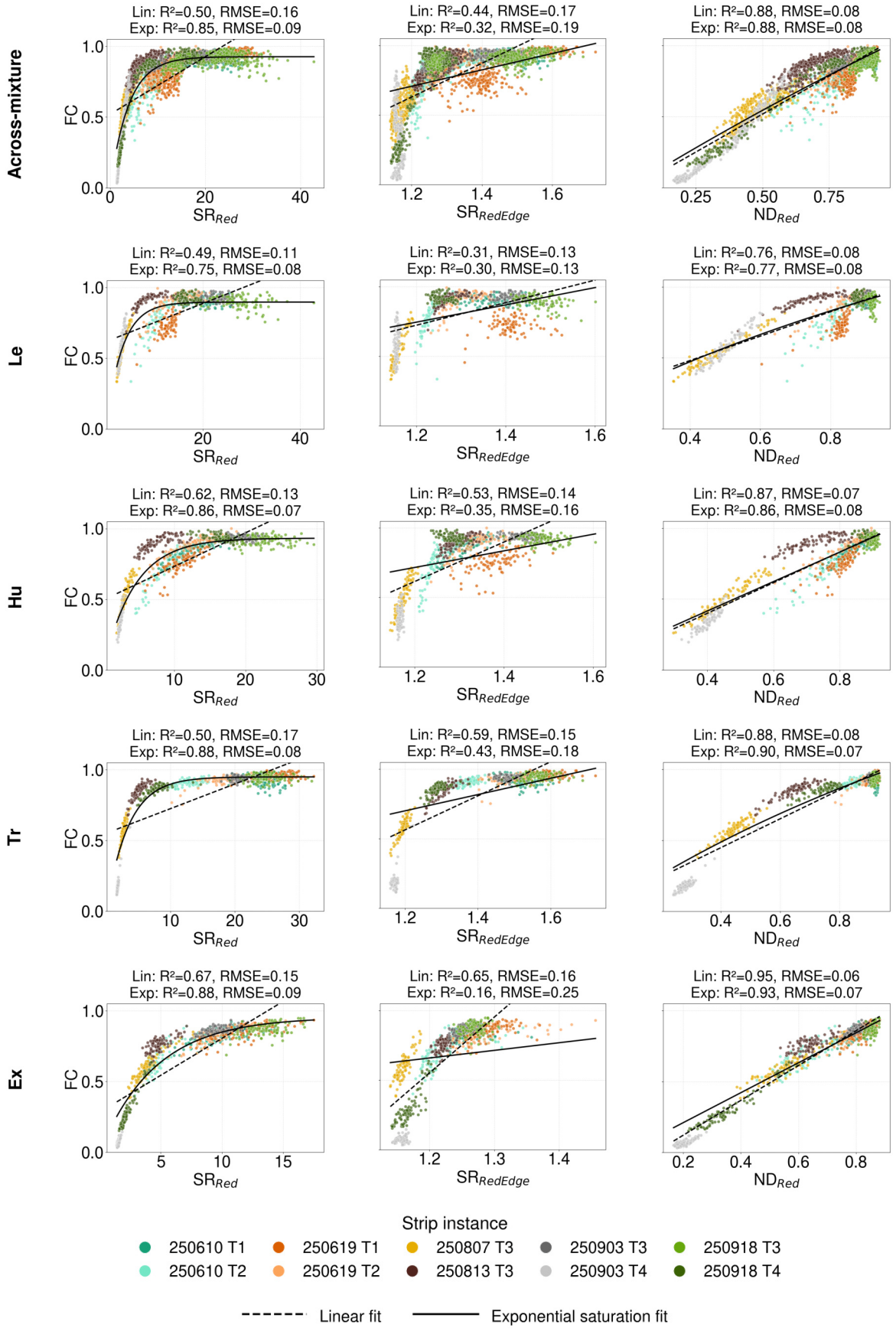

Figure D.2: Scatterplots of fractional cover versus retrieved trait from radiative transfer model based and vegetation indices based approaches (part 2). **Left:** Simple Ratio red (SR_{Red}), **middle:** Simple Ratio red edge ($SR_{RedEdge}$), **right:** Normalized Difference red (ND_{Red}). Displayed from top to bottom are across-mixture models and the four mixture-specific models (Le: Lepha, Hu: Humus, Tr: Trias, Ex: Express). Performance of the linear regression vs. exponential saturation is evaluated with R^2, RMSE and nRMSE.

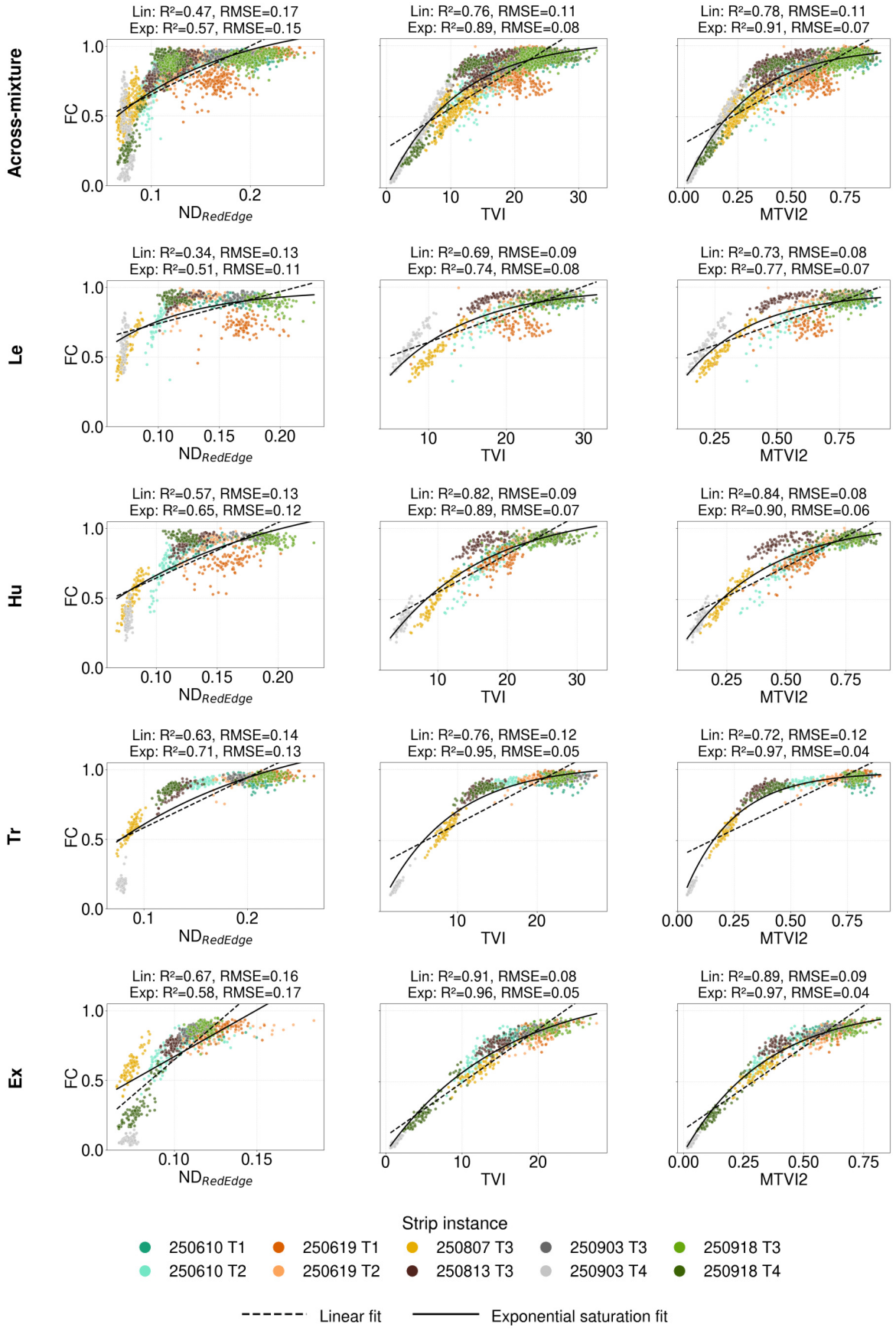

Figure D.3: Scatterplots of fractional cover versus retrieved trait from radiative transfer model based and vegetation indices based approaches (part 3). **Left:** Normalized Difference red edge ($ND_{RedEdge}$), **middle:** Triangular Vegetation Index (TVI), **right:** Modified Triangular Vegetation Index 2 (MTVI2). Displayed from top to bottom are across-mixture models and the four mixture-specific models (Le: Lepha, Hu: Humus, Tr: Trias, Ex: Express). Performance of the linear regression vs. exponential saturation is evaluated with R^2, RMSE and nRMSE.

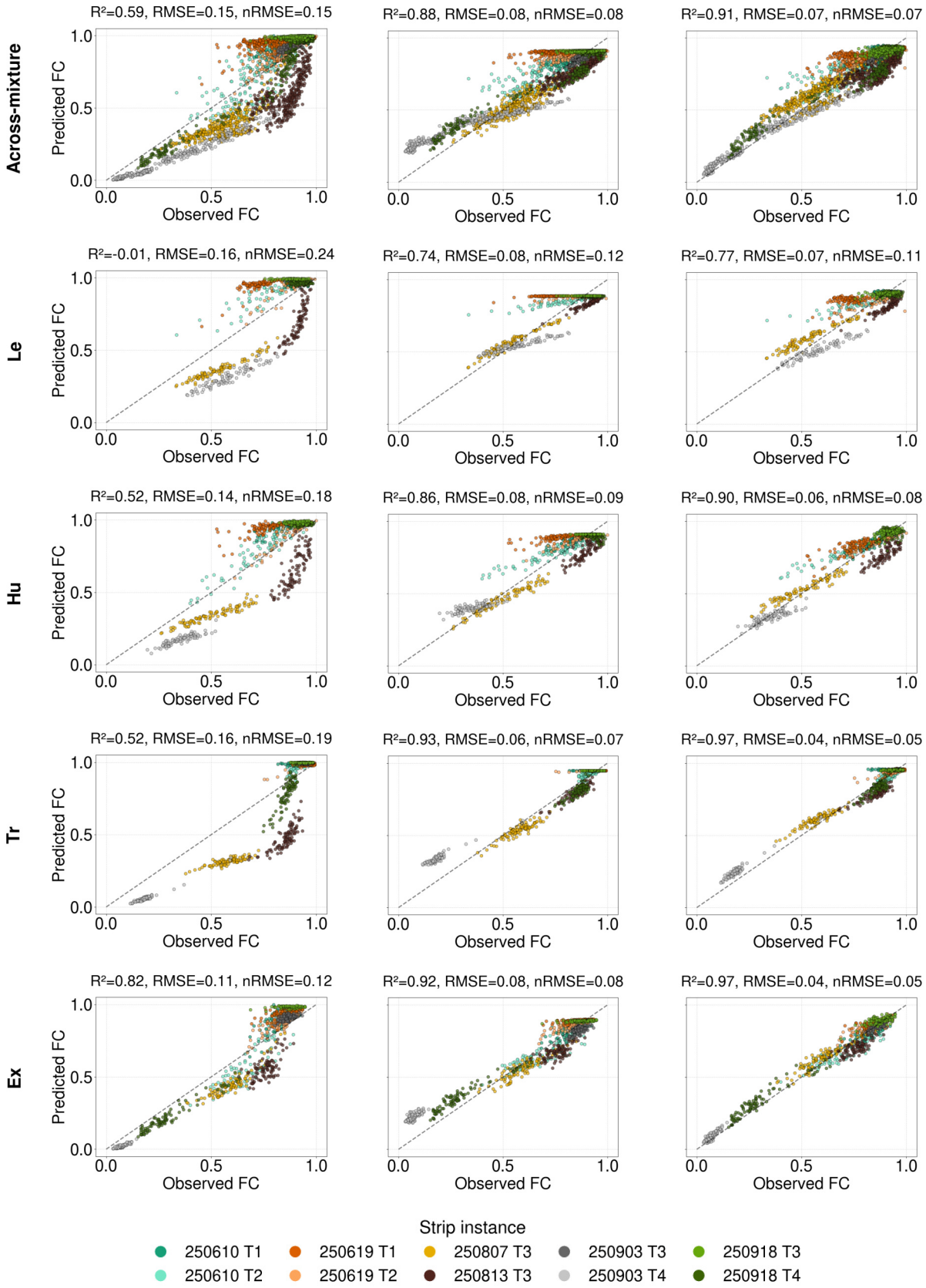

Figure D.4: Predicted versus observed scatterplots of across-mixture and mixture-specific models for fractional cover retrieval methods (part 1). **Left:** Spectral mixture analysis, **middle:** Radiative transfer model, **right:** Modified Triangular Vegetation Index 2. Displayed from top to bottom are across-mixture models and the four mixture-specific models (Le: Lepha, Hu: Humus, Tr: Trias, Ex: Express).

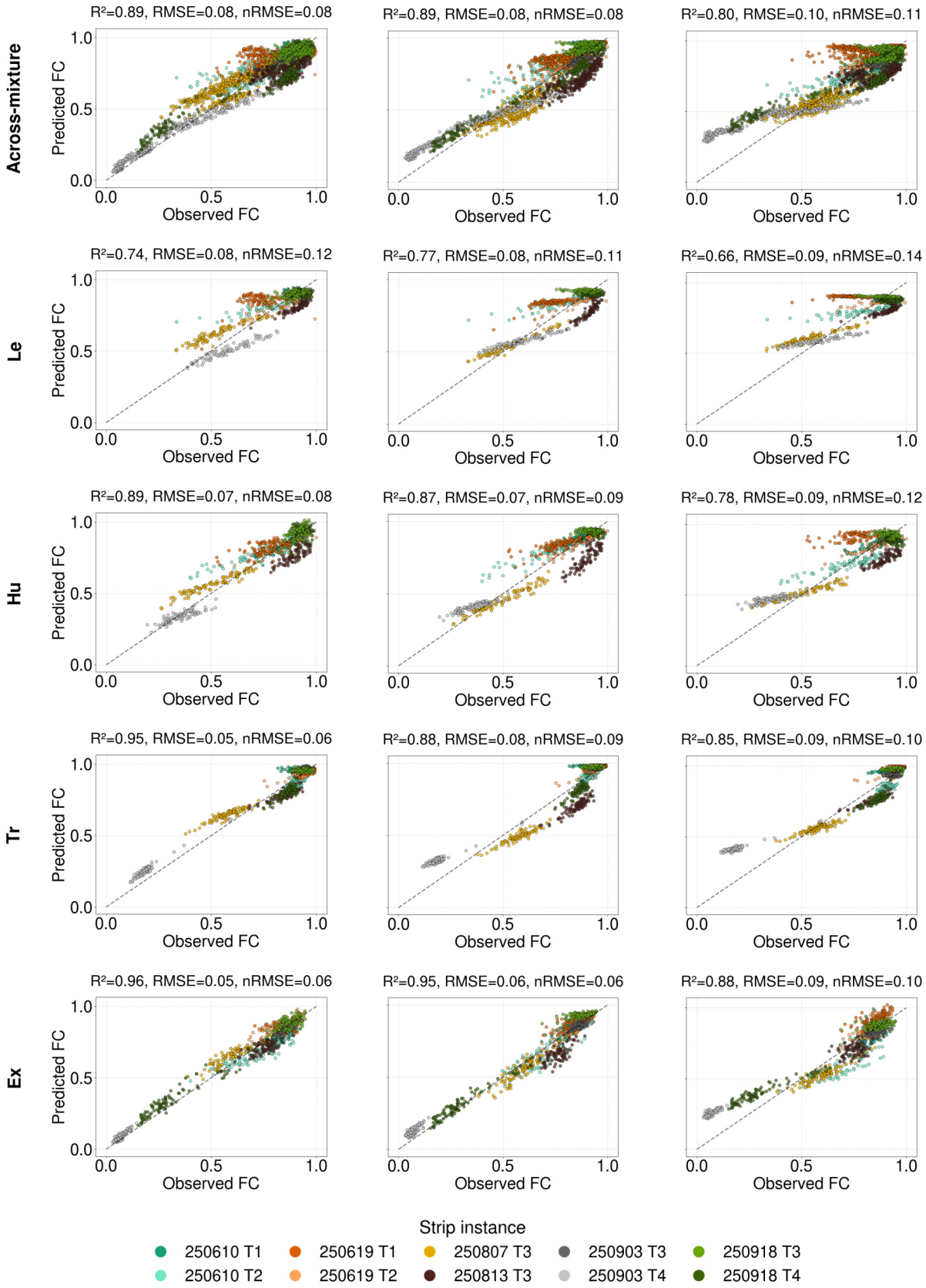

Figure D.5: Predicted vs. observed scatterplots of across-mixture and mixture-specific models for fractional cover retrieval methods (part 2). **Left:** Triangular Vegetation Index, **middle:** Normalied Difference Vegetation Index, **right:** GnyLi. Displayed from top to bottom are across-mixture models and the four mixture-specific models (Le: Lepha, Hu: Humus, Tr: Trias, Ex: Express).

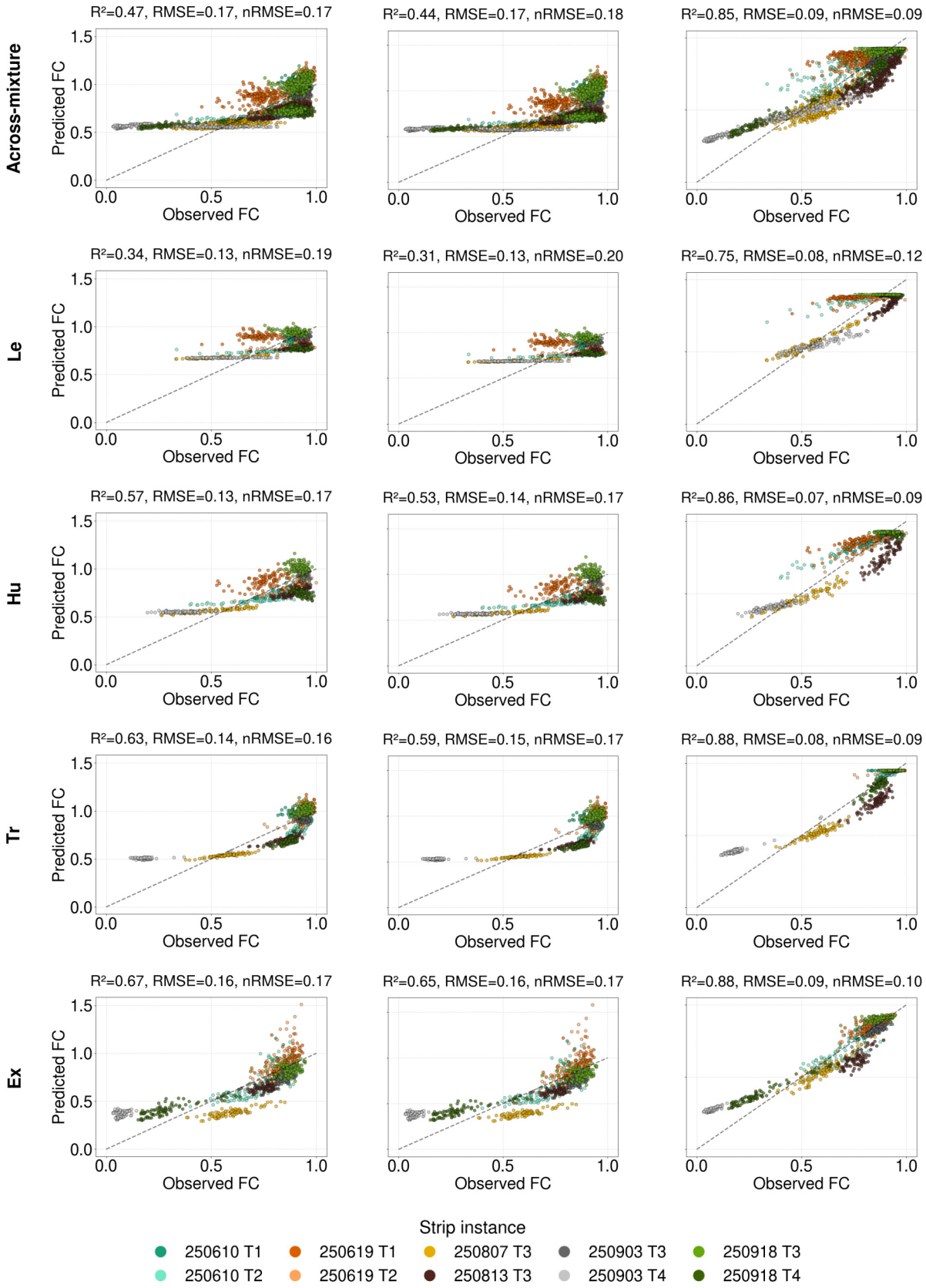

Figure D.6: Predicted versus observed scatterplots of across-mixture and mixture-specific models for fractional cover retrieval methods (part 3). **Left:** Normalized Difference red edge, **middle:** Simple Ratio red edge, **right:** Simple Ratio red. Displayed from top to bottom are across-mixture models and the four mixture-specific models (Le: Lepha, Hu: Humus, Tr: Trias, Ex: Express).

E Appendix: Results fractional cover under LOSIO-CV

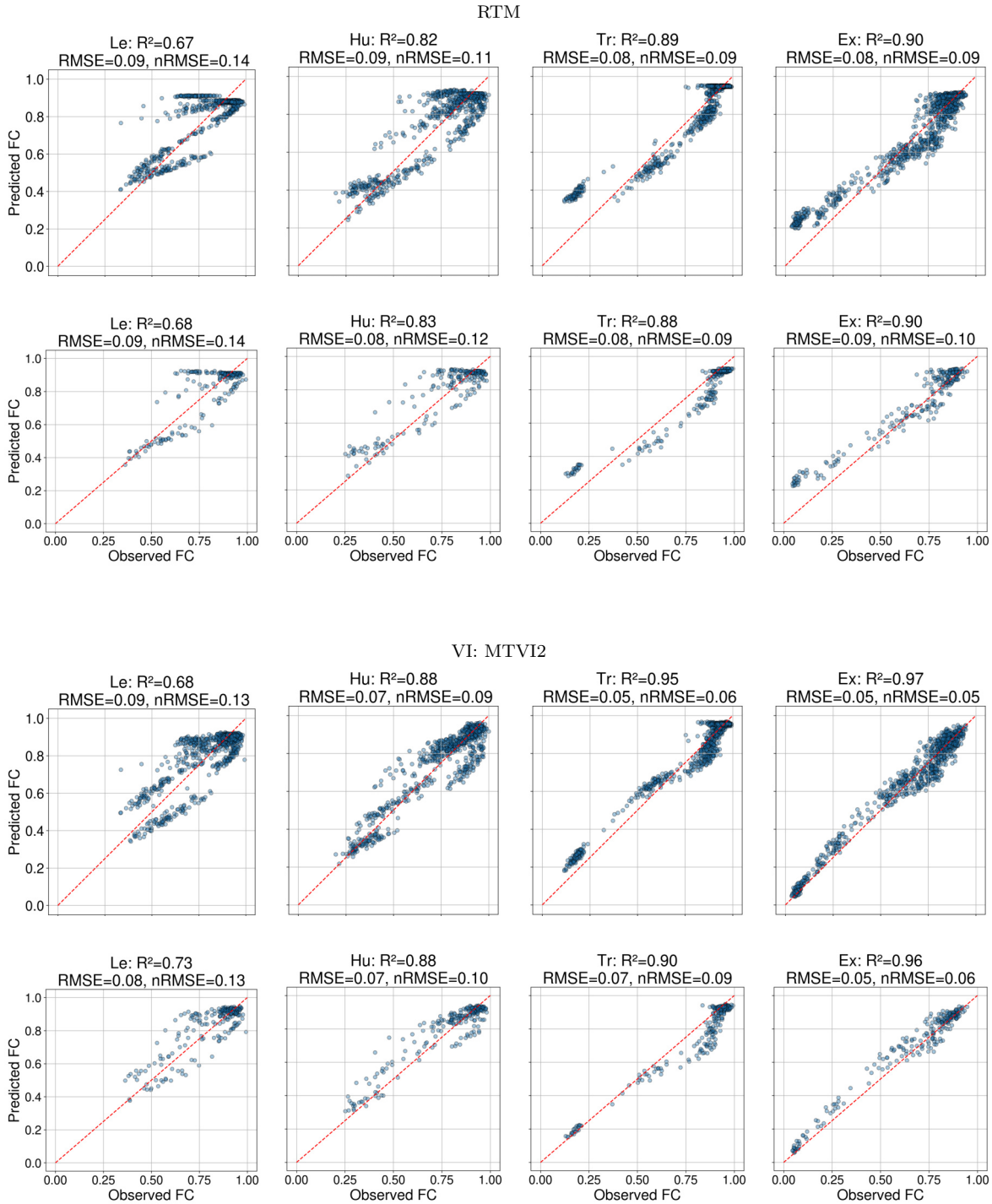

Figure E.1: Predicted versus observed fractional cover for RTM (radiative transfer model)-based (top two rows) and MTVI2-based models (bottom two rows), shown as global predictions across all test folds. For both methods, top rows show mixture-specific models for each mixture: Lepha (Le), Humus (Hu), Trias (Tr), and Express (Ex). Bottom rows show across-mixture models. Each point represents a test sample from one of the cross-validation folds.

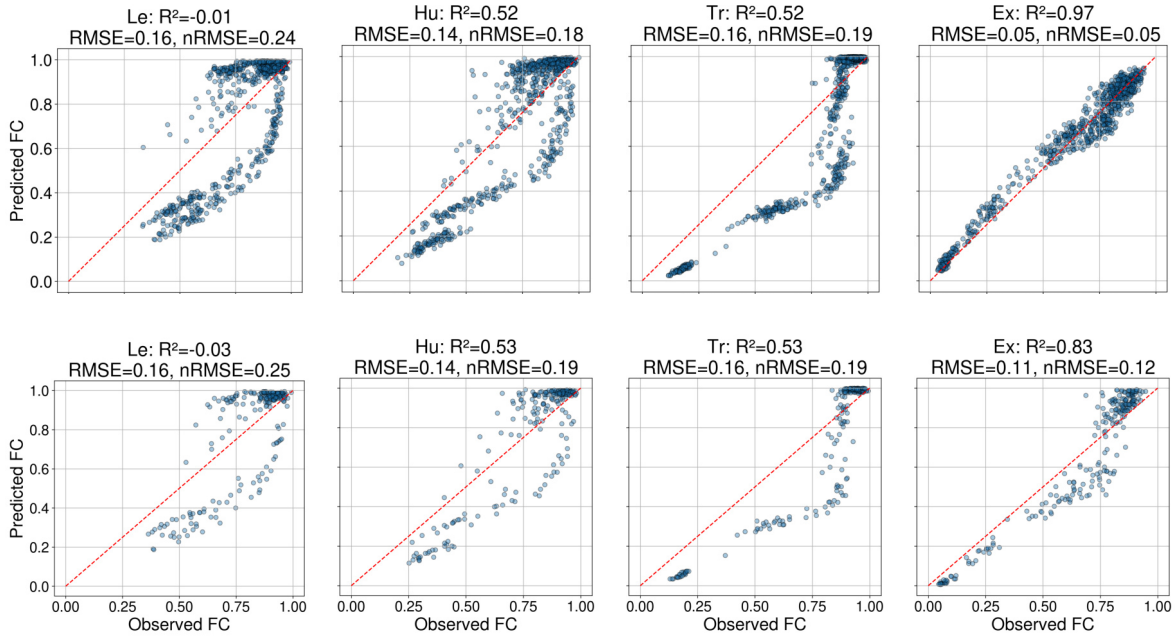

Figure E.2: Predicted versus observed fractional cover for the spectral mixture analysis (SMA)-based models, shown as global predictions across all test folds. Top row: Mixture-specific models for each mixture: Lepha (Le), Humus (Hu), Trias (Tr), and Express (Ex). Bottom row: Across-mixture models. Each point represents a test sample from one of the cross-validation folds.

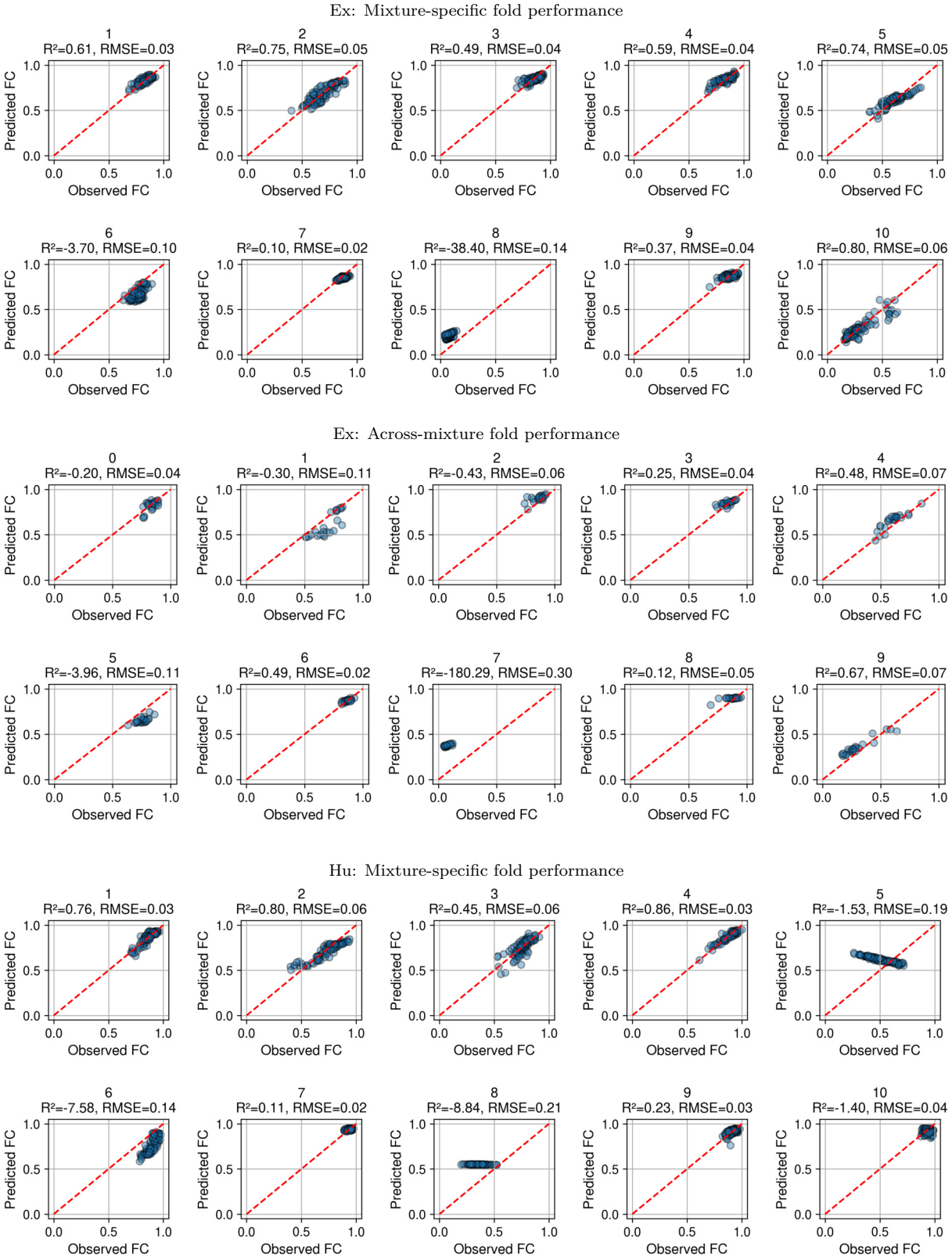

Figure E.3: Part 1: Performance of the neural network models for mixture-specific and across-mixture models per fold of the LOSIO-CV (leave-one-strip-instance-out cross-validation).

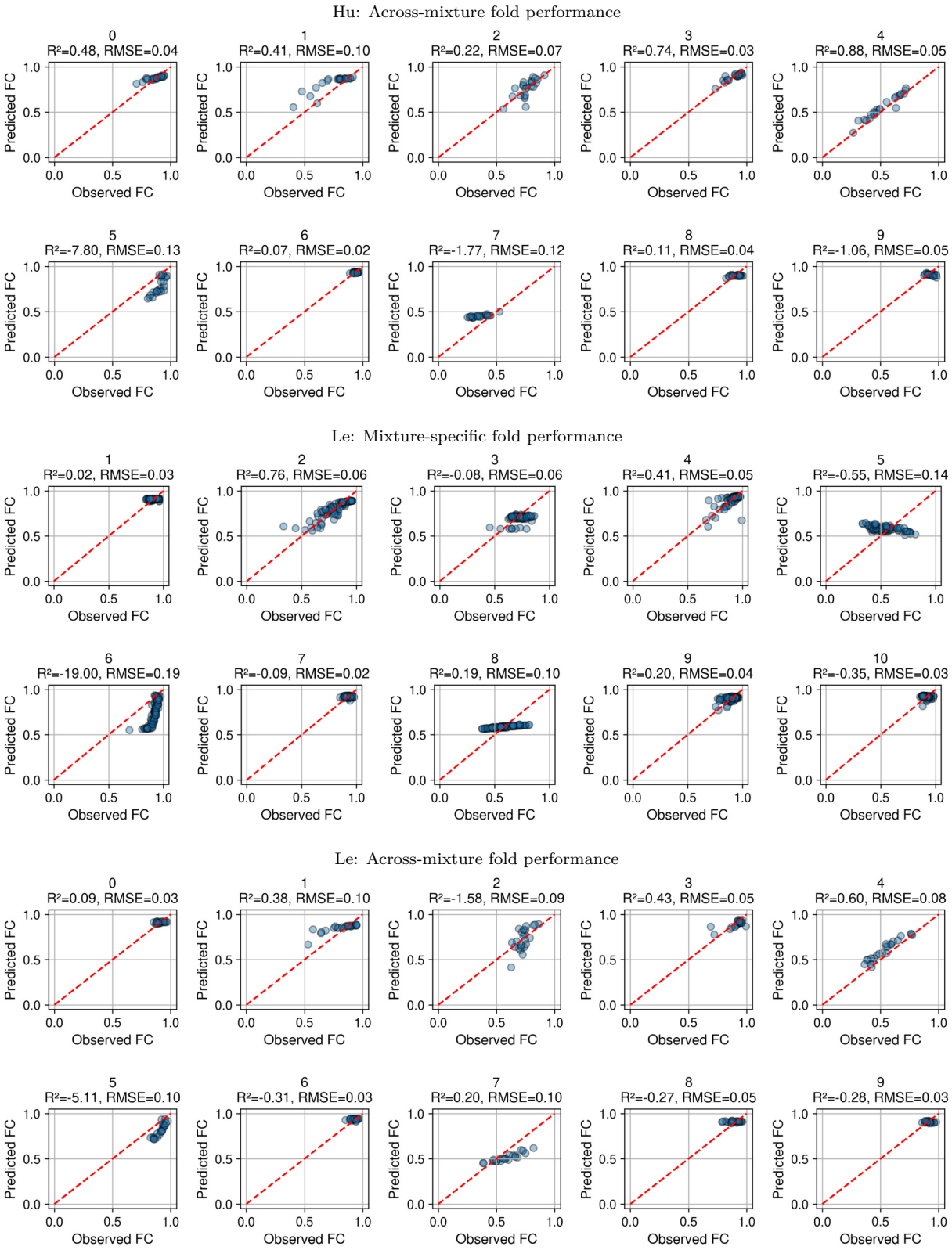

Figure E.4: Part 2: Performance of the neural network models for mixture-specific and across-mixture models per fold of the LOSIO-CV (leave-one-strip-instance-out cross-validation).

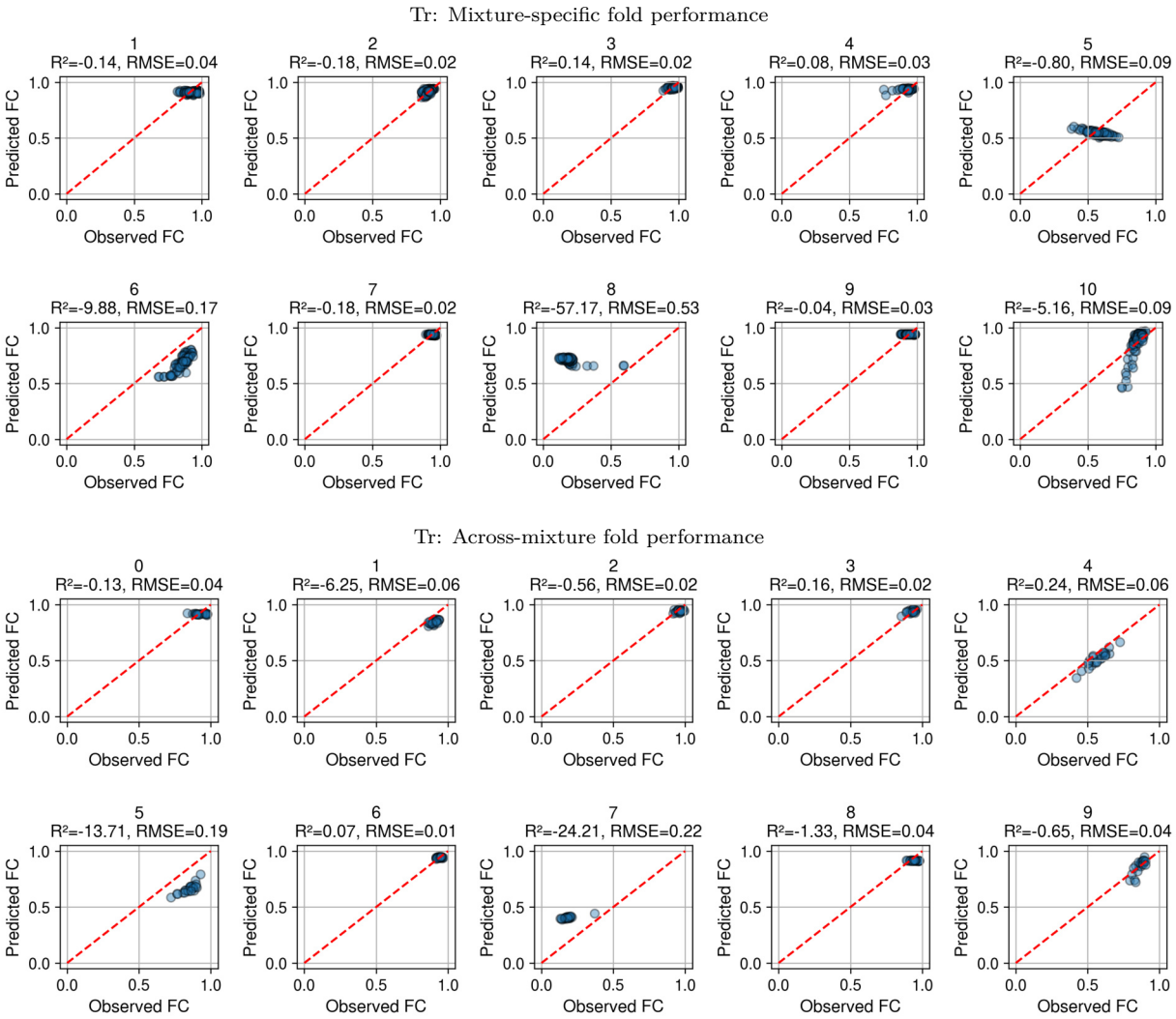

Figure E.5: Part 3: Performance of the neural network models for mixture-specific and across-mixture models per fold of the LOSIO-CV (leave-one-strip-instance-out cross-validation).

Declaration on the use of AI

I have used AI for this work, namely: ChatGPT-5 and DeepL.

I have used AI for the following purposes:

- Coding assistance: I used ChatGPT-5 to help write, debug, and optimize code for my analyses.
- Text improvement: I used DeepL and ChatGPT-5 to improve the clarity, grammar, and style of my written text.

With my signature I confirm that the above information is true.

Zürich, 30 January 2026 Valerie Schneider

Personal Declaration

I hereby declare that the submitted thesis is the result of my own, independent work. All external sources are explicitly acknowledged in the thesis.

Zürich, 30 January 2026 Valerie Schneider